Electric and Magnetic Properties of La2Cu04 and SrTi03 Nanoparticles Synthesized by Sol-Gel Method

著者	Budiman Faisal
その他のタイトル	ゾルゲル法によって作製したLa2Cu04およびSrTi03の電気的および磁気的特性
学位授与年度	平成30年度
学位授与番号	17104甲生工第330号
URL	http://hdl.handle.net/10228/00007055

Electric and Magnetic Properties of La_2CuO_4 and $SrTiO_3$ Nanoparticles Synthesized by Sol-Gel Method

by

FAISAL BUDIMAN

Dissertation submitted in partial fulfilment

of the requirement for the degree of

Doctor of Philosophy

SUPERVISOR:

PROF. HIROFUMI TANAKA

Graduate School of Life Science and Systems Engineering

Kyushu Institute of Technology

2018

ACKNOWLEDGEMENT

Thanks to Almighty God for the completion of my Ph.D study.

First of all, I would like to express gratitude to my supervisor, Prof. Hirofumi Tanaka for his supervision, guidance, support, help and assistance throughout my study. Thanks also to my project advisors: Assoc. Prof. Dr. Yoichi Horibe (Kyushu Institute of Technology), Dr. Isao Watanabe (RIKEN) and Prof. Kouichi Takase (Nihon University) for their advice, supervision and help.

Special acknowledgement is extended to Ministry of Education, Culture, Sport, Science and Technology (MEXT) of Japan for funding my Ph.D study through Global Assistive Adaptive Robotic (GAAR) Program. I would like to thank to all the lecturers and staff of Kyushu Institute of Technology for their kind assistance. Not forget, to those helped me at/during some experiments: Dr. Masanori Eguchi (Fuzzy Logic System Institute), Prof. Takuji Ogawa (Osaka University) Assoc. Prof. Ken-Ichi Yamashita (Osaka University), Dr. Satoshi Yamashita (Osaka University), Prof. Shuzi Hayase (Kyushu Institute of Technology), Dr. Gaurav Kapil (Kyushu Institute of Technology), Prof. Masaki Mito (Kyushu Institute of Technology), Mr. Ogata, Mr. Zhang Putao and Mr. Shibayama (Kyushu Institute of Technology), Ms. Suci Winarsih (Universitas Indonesia–RIKEN). Also, Thanks to all Tanaka Lab's members and Indonesia Student Association of Kitakyushu for accompanying and colouring my life in Japan in these three years.

To my families: Mubedi MS, Elly Yulia, Fitri Aprianti, Intan Fauziyyah, Furqon Hakim, Lilis Rusmini, Kustoyo, Hilmi Nur Fauzi and Maksoem's big family, I can never fully repay their careness, love and endless support. I am deeply indebted to them and truly wish that I have made them proud.

Faisal Budiman

July, 2018

TABLE OF CONTENTS

LIST OF FIGURES

FIGURE FROM CHAPTER 1

FIGURE FROM CHAPTER 2

FIGURE FROM CHAPTER 3

FIGURE FROM CHAPTER 4

FIGURE FROM CHAPTER 5

FIGURE FROM CHAPTER 6

FIGURE FROM CHAPTER 7

LIST OF TABLE

TABLE FROM CHAPTER 1

TABLE FROM CHAPTER 2

TABLE FROM CHAPTER 3

TABLE FROM CHAPTER 8

LIST OF ABBREVIATIONS

AF	Antiferromagnetic
CB	Conduction band
T_c	Critical temperature
DEP	Dielectrophoresis
EBL	Electron beam lithography
FESEM	Field emission scanning electron microscopy
LCO	Lanthanum copper oxide
LSCO	Lanthanum strontium copper oxide
μSR	Muon spin rotation
NPs	Nanoparticles
NWs	Nanowires
T_N	Néel temperature
SQUID	Superconducting quantum interference device
STO	Strontium titanate
TEM	Transmission electron microscopy
UV-Vis	UV-Visible
VB	Valence band
XRD	X-ray diffraction

LIST OF SYMBOLS

Å	Angstrom
μB	Bohr magneton
σ	Conductivity
I	Current
°	Degree
℃	Degree Celcius
emu	Electromagnetic unit
eV	Electron volt
g	Gram
h	Hour
K	Kelvin
<	Less than
H	Magnetic field
M	Magnetization
MHz	Megahertz
nm	Nanometer
Oe	Oersted
%	Percentage
s	Second
χ	Magnetic susceptibility
V	Voltage
λ	Wavelength

ABSTRACT

Investigation of magnetism and electrical properties of nano-sized particles has been a subject of interest in past years owing that their properties are deviated compared to their bulk. Perovskite oxide is one of the best materials to study such effect, since lattice distortion and non-stoichiometric form is allowed in the structure, depending on various stimuli, thus the material is potentially to appear with extraordinary variety of properties. For example, modulating electrical properties from insulating to metallic is possible. Therefore, investigation of a perovskite oxide in nanoscale order is become important.

La_2CuO_4 (LCO) and $SrTiO_3$ (STO) nanoparticles (NPs) were selected in this research work. LCO is basically a frontier of strong correlated materials of an antiferromagnetic (AF) Mott insulator. The strong electron-electron interactions makes the material to exhibit superconductivity, by introducing charge carriers to the system. As an AF and metal oxide, the LCO also potentially to have various applications such as spin-valve device and gas sensors, respectively. Moreover, STO also holds important electronic properties owing to its wide band gap, and, since it is an excellent substrate for epitaxial growth, physics of oxide heterostructure based on STO material is also of interest to be studied. To date, there are no details report on the magnetic and electric properties on free-standing STO and LCO. By controlling the properties of such nano-sized system, the results obtained will become fundamental for further research work and very potential to be developed for future electronic and magnetic device applications.

In the present work, free-standing LCO and STO NPs were synthesized by sol-gel method and its magnetic and/or electric properties were reported. Various method have been applied to synthesize a perovskite, such solid-state, co-precipitation, sol-gel, hydrothermal and spray technique. Sol-gel was selected considering the products are finer, higher in purity, more controllable and easy to conduct. Morphological observation by field emission scanning electron microscopy (FESEM) showed that the NPs has spherical structure and their size could be controlled depending on the annealing condition during synthesis, the

size product is proportional with annealing temperature/time of synthesis. X-ray diffractometry (XRD) results indicating the minimum annealing condition to obtain LCO and STO phase at least at 600 ℃ for 45 min and 500 ℃ for 5 h, respectively. Additionally, the obtained smallest NPs have 69 nm and 21 nm size, for LCO and STO, respectively.

Size dependent magnetic properties of LCO based compound was investigated by superconducting quantum interference device (SQUID) magnetometer, as a function of temperature and magnetic field. Magnetization enhancement was observed with reducing size. Additionally, the magnetism of LCO also was assessed in microscopic view by muon spin rotation (μSR) and the results showed drastically reduction of Néel temperature (T_N) with decreasing size. The LCO NPs with 69 nm size has T_N at about 60 K, compared to their bulk $T_N \approx 300$ K. Size effect also studied in the doped sample, the LCO is doped by Sr to exhibit superconductivity. Cancellation of superconductivity was observed in small particle size.

Electric properties of the fabricated LCO and STO NPs were also investigated. Firstly, electrodes separated with nanoscale gap were fabricated by electron beam lithography (EBL). The synthesized STO and LCO NPs were aligned at the electrodes by dielectrophoresis (DEP) technique. DEP is a technique to manipulate the movement of particles by applying non-uniform electric field, therefore the NPs bridging electrodes and electrical characteristics can be measured at various temperature. The results showed that the conductance of the samples increases with raising temperature, for both LCO and STO NPs samples. Two conduction mechanisms originating from hopping and tunneling appeared in the Arrhenius plot.

Keywords: *La_2CuO_4, $SrTiO_3$, nanoparticles, sol-gel, magnetic and electric property*

CHAPTER 1
Introduction and Literature Review

1.1. General introduction

This chapter provides the background, motivation and based knowledge gathered from literature as guidance on assessing and evaluating the work results. In here, the theory of magnetism and electric properties is presented, as well as the general properties of La_2CuO_4 (LCO) and $SrTiO_3$ (STO). The advantages of using nanoscale material and the synthesis process will be reviewed as well focusing on nanoparticles. As sol-gel is the main method used in this work for nanoparticles formation, the theory of sol-gel process and several factors affecting in the technique will be reviewed in here as well.

1.2. Nanomaterials

Studies on nanoscale materials driven interest of researchers over the past decades owing their unique properties compared with their bulk. Nanomaterials are defined as a material with any external dimension in the nanoscale (size range from approximately 1 nm to 100 nm.[1)] If the material has internal nanostructure or surface nanostructure, it called nanostructured material.[1)] Nanomaterials can be classified as zero-dimensional (0-D), one-dimensional (1-D), two-dimensional (2-D) and three-dimensional (3-D).[2)] The classification is based on the number of dimensions, which are confined to the nanoscale range (< 100 nm), as illustrated in Figure 1.1. The 0-D materials refer to the form of nanoparticles (NPs), which defined as a material which has nanoscale in three dimensions (x, y, z). The 1-D nanomaterials are a material which has two dimensions (x, y) at nanoscale, but other dimension (L) is not. The structure can be in the forms of nanowire, nanofibre, nanorod, nanobelt or nanotube.[3)] If only one dimension (t) at nanoscale and the others two dimensions (Lx, Ly) are not, it referred to 2-D nanomaterials. Similarly, 3-D nanomaterials refers to no bulk dimensions at nanoscale. The size range that holds so much interest is typically from 100 nm down to the atomic level, because it is in this range (particularly at the lower end)

that materials is expected to have different or enhanced properties compared with the same materials at a larger size. The two main reasons for this change in behavior are an increased relative surface area. As there are more surface atoms compared to the corresponding bulk, there are more interaction is built between the nanomaterials with the surrounding material, making the material more reactive and sensitive. As the size of matter is reduced to tens of nanometers or less, quantum effects can begin to play a role,[2] and these can significantly change a material's properties.

The synthesis of nanomaterials can be classified as top-down and bottom-up process.[2] Top-down process refers to the formation of nanomaterials by slicing the bulk material to nano-sized material, regularly done by attrition and/or milling process.[4] Top-down process serves straight forward and better size control, but the process may damage to the crystallographic and leave imperfection on the surface structure. Differs from top-down process, bottom-up relates to assembling the nanomaterial from atom/molecules,[5] generally referred as chemical synthesis. Some bottom-up process including sol-gel technique hydrothermal, anodic and thermal oxidation, chemical vapor deposition, pyrolysis, etc. In this work, perovskite oxides in the form of NPs are fabricated through sol-gel technique and its electrical and magnetic properties are investigated.

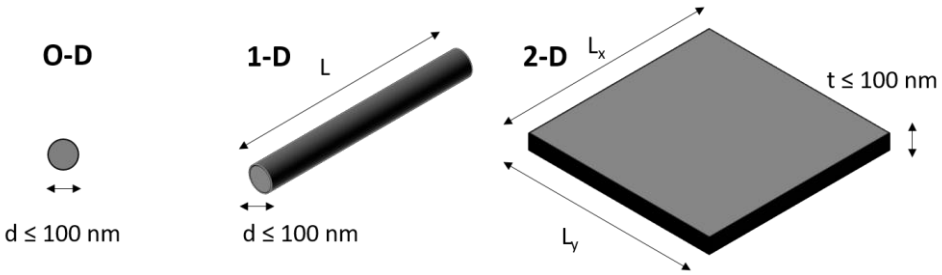

Figure 1. 1 Illustration of 0-D, 1-D and 2-D nanomaterials

1.3. Basic of magnetism

Magnetism is the property of a material to be attracted or repelled by magnetic field. Every material exhibits some kind of magnetic behavior, but

different material respond to applied magnetic fields in different ways, either as magnetic or non-magnetic material. The magnetic behavior of a material under influence of an applied magnetic field can be classified as: (1) ferromagnetic, (2) superparamagnetic, (3) paramagnetic, (4) antiferromagnetic (AF) and (4) diamagnetic.[6] Figure 1.2 shows the graph response of every magnetic behavior of a material under applied magnetic field, called magnetization curve *M-H*. Paramagnetic describes a phenomena where the magnetization in a material is attracted and follows the applied field proportionally, but are not able to retain the magnetic properties as the magnetic field is removed. The nature of paramagnetic are due to the presence of some unpaired electrons, even though some of defects in a material also the cause of paramagnetic, such as adsorbed oxygen species (O^-, O_2^-, O_3^-), hole or electron trapping centers.[7] Additionally, the magnetization curve of AF material also exhibit linear dependence of magnetization with the applied field, similar with paramagnetic material. However, usually AF material can be characterized by Néel temperature (T_N): transition temperature where the AF change to paramagnetic behavior, usually observed in the temperature dependent magnetization at fixed applied field.

Diamagnetism describes when the applied magnetic field causes a material become weakly magnetized in a direction opposite to the applied magnetic field. Some example of diamagnetic materials such as bismuth, water, mercury, quartz, alcohol, air, etc. Moreover, there is also kind of material that totally expel the applied magnetic field (perfect diamagnetism), namely superconductor, where it expulses magnetic field thus possesses magnetic levitation due to Meissner effect. Superconducting property usually occurs at low temperature (characterized by critical temperature (T_c)) and researchers now is still struggling to make the critical temperature of a superconductor material at ambient condition. Characteristic of diamagnetic, AF and paramagnetic are: 1) the curve is linear, 2) the intersect line is zero and 3) the magnetization is irreversible.

Ferromagnetic material (such as nickel, iron, cobalt) exhibits a strong attraction to the applied magnetic field and the material are able to retain their magnetic field, meaning if a ferromagnetic material is magnetized in one

direction, it will not back to the original when the magnetic field is removed. It must be forced back to zero by the opposite direction of magnetized and the key feature of ferromagnetic property is hysteresis loop. There are also a material with behavior superparamagnetic, which commonly appears in small ferromagnetic NPs, where a graph will be saturated at some point. Typical superparamagnetic material occurs in NPs sample. The reduction of size causes the magnetic anisotropy energy (energy that maintains particular orientation of magnetic moment) per NP decreases, therefore triggering the random flipping of the magnetic moment and influencing the maximum magnetization possible and may saturated become superparamagnetic.[6)]

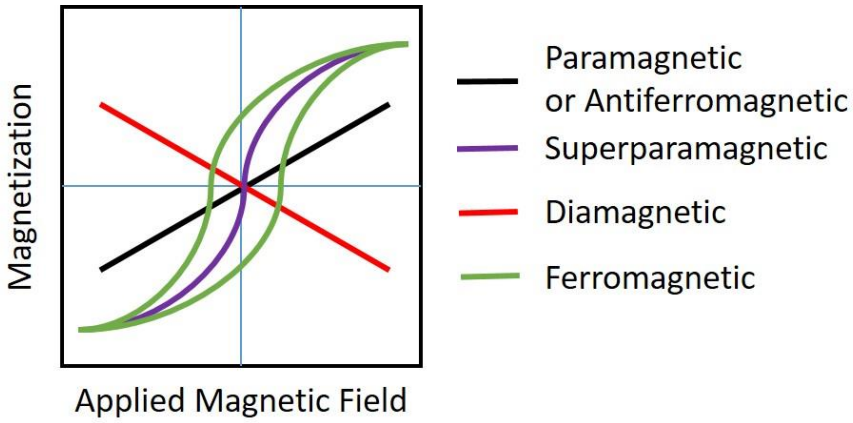

Figure 1. 2 Magnetic behavior under the influence of an applied magnetic field

1.4. Magnetic nanoparticles

Magnetic characteristics of NPs has driven interest of researchers owing these nanoscale magnets has unique physical properties, associated with surface and size effect.[6)] Size effects are attributed to the nano-metric size of the particles, while surface effects are related to the symmetry breaking of the crystal structure at the boundary of each particle.[8)] By experiencing size effect, the magnetic behavior of a material can be classified to superparamagnetic, single domain, pseudo-single domain or multi domain structure.[9)] As an example, in a ferromagnetic material, the coercivity is zero in superparamagnetic region and the maximum coercivity is attained in single domain region. Further decreases

with increasing size/change to multi domain region. Additionally, by reducing size, the magnetic transition temperature also reduced. As now the dimension of a material is reduced, the large number of surface area is developed and significantly affected the exchange interaction among surface atoms and affecting the magnetic transition temperature.

Moreover, size reduction acquired the material to become more defective, particularly at surface and introducing some uncompensated spins.[10] As these uncompensated spins are coupled to the magnetic spins of the core, it modified the physical properties of a material. In very small sample, the surface property may dominating the measured magnetic properties and could concealed the information about the core magnetic order.[11] Park et al. investigated the effect of particle size on $BiFeO_3$ material and found enhancement of magnetization as size is reduced.[12] Bhowmik et al. also found similar improvement related to size effect on $CoRh_2O_4$.[13] They proposed a core-shell model on explaining the magnetic characteristic of AF NPs. The core property is essentially AF and shell with uncompensated spins. When size is reduced, more and more numbers of shell spins is introduced and break the AF configuration. Consequently, there is a modulation of AF and less-AF magnetic regions and significantly contributes on the magnetization of sample. Zheng et al. investigated the magnetic properties of AF material CuO NPs with 5 nm size using muon-spin rotation (μSR) and magnetic susceptibility measurement and reported the suppression of T_N to 30 K, while the bulk T_N is about ~ 229 K.[14] Size dependent T_N also reported by Rinaldi-Montes works in NiO material.[15]. Conversely, the properties of a material is also determined by size.

1.5. Basic of electric property

Related to the ability of a material to conduct electrical charge carriers, materials can be categorized into three different types: metal, semiconductor and insulator.[16] The difference is illustrated by schematic band diagram in Figure 1.3. In a metal, the valence band (VB) overlaps with conduction band (BC), thus electrons are free to move and easily promoting currents. In a semiconductor

material, the VB and CB are separated in the limited amount of band gap energy (E_g). The E_g is narrow enough and the electrons must be promoted to be excited from VB to CB by inducing photon or thermal energy in equal amount (or more) with the E_g. Insulator have identical band gap structure like semiconductor, but with a very large band gap and required large amount of energy to promote electrons to reach the CB, making the material non-conductive.

Differentiating metal and semiconductor can also be determined by their resistance response against temperature. Characteristic of metal is, the resistance increases with temperature. As explained above, since the VB and CB of a metal is overlap, therefore, increasing temperature promotes more collision of electrons and generating heat, thus leads to the increase of resistance. Unlike metal, resistance of semiconductor decreases with increasing temperature. With increasing temperature, thermal energy promotes more electrons to be excited from VB and CB, in consequence more currents are generated.

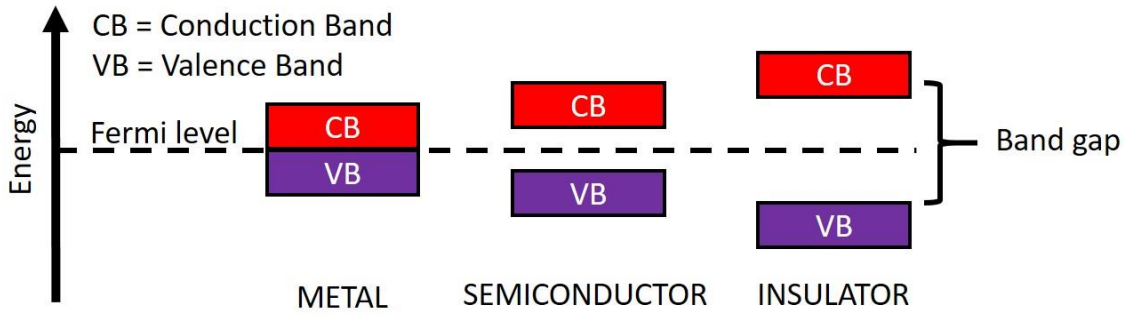

Figure 1. 3 Schematic band diagram of metal, semiconductor and insulator

There are also material called Mott insulator, with strong electron interactions. The comparison of band insulator and Mott insulator is illustrated in Figure 1.4. According to the band theory, if the highest band is full-filled, it becomes an insulator and if it is half-filled, it is a metal. The band theory is fitted for material with low electron-electron interactions. A Mott insulator should be metallic because of the half-filled band instead insulating because of strong electron-electron repulsion, namely strong correlated material. Example of strong correlated material such as NiO, La_2CuO_4, Fe_3O_4 and VO_2. Mott insulator could

be changed to metallic property by various stimuli and driven interest in advanced physic research, although is not yet fully understood. One applications is such strong correlated system is superconductivity.

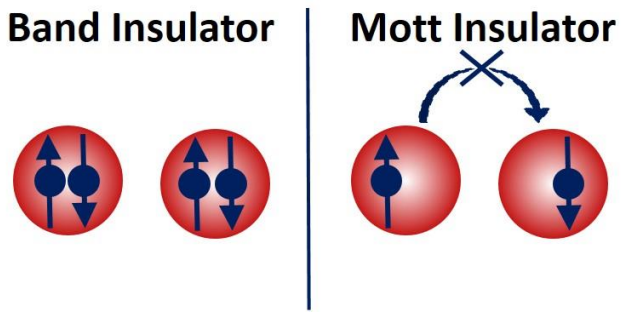

Figure 1. 4 Illustration of band insulator and mott insulator

Measurement of electric properties regularly done in a device equipped with metal electrodes. When a semiconductor are brought in contact with metal, a potential barrier is created at the interface due to difference in work function, thus transfer electrons from the metal to semiconductor is restrained or hindered.[17] To allow the electrons cross the barriers (form a junction), the Fermi level must be in line at equilibrium. Metal with high work function is usually used if the semiconductor is p-type,[17] such as Platinum (Pt), Nickel (Ni), and Gold (Au).[18] Work function is defined as the required work from Fermi level to the vacuum level. In a p-type semiconductor, the hole is majority carrier and the Fermi level closes to VB, therefore metal with high work function is preferable to be used. In the same way for n-type semiconductor, metal with low work function is generally used, for example Aluminum (Al), Titanium (Ti), Chromium (Cr). Moreover, heat treatment is also possible to improve electrical contact between metal and semiconductor.[18] By heating, enhancement of bonding between metal to the semiconductor is induced, and, it is also well known most contacts in semiconductor devices are subjected to heat treatment, prior to adhering process.[17] For example, electrical contact of Ti-Al contact was improved after the device was subjected to annealing at 1273 K.[19]

1.5.1. Dielectrophoresis

Dielectrophoresis (DEP) is a movement of a dielectric particles forced by non-uniform electric field.[20] The technique is capable on separating, assembling, or sorting variant types of particles. DEP offers low cost and rapid process, since the system only requires electrodes, electric field gradient generator and suspending medium. As the electric field gradient induces to the particles in surrounding medium, the particle experiences DEP force, either be repelled (negative DEP) or attracted (positive DEP) to the higher electric field. The magnitude and direction of the particle movement depend on the relative polarization of the particles and the surrounding medium. For spherical particle, the DEP force is expressed by Equation 1.1:

$$\vec{F} = 2\pi r^3 \varepsilon_m \, \mathrm{Re}\left(\frac{\varepsilon_p - \varepsilon_m}{\varepsilon_p + 2\varepsilon_m} \right) \nabla \vec{E}^2 \quad \text{..... (1.1)}$$

Where $\vec{F}$ is dielectric force of DEP, r is the particle radius, ε_m is the dielectric constant of the solvent medium, $\mathrm{Re}\left(\frac{\varepsilon_p^* - \varepsilon_m^*}{\varepsilon_p^* + 2\varepsilon_m^*} \right)$ is the real part of the Clausius-Mossotti factor, ε_m^* is the complex dielectric constant of the solvent medium, ε_p^* is the complex dielectric constant of the particle and $\vec{E}$ is the gradient of external electric field.

DEP is mainly utilized in biological sciences, such to separate cancer cells from healthy cells[21] or trapping microorganism.[22] Yang et al. controlled the trapping of bacteria cell by controlling the frequency and medium used.[23] As illustrated in Figure 1.5, the increase of frequency caused the bacterial to be repelled [Figure 1.5 (a)], both repelled and attracted [Figure 1.5 (b)] and attracted [Figure 1.5 (c)] to the electrode. Equally important, it is also possible to control the negative and positive DEP by adjusting the medium used, where the condition of $\varepsilon_{cell} > \varepsilon_m$ will result on positive DEP and condition of $\varepsilon_{cell} < \varepsilon_m$ will exhibit negative DEP.[23] However, the frequency and medium used are different for every dielectric particles, depending on the nature properties of the particle itself.

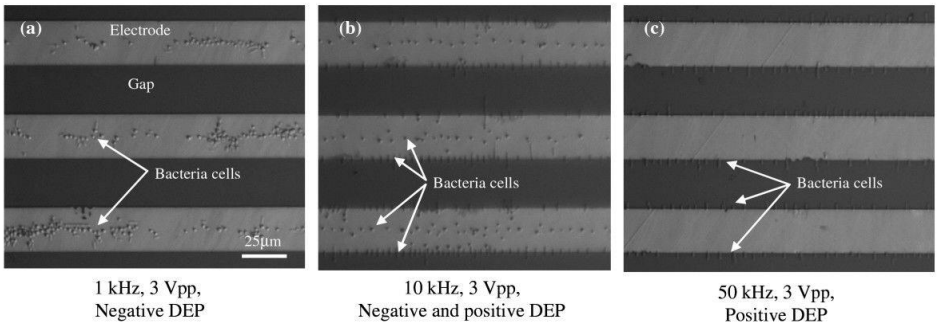

Figure 1. 5 Negative and Positive DEP.[21] (Open access article (free permission to reuse from BioMed Central Ltd.)

Recently, DEP technique is also utilized to assembly nanostructure and measuring their electrical properties. Wang et al. aligned ZnO NWs by DEP technique and studied the effect magnitude and frequency of the applied electric field, as displayed in Figure 1.6.[24] They reported that the rise of frequency caused NWs to tighter, straighter and more uniformly aligned at electrodes, as seen in Figure 1.6 (a) and (b), where magnitude of applied is responsible for the density of assembled NWs [see Figure 1.6 (c) and (d)].[24]

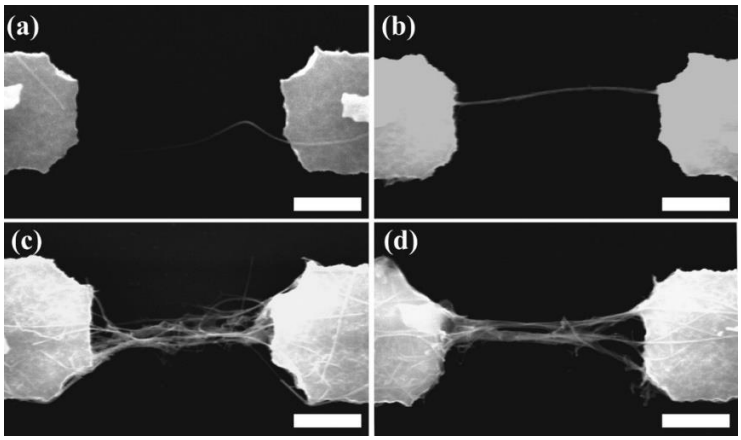

Figure 1. 6 Trapping of ZnO NWS. The magnitudes and frequencies were: (a) 1 V_{pp} at 0.1 MHz, (b) 1 V_{pp} at 10 MHz, (c) 20 V_{pp} at 0.1 MHz, and (d) 20 V_{pp} at 10 MHz. The scale bars correspond to 1 μm.[24] (Reprinted with permission from AIP Publishing)

1.6. Perovskite

Perovskite is a compound with structural formula ABO_3 or A_2BO_4 (with A and B are metals) and the crystal structure is illustrated in Figure 1.7. In the ideal form, the structure is cubic or nearly cubic (ABO_3), but also possible to have close to tetragonal structure (AB_2O_4). This compound has high structural stability and the A or B cation can be substituted by an impurity (for example: A') with different oxidation state or radius, allowing the variation of oxidation state of B and the oxygen vacancy,[25] thus deviation of its stoichiometric form is allowed in perovskite material.

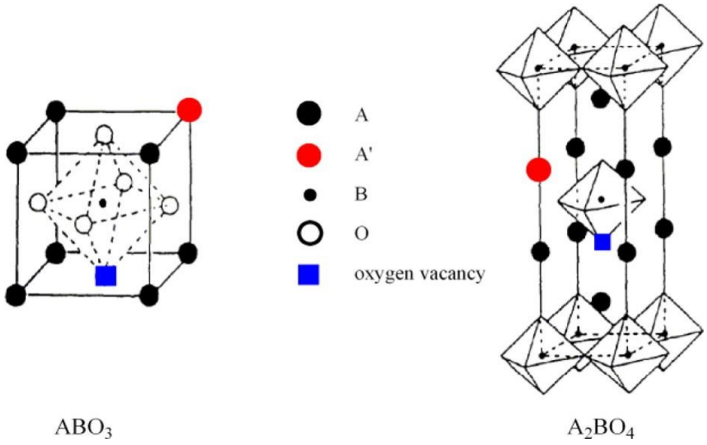

Figure 1. 7 Crystal structure of perovskite with ABO_3 (left) and AB_2O_4 (right) structure.[25] (Reprinted with permission from ACS Publications)

The main interesting characteristics of perovskite oxide material is the distortion of lattice, involving the rotation of the BO_6 octahedral in the structure. This distortion derives depending on the temperature, pressure, dopant, or concentration of oxygen in the structure. Some distortions results on the change of ideal cubic form to orthorhombic, rhombohedral, hexagonal or tetragonal forms and the compound hence acquire several phase transitions. As consequence, the compound may acquire several phase transitions and exhibiting great variability of properties. This flexibility structure might able to accommodate the properties most all of the elements in the periodic system. As an example, modulating the electrical properties from insulating, semiconducting and metallic behaviors is possible to be had in one material,

under various stimuli.[26] For that reason, this compound is considered as the best oxide material to be studied. Therefore, by fabricating a perovskite material in nanoscale order is one interesting topic to be investigated. These benefits might fulfil the demand of technology advancement in magnetic and electronic devices.

1.6.1. Lanthanum cuprate

Lanthanum cuprate (La_2CuO_4/LCO) is a perovskite oxide material contains trivalent La and divalent Cu. The compound exhibits insulating property instead of metallic due to electron-electron interactions, even though conventional band theories indicates LCO is metallic.[27,28] Therefore, the material is classified as a Mott insulator. Regularly, the crystal structure of LCO adopt K_2NiF_4 type-structure with oxygen sharing (CuO_6) in the structure consists of a stacking of single CuO_2 plane embedded with multilayers of LaO along c axis, as illustrated in Figure 1.7 (right part). The CuO_2 and LaO layers act as conducting and insulating layers respectively.[29] Hord et al. studied the variety of phase transitions in LCO material, and the XRD profiles (measured with λ = 70.930 pm) of all possibility LCO phase is shown in Figure 1.8.[30] There are three different crystal structure in LCO: 1) T', 2) tetragonal and 3) orthorhombic structure, and can be distinguished by observing the peak at ~ 15º. At room temperature, the LCO has orthorhombic structure [see Figure 1.8 (c)] and changed to tetragonal structure [Figure 1.8 (b)] upon heating at above 723 K. The transformation is reversible and the changed could be identified by splitting peak at ~ 15º. Moreover, there is also a metastable T' phase [Figure 1.8 (a)], where the synthesized processes done through different moderate synthesis temperature technique, with molten metal hydroxide as starting material.[30,31]. However, the T' phase transformation is irreversible, it transforms to tetragonal phase upon heating, but during cooling it changed to orthorhombic.

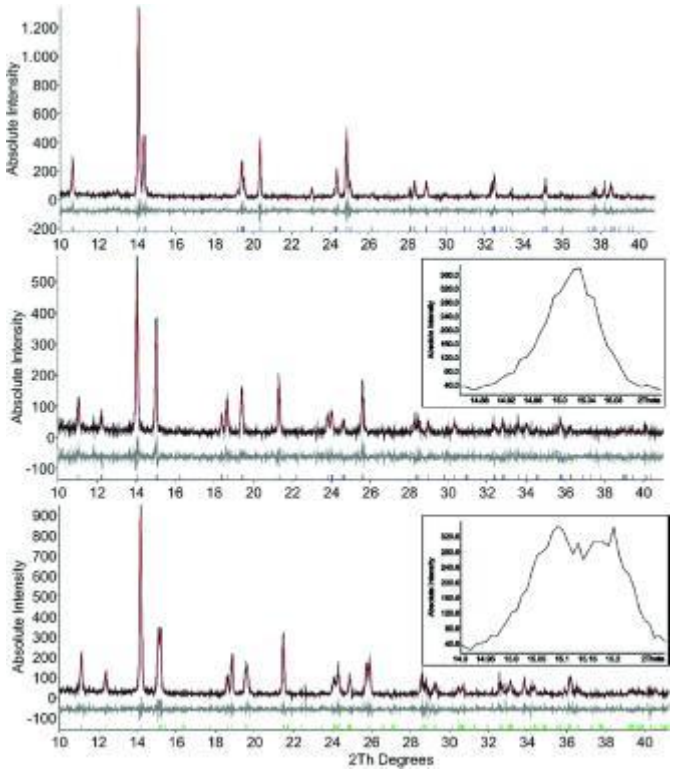

Figure 1. 8 Powder pattern of LCO with (a) T', (b) tetragonal and (c) orthorhombic structure from up to bottom.[30] (Reprinted with permission from Wiley publishing)

In stoichiometric form, LCO is an AF Mott insulator.[32] Budnick et al. investigated the magnetic properties of LCO by μSR technique and found the bulk LCO is AF with T_N is about 250 K,[33] followed by Saylor et al. work, reported the T_N of bulk LCO is about 317 K.[34] Recently, Storchak et al. also conducted similar experiment, with the obtained T_N at about 300 K.[35] However, the properties of LCO was reported very sensitive to the stoichiometry of the compound,[36,37] since it is easy to be introduced by oxygen and influenced by sample fabrication process.[38] Uchida et al. studied about the electric properties of bulk LCO and the resistivity increased at low temperature, proving the bulk LCO is semi conductive.[36] In contrast, a study of LCO electrical transport by Lin et al., the LCO synthesized by plasma sintering at temperature above 875 ℃ shows metallic property, where the other sample annealed lower than 875 ℃ shows weak temperature dependent electrical resistivity.[39]

Through incorporation of charge carriers, the properties of LCO drastically changed. The great interest studies of LCO based compound aroused since it is a starting system of high temperature superconductive material, as discovered first by Bédnorz and Muller in La-Ba-Cu-O system.[40] Since the evolution of high temperature cuprate superconductors, LCO based compound were deeply studied due to its simple structure.[32] Typically, superconducting property is generated from LCO system through incorporation of metal dopant (M = Ba^{2+}, Sr^{2+} or Ca^{2+}) to the structure [$La_{2-x}M_xCuO_4$ (LMCO)]. By replacing some La ions, charge carriers are introduced to the conduction layer and different property appears. Figure 1.9 shows the typical phase diagram concentration of LCO doped by metal and oxygen. Upon metal doping (i.e. Sr) [see Figure 1.9 (a)], there are three main regions in the phase diagram: (1) under doped, (2) optimum doped and (3) over doped region.[27] In under doped region ($x < 0.05$), the AF property of sample will be vanished at around $x \sim 0.02$, following by disordered magnetic moment (i.e. spin-glass state) at around $0.02 < x < 0.05$. The optimum doped to exhibit superconducting property will be at $0.06 < x < 0.30$, and the over doped region ($x > 0.03$) vanishes the superconductivity. The superconducting property is regularly characterized by critical temperature (T_c); the transition temperature for superconductivity occur. The maximum T_c in LCO compound when the doping level is set at $x = 0.015$ with $T_c = 40$ K. Typical magnetic susceptibility measurement in La-Ba-Cu-O system at superconducting region is as displayed in Figure 1.10, reported by Gugucia et al.[41] They studied the effect of hydrostatic pressure on the T_c in La-Ba-Cu-O system. As seen the value of y axis is negative, means expulsion of magnetic flux occur and applied pressure caused the increase of T_c.

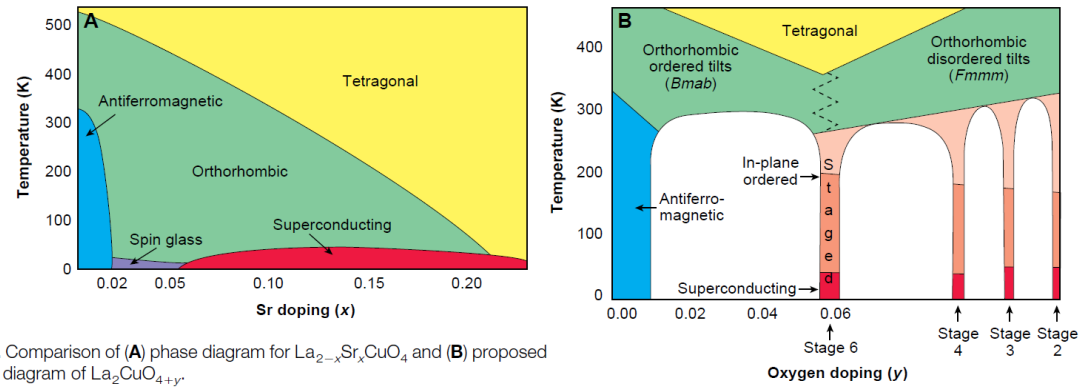

Fig. 1. Comparison of (**A**) phase diagram for $La_{2-x}Sr_xCuO_4$ and (**B**) proposed phase diagram of La_2CuO_{4+y}.

Figure 1. 9 Comparison of phase diagram for: (a) $La_{2-x}Sr_xCuO_4$ and proposed La_2CuO_{4+y}.[27] (Reprinted with permission from American Association for the Advancement of Science)

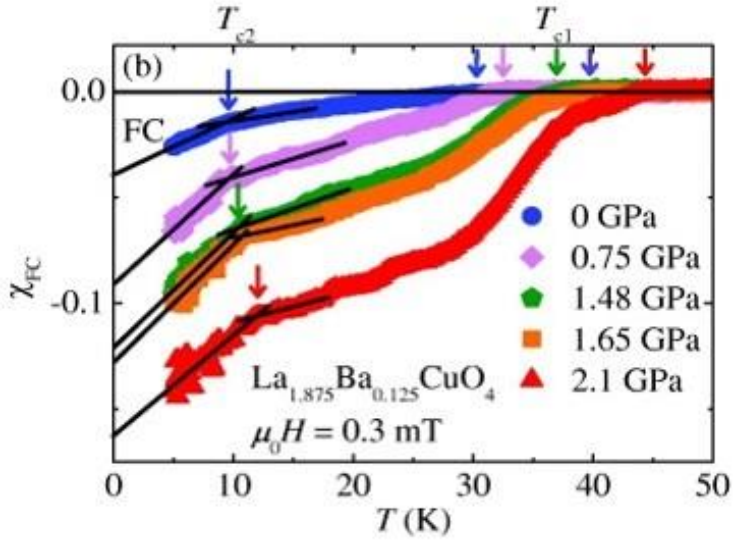

Figure 1. 10 Temperature dependent magnetic susceptibility with various applied hydrostatic pressure showing expulsion of magnetic field.[41] (Open access journal – free permission to reuse from IOPscience publishing)

Hole also can be induced to LCO by inserting oxygen. In the case of metal dopant, the replaced metal will immobile in the structure. Different with metal dopant, oxygen will occupy interstitial site due to its small atomic radius, hence it is very mobile in the structure.[27] For each oxygen interstitial introduced, two Cu^{2+} ions become Cu^{3+} ions. Wells et al. proposed phase diagram for oxygen doped of LCO [see Figure 1.9 (b)],[27] even though there are still many miscibility gaps and needs further investigation for oxygen doped LCO. There are two main

regions: (1) oxygen poor phase ($y < 0.01$) and (2) oxygen rich phase ($y > 0.55$). In the region of oxygen poor phase (stage 1), the structure is still orthorhombic phase, similar with the undoped LCO. In the case of oxygen rich phase region (stage 5), superconductivity occurs and the authors proved that the structure has an additional super lattice peaks. The authors also could synthesized sample up to $y \sim 0.1$ and proposed the staging behavior in $y > 0.55$ (stage 4, 3 and 2), but the exact oxygen is not measured. Preliminary result showed that at these stages, the LCO still exhibits superconductivity, with T_c as high as 45 K. Upon doping of LCO by metal/oxygen to the superconducting region level, the material showed metallic property, with resistivity decreases to zero at temperature below T_c.[42,43)]

1.6.2. Strontium titanate (STO)

Strontium titanate ($SrTiO_3$/STO) is a perovskite oxide material contains divalent Sr and tetravalent Ti. The crystal structure of STO is cubic at room temperature, and every Sr^{2+} ions are enclosed with four TiO_6 octahedral, as illustrated previously in Figure 1.7 (ABO_3 structure). STO undergoes phase transitions from cubic to tetragonal at 105 K,[44)] continued by the transition of tetragonal to orthorhombic at 37 K.[45)]

STO is a promising material to be used in oxide electronic device, owing to its high dielectric constant and wide band gap. The indirect and direct band gap of STO are about 3.25 and 3.75 eV, respectively.[46)] At room temperature, STO has high dielectric constant,[47)] therefore prospect to be utilized as good insulator and high charge storage capacitor.[48)] In the case of electric properties, the increase of oxygen vacancies on STO were reported enhancing the conductivity.[49)] At certain electron doping level, even STO is also possible to exhibit superconducting property.[50)] Additionally, since STO is an excellent substrate for epitaxial growth of various oxide based thin films, physics of oxide heterostructure based on STO material is also driven interest of researchers in the past years.[51)] Epitaxial growth is assigned as a method to grow another thin film on a substrate, where the overlaying material is expected to have the same

crystalline orientation with the substrate used. For example, complex oxide $LaAlO_3/SrTiO_3$ at the interface exhibits superconductivity.[52] Grown STO on Si substrate could be used as gate dielectric material.

1.7. Synthesis of perovskite oxide

Various method have been employed to synthesize perovskite oxide. The most common synthesis methods includes solid-state, co-precipitation, hydrothermal, spray pyrolysis and sol-gel. In the case of solid-state process, the process started by combining two or more oxide powders/carbonates/salts mechanically, and continued by heating at temperature at above 1000 ℃. At elevated temperature, diffusion of each solids ions toward to the interface occurs to form new mixed oxide. Moreover, co-precipitation is a conversion process from the soluble substance in the solution into an insoluble (solid) by addition of another chemical (precipitant).[53] The reaction between the precipitant and the solution forms a precipitate which can be extracted out and removed, and subjected to heat treatment.

There are also techniques of perovskite synthesis but additional set up of experiment must be installed such hydrothermal and spray pyrolysis. Hydrothermal process involves the combination of critical temperature of the material with boiling temperature of water or another solution synthesis (typically water is used) and usually done in special set up high pressure vessel.[54] Spray pyrolysis uses based on fast vaporization of metal precursors in the form of small droplets and sprayed to a heated surface. Among perovskite synthesis methods above, the comparison is summarized in Table 1.1. Here, sol-gel is selected and is explained more deeply in subchapter 1.8.

Table 1. 1 Comparison of perovskite oxide synthesis method[54,55)]

Synthesis Method	Homo-geneity	Product size (nm)	Purity	Synthesis Temperature	Agglo-meration
Solid-state	Poor	> 1000	Poor	1000 ℃	Moderate
Co-precipitation	Good	> 10	Good	500-1000 ℃	High
Sol-gel	Very good	> 10	Very good	500-1000 ℃	Moderate
Hydrothermal	Very good	> 100	Very good	80-400 ℃ + High Pressure	Low
Spray Technique	Very good	> 10	Very good	700-1000 ℃	Low

1.8. Sol-gel

Sol-gel chemistry is a ceramics synthesis via modification of liquid precursors through sol formation to a network structure called a gel.[62)] Solids and another solids matter does not react each other except there is sufficient energy is supplied. The view point of sol-gel synthesis is to dissolve compound in a liquid and turn it again to a solid, accordingly multi component compound with a controlled stoichiometry can be fabricated. Sol-gel has attracted attention researchers in the world since it offers considerable advantages such as high purity of product, good homogeneity, and controllability of product size with the ability to be shaped in various form.[56)] Sol-gel comprises gradual processes whereby the development of ceramics will follow several stages: 1) synthesis of sol, 2) formation of gel, 3) drying the gel and 4) heat treatment, as illustrated in Figure 1.11.

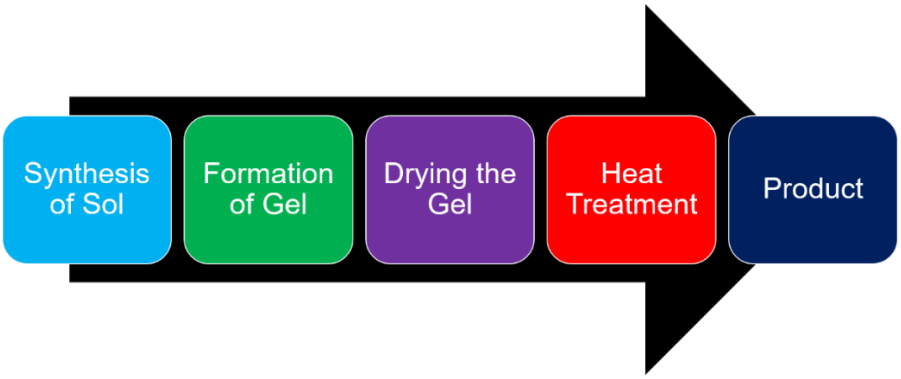

Figure 1. 11 Stages in sol-gel process

1.8.1. Synthesis of sol

Sol is a chemical reaction where two or more substances are combined together to form a colloid. The precursors used usually are metal alkoxides (M-OR, M is the metal atom and R is organic substituent), such as metal nitrate, metal citrate or metal chloride. The chemical bonding of the precursors is subjected to be raveled through hydrolysis (Equation 1.2) and polycondensation (Equation 1.3 and Equation 1.4), leads to the formation of M-OH and M-O-M. The reaction initially undergo in the presence of water, and the rate can be controlled when acid/base catalyst. Buckley and Greenbalt reported that acidic condition favored slower hydrolysis compared to base condition, but served finer product.[57] Accordingly, this stage is affected by the ratio of water to the precursor as well as the concentration of the catalyst.

Hydrolysis

$$M-OR+H_2O \rightarrow M-OH+R-OH$$

…….(1.2)

Polycondensation

$$M-OR+M-OH \rightarrow M-O-M+R-OH \quad \text{.....(1.3)}$$

$$M-OH+M-OH \rightarrow M-O-M+H_2O \quad \text{.....(1.4)}$$

1.8.2. Formation of gel

Gel is a semi rigid mass, forms when the sol starts to evaporate and the particles merge together creating a network. This stage involves syneresis or aging, where the continued condensation leads to increased viscosity of the precursors. In most alkoxide systems, the sol should be aged for a few hours to a few days. Organic molecules are added as chelating agent and/or fuel, to enhance the stability of the precursors, enhancing metal ion binding, as well as prevent precipitation of individual hydroxides. Every organic molecules used behave differently to the reaction and influence the end of products. Citric acid (CA) is the common used as the fuel, since it is inexpensive, abundant and effective chelating agent.[56] Rudissil et al. studied the effect of chelating agent

(CA, ethylene glycol (EG), malic acid (MA) and glycerin (G)) on the morphology of $Ce_{0.5}Mg_{0.5}O_{1.5}$ and the SEM images are presented in Figure 1.12.[58] It can be seen that the morphology is varied as the chelating agent is changed. As CA was used in the synthesis [Figure 1.12 (a) and (b)], sphere like particles formed and by replacing CA, the morphology became merged together [Figure 1.12 (c) and (d)].

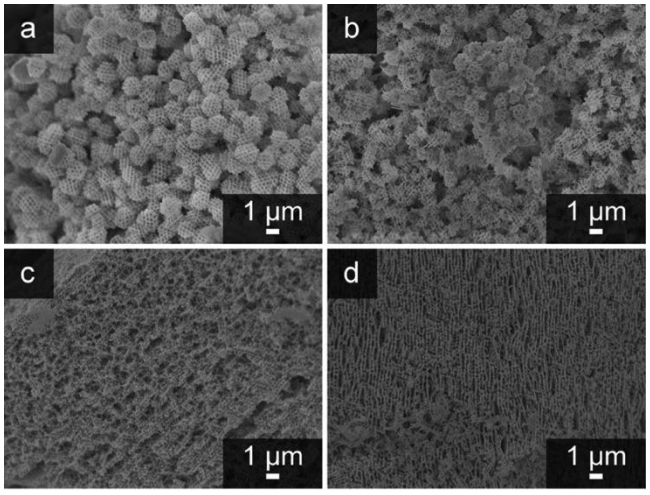

Figure 1. 12 SEM images of $Ce_{0.5}Mg_{0.5}O_{1.5}$ samples prepared at a 2:1:1 molar ratio of: (a) EG :CA:TMI (total metal ions), (b) G:CA:TMI, (c) EG:MA:TMI and (d) G:MA:TMI. (Reprinted with permission from American Chemical Society)

Moreover, tuning the pH is also crucial to keep the homogeneity and stability of solutions. Generally, ammonia based compounds (ammonia, urea, ammonium hydroxide, ethylene diamine) are used, since it supplies N to the precursors and enhancing combustion process during heat treatment in the next step.[56] Precursor's pH also influences the aging time and how glassy is the gel. By controlling the viscosity, a variety of shape can easily be controlled.

1.8.3. Drying the gel

After homogeneous networking gel is formed, drying the gel is necessary since now the metals are well bonded. Drying serves removing the liquid phase from the gel and volume shrinkage occurs. Typically, water is the product after

condensation process, then evaporation of water can be done by heating at temperature > 100 ℃.

1.8.4. Heat treatment

Formation of most metal oxides requires heat treatment otherwise precipitation of individual hydroxides and/or amorphous oxides will remain. Heat treatment purposes on: 1) removal of M-OH surface, 2) decomposition of organic matters and 3) crystallization. Annealing at low temperature at about 200-400 ℃ is probably necessary to decompose all the organic matter before further crystallization at higher temperature. Mali et al. confirmed the decomposition in their work nitrate-citrate sol-gel based compound, indicating by large weight loss of about 70 % at 205 ℃ from thermogravimetric analysis (TGA) result.[59] Crystallization on occurs at about 400-900 ℃, depends on the nature of material itself. Joshi et al. studied the effect of annealing temperature on the formation of $Zn_{0.95}Cr_{0.05}O$ NPs and reported that higher annealing temperature provides bigger particle.[60] TEM images in Figure 1.13 shows that particle size of the synthesized sample at 450, 600, and 700 ℃ are found to be about 10–20 nm [Figure 1.13 (a)], 10–30 nm [Figure 1.13 (b)] and 10–35 nm [Figure 1.13 (c)], respectively.

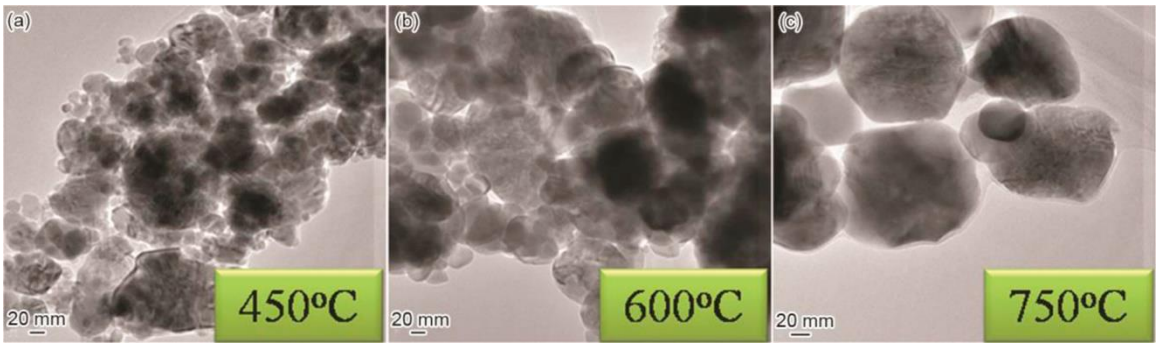

Figure 1. 13 TEM images of $Zn_{0.95}Cr_{0.05}O$ NPs annealed at: (a) 450, (b) 600 and (c) 700 ℃[60] (Reprinted with permission from Elsevier).

1.9. Problem statement

The present work is aimed for the formation of free-standing LCO and STO NPs through sol-gel technique and to investigate its electric/magnetic properties is investigated. The structure formed (i.e. NPs) has advantages since it has high surface area, therefore the change of properties compared to their bulk is expected. Sol-gel is selected as the synthesis method considering the homogeneity and purity is high and size is controllable. Hydrothermal and spray technique may the best choice in term of product, but the experiments need additional set up, impact to the cost of set up. Therefore, here, sol-gel is considered the best choice since it is a chemical synthesis, the cost will be less expensive. By using this method, the size of LCO and STO NPs is aimed on controlling the size of NPs.

Size dependent magnetic/electric properties on nano-sized LCO based compound is investigated here. LCO is an AF Mott insulator, means it holding important properties in strong correlated system. One of the most important applications in such strong correlated system is superconductivity, even though the nature of the material is still metal oxide and antiferromagnetic material, thus which offering more widely applications. In the case of cuprate, superconducting transition temperature can be pinned by adding more layers of CuO, such in $YBa_2Cu_3O_7$ and $HgBa_2Ca_2CuO_3O_y$. Therefore, here also remain understanding on how the electric and magnetism changed in nano-sized of such strong correlated system. LCO is considered the best prototype to be studied, since it has simple structure (only single CuO layer), and, to date, there are still limited information for synthesis of LCO NPs and its properties. Therefore, controlling the magnetic and electric properties of nano-sized AF Mott insulator material is essentially fundamental and might also related on understanding to others cuprate or strong correlated system.

Moreover, electrical properties of free-standing of STO NPs is also studied. Various electric properties based on STO material is ranging from insulator to metal, memristive behavior, ferroelectric, and, even to superconductivity, which makes the material important and very potential to be utilized for future

electronic device applications. So far the most interest studies of STO is the physics of STO based heterostructure in the form of thin film, where the oxide interface give arises to unique electrical properties. In the case of free-standing, only limited to dielectric properties was reported since STO has wide band gap and potentially to be used as capacitor. By controlling the properties of free-standing STO NPs, the result obtained become essential and fundamental for further research work in nano-sized heterostructure or other nano-electronic device applications.

1.10. Objectives study

The main aims of this research are:

1. To find an optimum condition to synthesize the controlled size of free-standing LCO and STO NPs based compound by sol-gel method.
2. To investigate the magnetic and/or electric properties of the synthesized STO and LCO NPs based compound.

1.11. Research scope

In this research work, the main aspects to discuss are the electric and/or magnetic properties of LCO NPs and STO NPs based compound synthesized by sol-gel method. The scope of this study covered:

1. The LCO NPs and STO NPs based compound were synthesized by sol-gel method. Aspect was studied in synthesis process is how to control the material size to nanoscale.
2. The LCO NPs were characterized by Field Emission Scanning Electron Microscopy (FESEM), X-ray Diffractometry (XRD), and Transmission Electron Microscopy (TEM).
3. The electric properties of the samples were investigated based on trapping low temperature probing system. Prior to this measurement, the LCO NPs were assembled at electrodes by DEP method. The electrodes itself was fabricated by electron beam lithography (EBL).

4. The magnetic properties of the samples were measured by superconducting quantum interference device (SQUID) magnetometer.
5. At this moment, the oxidation state of sample is temporary put as future work and will be analyzed by X-ray photoelectron spectroscopy.

1.12. Outline of thesis

This thesis is consisted of eight chapters. Chapter one explains the introduction and literature review covering the theory and literature related to the involved works, research motivation, objectives and study scope of this work. Chapter two deals with the materials, chemicals used and experimental procedures. This chapter includes the design of experiment, synthesis process of LCO and STO NPs by sol-gel process as well as the experimental set-up of electric and magnetic properties measurement. The characterization techniques and its working principle are also included in this chapter. Chapter three, four, five, six and seven focus on presenting the overall results and analysis in the form of journal template. The chapters are organized to introductory paragraph, experimental procedure, results and discussion, conclusion. Chapter eight states the conclusion of this research work as well as some suggestions and recommendations.

1.13. References

1) T. ISO, Nanoparticle, nanofibre and nanoplate. (2008).
2) D.L. Schodek, P. Ferreira and M.F. Ashby, Nanomaterials, nanotechnologies and design: an introduction for engineers and architects (Butterworth-Heinemann, Oxford, U.K., 2009).
3) S. Barth, F. Hernandez-Ramirez, J.D. Holmes and A. Romano-Rodriguez, Prog. Mater. Sci. 55, 563 (2010).
4) T.P. Yadav, R.M. Yadav and D.P. Singh, Nanosci. Nanotechnol. 2, 22 (2012).
5) A. Biswas, I.S. Bayer, A.S. Biris, T. Wang, E. Dervishi and F. Faupel, Adv. Colloid Interface Sci. 170, 2 (2012).

6) A.G. Kolhatkar, A.C. Jamison, D. Litvinov, R.C. Willson and T.R. Lee, Int. J. Mol. Sci. 14, 15977 (2013).
7) M. Ivanovskaya, E. Ovodok and V. Golovanov. Chem. Phys. 457, 98 (2015).
8) O. Iglesias and A. Labarta, Phys. Rev. B. 63, 184416 (2001).
9) L.H. Bennett, C. H. Page, & L. J. Swartzendruber, J Res of the National Bureau of Standards 83, 9-12 (1978).
10) S. K. Giri, A. Poddar, A., & T. K. Nath, T. K., J Appl. Phys. 112, 113903 (2012).
11) Y. Tang, D.J. Smith, B. Zink, F. Hellman and A. Berkowitz, Phys. Rev. B 67, 054408 (2003).
12) T.-J. Park, G.C. Papaefthymiou, A.J. Viescas, A.R. Moodenbaugh and S.S. Wong, Nano Lett. 7, 766 (2007).
13) R. Bhowmik, R. Nagarajan and R. Ranganathan, Phys. Rev. B 69, 054430 (2004).
14) X. Zheng, C. Xu, K. Nishikubo, K. Nishiyama, W. Higemoto, W. Moon, E. Tanaka and E.S. Otabe, Phys. Rev. B 72, 014464 (2005).
15) N. Rinaldi-Montes, P. Gorria, D. Martínez-Blanco, A.B. Fuertes, I. Puente-Orench, L. Olivi and J.A. Blanco, AIP Adv. 6, 056104 (2016).
16) A. Jayendran and R. Jayendran, Englisch für Elektroniker (Springer, Wiesbaden, 1996).
17) E.H. Rhoderick, IEE Proc.-Solid-State Electron Dev. 129, 1 (1982).
18) G. Greco, F. Iucolano and F. Roccaforte, Appl. Surf. Sci. 383, 324 (2016).
19) Z. Wang, S. Tsukimoto, M. Saito, K. Ito, M. Murakami and Y. Ikuhara, Phys. Rev. B 80, 245303 (2009).
20) R. Pethig, A. Menachery, S. Pells and P. De Sousa, BioMed Res. Int. 2010, (2010).
21) A. Alazzam, B. Mathew and F. Alhammadi, J Sep. Sci. 40, 1193 (2017).
22) M. Elitas, N. Dhar, K. Schneider, A. Valero, T. Braschler, J. McKinney and P. Renaud, Biomed. Phys. Eng. Express. 3, 015005 (2017).

23) L. Yang, P.P. Banada, A.K. Bhunia and R. Bashir, J. Biol. Eng. 2 [1], 6 (2008).
24) D. Wang, R. Zhu, Z. Zhou and X. Ye, Appl. Phys. Lett. 90, 103110 (2007).
25) J. Zhu, H. Li, L. Zhong, P. Xiao, X. Xu, X. Yang, Z. Zhao and J. Li, ACS Catal. 4, 2917 (2014).
26) K. Szot, W. Speier, G. Bihlmayer and R. Waser, Nat. Mater. 5, 312 (2006).
27) B. Wells, Y. Lee, M. Kastner, R. Christianson, R. Birgeneau, K. Yamada, Y. Endoh and G. Shirane, Sci. 277, 1067 (1997).
28) P.A. Lee, N. Nagaosa and X.-G. Wen, Rev. Mod. Phys. 78, 17 (2006).
29) F. Zhou: Growth and Characterization of Bulk Superconductor Material (Springer, Switzerland, 2016)
30) R. Hord, G. Cordier, K. Hofmann, A. Buckow, G. Pascua, H. Luetkens, L. Alff and B. Albert, Z. Anorg. Allg. Chem. 637, 1114 (2011).
31) Y. Imai, M. Kato, Y. Takarabe, T. Noji and Y. Koike, Chem. Mater. 19, 3584 (2007).
32) A. Mourachkine, Room-temperature superconductivity (Cambridge Int Sci. Publishing, U.K., 2004).
33) J. Budnick, A. Golnik, C. Niedermayer, E. Recknagel, M. Rossmanith, A. Weidinger, B. Chamberland, M. Filipkowski and D. Yang, Phys. Lett. A. 124, 103 (1987).
34) J. Saylor, L. Takacs, C. Hohenemser, J. Budnick and B. Chamberland, Phys. Rev. B. 40, 6854 (1989).
35) V.G. Storchak, J.H. Brewer, D.G. Eshchenko, P.W. Mengyan, O.E. Parfenov, A.M. Tokmachev and P. Dosanjh, Phys. Rev. B. 94, 134407 (2016).
36) S.-i. Uchida, H. Takagi, H. Yanagisawa, K. Kishio, K. Kitazawa, K. Fueki and S. Tanaka, Jpn. J Appl. Phys. 26, L445 (1987).
37) R.P. Singh and M. Singh, Phys. Rev. B. 51, 6754 (1995).

38) R. Cava, R. Van Dover, B. Batlogg and E. Rietman, Phys. Rev. Lett. 58, 408 (1987).
39) Y.H. Lin, Y. Liu, B.P. Zhang, C.W. Nan, J.F. Li and Z. Shen, J Am. Ceram. Soc. 90, 4005 (2007).
40) K.A. Müller and J.G. Bednorz, Sci. 237, 1133 (1987).
41) Z. Guguchia, A. Maisuradze, G. Ghambashidze, R. Khasanov, A. Shengelaya and H. Keller, New J Phys. 15, 093005 (2013).
42) S. Smadici, J. Lee, S. Wang, P. Abbamonte, G. Logvenov, A. Gozar, C.D. Cavellin and I. Bozovic, Phys. Rev. Lett. 102, 107004 (2009).
43) M. Hundley, J. Thompson, S. Cheong, Z. Fisk and J. Schirber, Phys. Rev. B. 41, 4062 (1990).
44) E. Salje, M. Gallardo, J. Jiménez, F. Romero and J. Del Cerro, J Phys. Condens. Matter 10, 5535 (1998).
45) A.K. Bain and P. Chand: Ferroelectrics: Principles and Applications (John Wiley & Sons, Germany, 2017).
46) K. Van Benthem, C. Elsässer and R. French, J. Appl. Phys. 90, 6156 (2001).
47) F. Pontes, E. Lee, E. Leite, E. Longo and J.A. Varela, J Mater. Sci. 35, 4783 (2000).
48) M. Popovici, B. Kaczer, V.V. Afanas' Ev, G. Sereni, L. Larcher, A. Redolfi, S.V. Elshocht and M. Jurczak, Phys. Status Solidi (RRL)– Rapid Res. Lett. 10, 420 (2016).
49) H. Trabelsi, M. Bejar, E. Dhahri, M. Sajieddine, K. Khirouni, P. Prezas, B. Melo, M. Valente and M. Graça, J Alloys Compd. 723, 894 (2017).
50) A. Stucky, G. Scheerer, Z. Ren, D. Jaccard, J.-M. Poumirol, C. Barreteau, E. Giannini and D. van der Marel, Sci. Rep. 6, 37582 (2016).
51) Y.-Y. Pai, A. Tylan-Tyler, P. Irvin and J. Levy, Rep. Prog. Phys. 8, 036503 (2018).
52) H. Esmailzadeh and A.G. Moghaddam, Physica C 548, 123 (2018).
53) J. Guertin, C.P. Avakian and J.A. Jacobs: Chromium (VI) handbook (CRC press, U.S.A., 2016).

54) D.D. Athayde, D.F. Souza, A.M. Silva, D. Vasconcelos, E.H. Nunes, J.C.D. da Costa and W.L. Vasconcelos, Ceram. Int. 42, 6555 (2016).
55) P. Cousin and R. Ross, Mater. Sci. Eng. A. 130, 119 (1990).
56) A. Danks, S. Hall and Z. Schnepp, Mater. Horizons. 3, 91 (2016).
57) A. Buckley and M. Greenblatt, J Chem. Edu. 71, 599 (1994).
58) S.G. Rudisill, S. Shaker, D. Terzic, R.g. Le Maire, B.-L. Su and A. Stein, Inorg. Chem 54, 993 (2014).
59) A. Mali and A. Ataie, Scripta Mater. 53, 1065 (2005).
60) Z. Joshi, D. Dhruv, K. Rathod, J. Markna, A. Satyaprasad, A. Joshi, P. Solanki and N. Shah, J Mater Sci. Technol. 34, 488 (2018).

CHAPTER 2

Methodology

2.1. Introduction

This chapter explains the information of the raw chemicals, materials and the experimental procedure of this research works. This chapter is divided into three main parts: (1) materials and chemicals used, (2) the procedure for sample synthesis, (3) the characterizations of the fabricated sample including electric and/or magnetic property measurements. The experimental procedure of this research work is illustrated by flow chart in Figure 2.1.

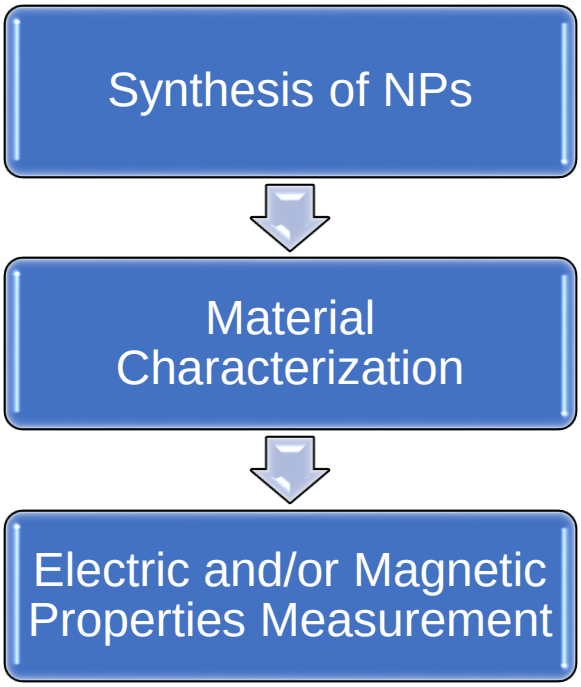

Figure 2. 1 Flow process of this experimental work

2.2. Chemical and materials

The materials and chemical used in this research are presented in Table 2.1

Table 2. 1 Summary of chemicals and materials used

Chemical Name	Chemical Formula	Function	Supplier	Remarks
Lanthanum Oxide	La_2O_3	Precursors	Sigma Aldrich	Purity: 99.9% MW: 325.81 gr/mol
Cupric Oxide	CuO	Precursors	Wako	Purity: 99.9% MW: 79.55 gr/mol
Strontium Carbonate	$SrCO_3$	Precursors	Sigma Aldrich	Purity: 99.9% MW: 147.63 gr/mol
Tetraisopropyl Titanate	$C_{12}H_{28}O_4Ti$	Precursors	Tokyo Chemical Industry	Purity: 97% MW: 284.2153 gr/mol
Nitric Acid	HNO_3	Solvent	Wako	Concentration: 70% MW: 63.01 gr/mol
Ethylene Glycol	$C_2H_6O_2$	Surfactant	Wako	Purity: 99.5% MW: 62.07 gr/mol
Citric Acid Monohydrate	$C_6H_8O_7.H_2O$	Surfactant	Wako	Purity: 99.5% MW: 210.14 gr/mol
Ammonia Solution	NH_3 (aq)	pH Adjustment	Wako	Concentration: 28% MW: 17.03 gr/mol
Ethanol	C_2H_6O	Solvent	Wako	Purity: 99.5% MW: 46.07 gr/mol
Isopropanol	$(CH_3)_2CHOH$	Cleansing Agent	Kanto Chemical	Purity: 99.9% MW: 60.10 gr/mol
Anisole (gL 2000-M)	C_7H_8O	Electron Beam Resist	Kanto Chemical	Purity: 89% MW: 108.14 gr/mol
n-Amyl Acetate (ZED N-50)	$C_7H_{14}O_2$	Developing Agent	Zeon Chemical	Purity: 100% MW: 130.19 gr/mol
4-Methyl-2-Pentanone	$C_6H_{12}O$	Developing Agent	Kanto Chemical	Purity: MW: 100.16 gr/mol
Dymethil Sulfoxide	$(CH_3)_2SO$	Lift-off Solution	Kanto Chemical	Purity: 99% MW: 78.14%

2.3. Synthesis of LCO

A stoichiometric amount of La_2O_3 and CuO powders were used as raw materials. Due to possibility interaction to air, the La_2O_3 was first dried at 700 ˚C

for 2 h. The dried La_2O_3 and CuO powders then were dissolved in an appropriate amount of HNO_3 separately to achieve the nitrate forms ($La_2(NO_3)_3$ and $Cu(NO_3)_2$). These solutions were mixed under continuous magnetic stirring until the color changed to light blue. The organic matters used were citric acid and ethylene glycol with mass ratio 3:2 and the pH of the solution was adjusted to 7 by NH_3 water solution. First, the solution precursor was evaporated at 150 ℃ for 1 h and continued at 300 ℃ for 3 h to decompose all the organic matters. Thereafter, crystallization was then performed by further post-annealing at 500-800 ℃ with heating rate 10 ℃/min, as illustrated in Figure 2.2. The final product was ground for 1 h using agate mortar until obtaining well-homogeneous fine powder. The overall synthesis process is illustrated in Figure 2.3.

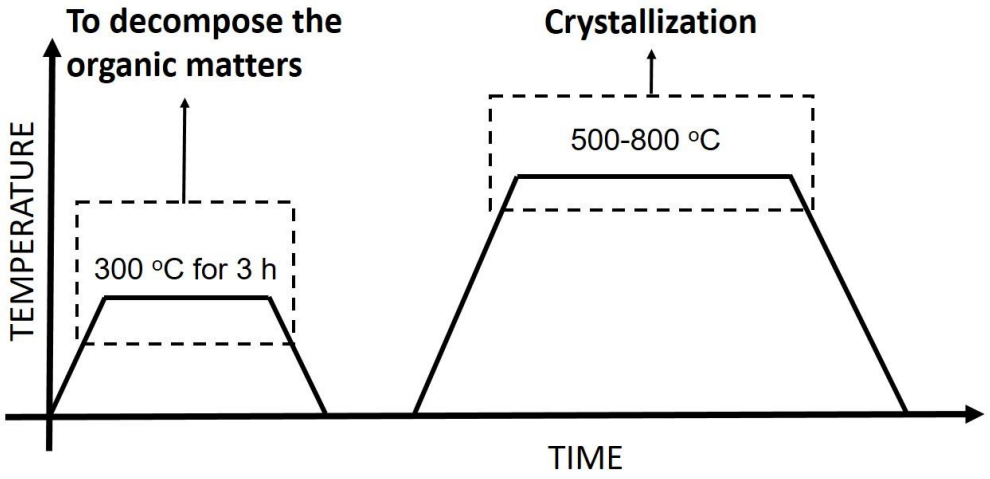

Figure 2. 2 Annealing profile of LCO NPs synthesis in this research work

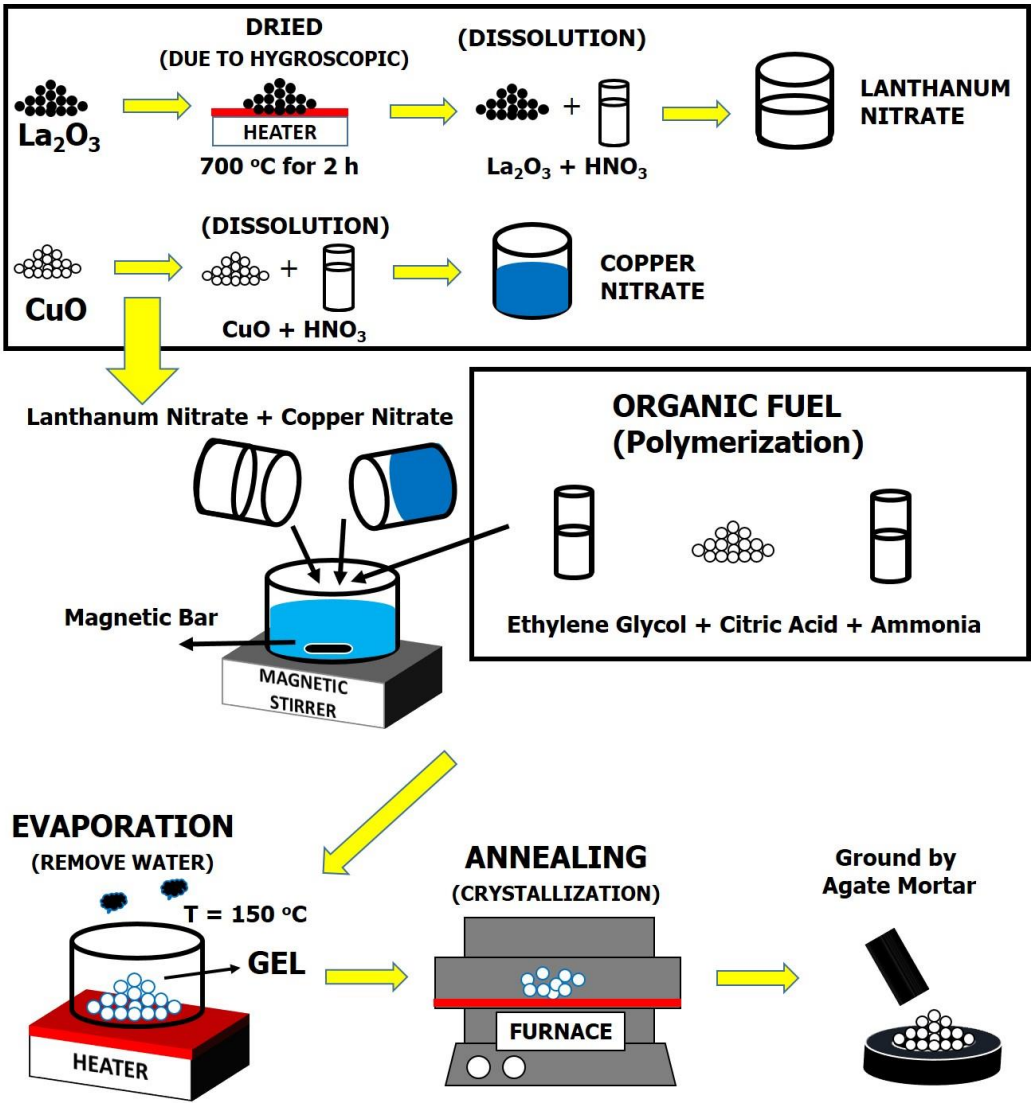

Figure 2. 3 Schematic illustration of LCO NPs synthesis by sol-gel method

2.4. Synthesis of $La_{2-x}Sr_xCuO_4$

Several $La_{2-x}Sr_xCuO_4$ (x = 0.2) (LSCO) samples with different particle size were synthesized by same process as explained in Section 2.3. The different part is only in starting material, with the addition of Sr. Raw materials and mole ratio used in this work is listed in Table 2.2.

Table 2. 2 Raw materials and mole ratio calculation

Raw Materials	**La_2O_3**	**$SrCO_3$**	**CuO**
Mole Ratio	2-x	x	1.00

2.5. Synthesis of La_2CuO_{4-y}

To study the effect of electron doping, the LCO samples were subjected by post-annealing under Ar, to obtain La_2CuO_{4-y} (LCO_{4-y}), respectively. Several LCO samples were placed in the furnace and post-annealing was done with heating up rate 10 °C/min at 450 °C for 24 h. Before the annealing is started, argon gas was supplied into the furnace first for 15 min, to remove the air existed in the furnace. The Ar flow was stopped when the temperature was naturally cooled down to room temperature.

2.6. Synthesis of STO

A stoichiometric amounts of $SrCO_3$ and $C_{12}H_{28}O_4Ti$ as starting materials were dissolved in an appropriate amount of diluted citric acid (CA) solution at 80 ℃, to yield metal citrate as a precursor. Then, CA and ethylene glycol (EG) at a mass ratio of 3:2 were added into the precursor with magnetic stirring. The mixed precursor was heated at 150 ℃ followed by annealing at 400-800 ℃ for 5 h in air, and grinding for about 1 h using an agate mortar to obtain very fine powders. The impurity phase existing in the sample was removed by washing with 5% HNO_3 solution. The overall process of STO synthesis is illustrated in Figure 2.4.

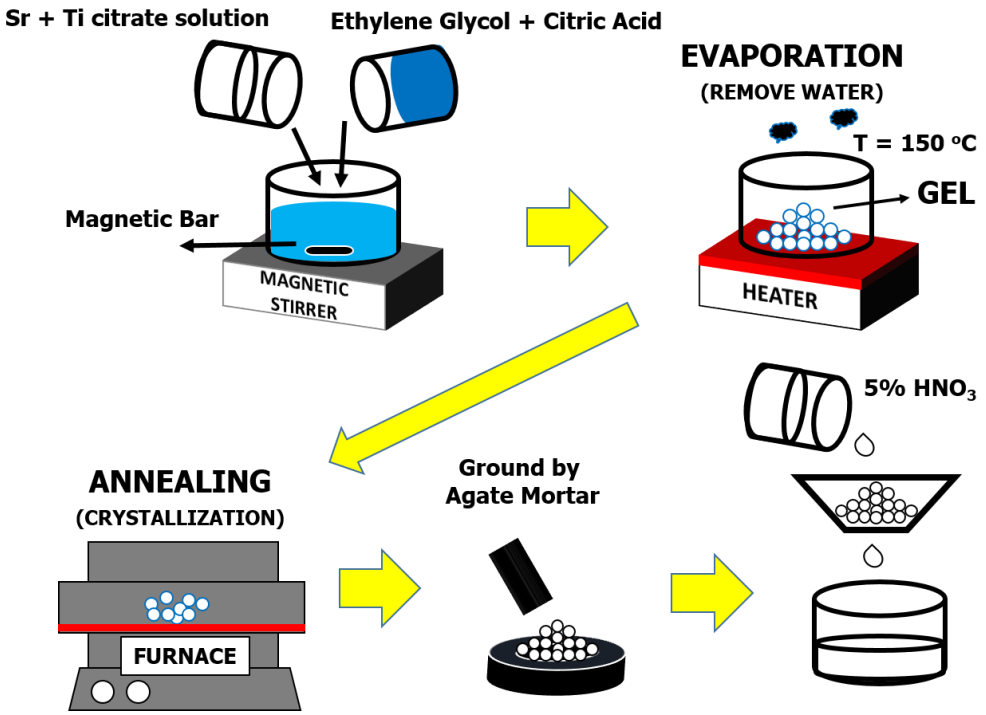

Figure 2. 4 Schematic illustration of STO synthesis by sol-gel method

2.7. Parameter studied in LCO and STO synthesis

In this parameter, the annealing temperature was varied from 400 to 800 °C. The samples were placed in a furnace and were annealed with heating up rate 10 °C/min and naturally cooled down to room temperature. The purpose of this parameter is to investigate the minimum annealing temperature needed to synthesize LCO and STO phase. The summary of this parameter is presented by Table 2.3, Table 2.4 and Table 2.5.

Table 2. 3 Summary of parameters used to study the effect of annealing temperature in LCO synthesis

Variable Condition		Fixed Condition
Annealing Temperature	500 °C 600 °C 700 °C 800 °C	Pre-annealing: 300 °C for 3 h Synthesis pH: 7 Annealing environment: Air Heating up rate: 10 °C/min Heating down rate: Naturally cooled to room temperature Annealing Time: 3 h

Table 2. 4 Summary of parameters used to study the effect of annealing time in LCO synthesis

Variable Condition		Fixed Condition
Annealing Time	0 min	Annealing environment: Air Heating up rate: 10 °C/min Heating down rate: Naturally cooled to room temperature Annealing Temperature: 600 °C
	45 min	
	90 min	
	180 min	

Table 2. 5 Summary of parameters used to study the effect of annealing temperature in STO synthesis

Variable Condition		Fixed Condition
Annealing Temperature	400 ℃	Synthesis pH: 2 Annealing environment: Air Heating up rate: 10 °C/min Heating down rate: Naturally cooled to room temperature Annealing Time: 5 h
	500 ℃	
	600 ℃	
	700 ℃	
	800 ℃	

2.8. Characterization

Several characterization techniques were performed to know the properties of fabricated sample. The morphology of LCO and STO NPs was observed by Field Emission Scanning Electron Microscope (FESEM). For advance morphology observation, Transmission Electron Microscope (TEM) was used. For phase identification purpose, the sample was examined by X-ray Diffraction Spectrometry (XRD) method.

2.8.1. Scanning electron microscopy

Scanning electron microscopy (SEM) is an imaging characterization technique used to obtain the information of about morphology and topography of a material.[1)] The working principle of this technique is started with the generation of very high field emission electron by electron gun which

furthermore the beam will be adjusted by a magnetic coil to scan the sample. In this research work, the morphology of the synthesized LCO and STO was observed by field-emission scanning electron microscope (FESEM) model Hitachi S-5200 and/or S-3400 (see Figure 2.5) with acceleration voltage at 5 KV. The observation were performed by ranging the image magnification from 1,000-50,000 times.

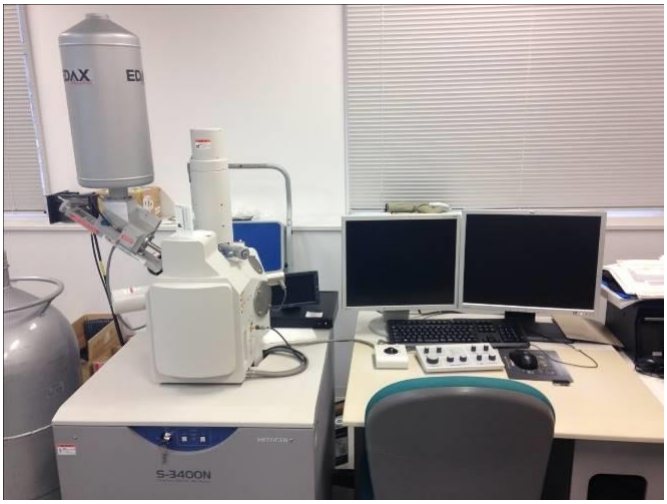

Figure 2. 5 Photograph of SEM machine

For quantitative analysis, the FESEM images was examined by Image J Software to measure the diameter of the sample. The diameter was measured from one end opposite to the top surface of each particle. In this thesis, all the measurement values using the average value of data.

2.8.2. X-ray diffraction spectrometry

X-ray diffraction (XRD) is one quantitative and qualitative characterization techniques used to analyze crystalline material.[1)] The working principle of this method is based of incident x-ray beam with wavelength λ that bombard lattice planes in a crystal planes at an angle θ. This process can be described by Bragg's Law as expressed in equation 2.1.

$$n\lambda = 2d \sin\theta \quad \text{..... (2.1)}$$

Where n is integer number, λ is the wavelength of x-ray radiation, d is the distance of lattice planes and θ is the angle of incident beam and lattice planes. In this research work, x-ray diffractometer (Rigaku RINT-2100) with Cu Kα radiation 40 kV (λ = 0.154 nm) was used for phase and crystal analysis of the sample. The scanning rate was 0.02 °/s. The XRD machine used is displayed in Figure 2.6.

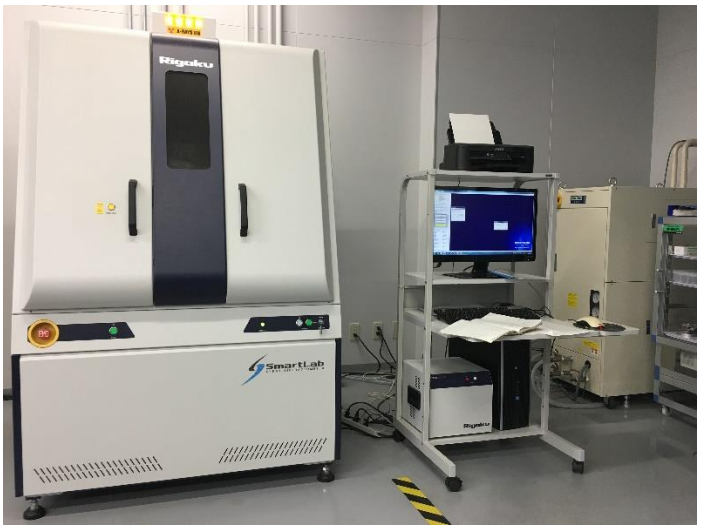

Figure 2. 6 Photograph of XRD machine

The average crystallite size was calculated using the Scherrer equation (Equation 2.2):

$$D = \frac{k\lambda}{\beta cos\theta} \quad \text{..... (2.2)}$$

where D is the crystallite size, k is the Scherrer constant (0.9), λ is the wavelength of Cu Kα, and β is the full-width at half maximum (FWHM) of XRD peaks which corresponds to the difference in FWHM of measured diffraction peaks, and the FWHM of an ideal crystal.

2.8.3. Electric property measurement

2.8.3.1. Nanogap electrode fabrication

A nanoscale gap electrode was fabricated via EB lithography method, with SiO_2 as the substrate. Firstly, the device pattern was designed by software AutoCAD before the process. After that, EB resist solution (gL 2000:anisole = 1:1) was spin coated to the substrate with speed 5000 rpm for 40 s and pre-baked at 180 ℃ for 3 min. The electrode patterning was performed by EB machine model Elionix ELS-7500, as shown in Figure 2.8. The beam amplitude was 30 nA and developed by ZED-N 50 solution for 5 min continued by MIBK:IPA for 15 sec, then rinsed by distilled water. The material of electrode was Pt/Ti with thickness 24/6 nm that depositing by sputtering machine model Miller CFS-4EP-LL. The resist then was removed by dimethyl-sulfoxide at 80 ℃ for 40 min under sonication process. Overall EBL process is illustrated in Figure 2.8.

Figure 2. 7 Photograph of EBL machine

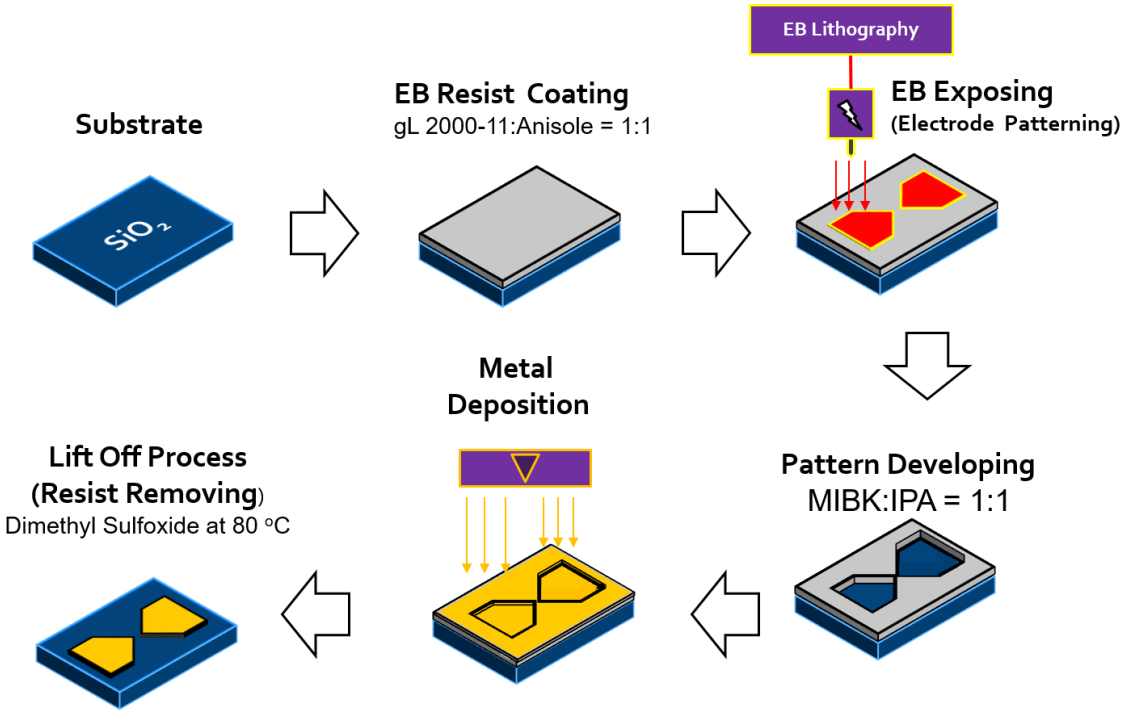

Figure 2. 8 Schematic illustration of nano gap electrode fabrication by EBL

2.8.3.2. Dielectrophoresis

The LCO NPs and STO NPs were assembled at the edge of electrodes by dielectrophoresis (DEP) method. Firstly, small amount of the LCO and STO NPs powder was diluted into ethanol. Centrifugation was performed to the suspension, prior to avoiding the agglomeration of particles. Secondly, the suspension then was casted to the electrode device and wait until dried naturally, as illustrated in Figure 2.9. During casting, AC voltage was applied by function waveform generator model WW 2074 manufactured by Tabor Electronics on an electrode to generate the non-uniform electric field, with phase difference 180°. The voltage and frequency used were V_{pp} = 10 V and f = 1 MHz respectively. The trapping process was finished if the cast solution have dried. After that, the device was heated at 450 °C under Ar atmosphere, prior to improve the electrical contact between electrodes and sample

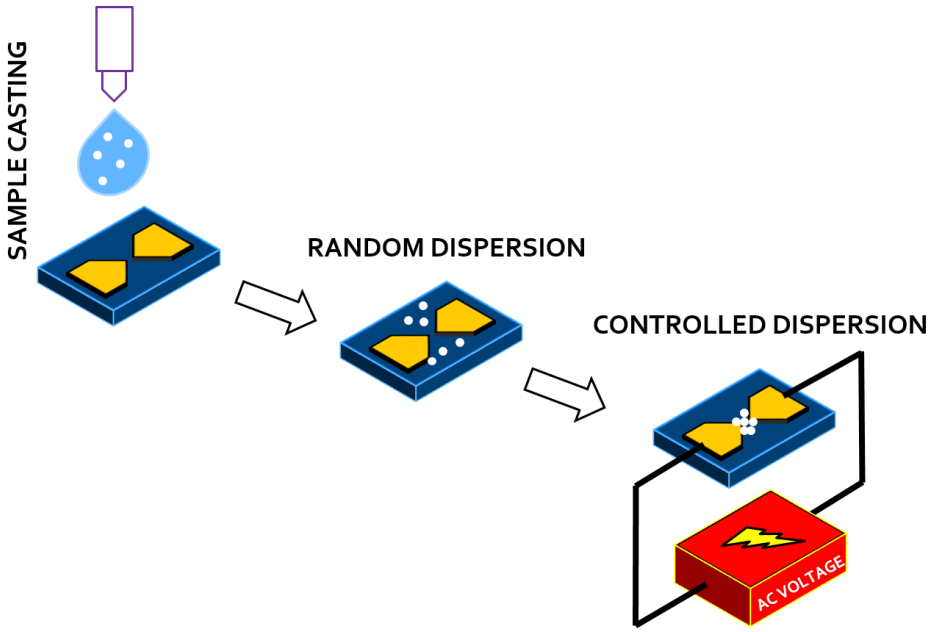

Figure 2. 9 Schematic illustration of particles trapping by DEP method

2.8.3.3. Electrical characteristics

The electrical characteristic of samples were investigated by tailor-made probing system, equipped with cryogenic freezer, to conduct an *I-V* measurement at low temperature. The photograph of the machine is displayed in Figure 2.10. The current-voltage data were recorded using Keysight Agilent 4156 A semiconductor parameter analyzer, as a function of voltage as well as *I-V* at various temperature, ranging from 15 to 300 K. All measurement were performed in vacuum condition.

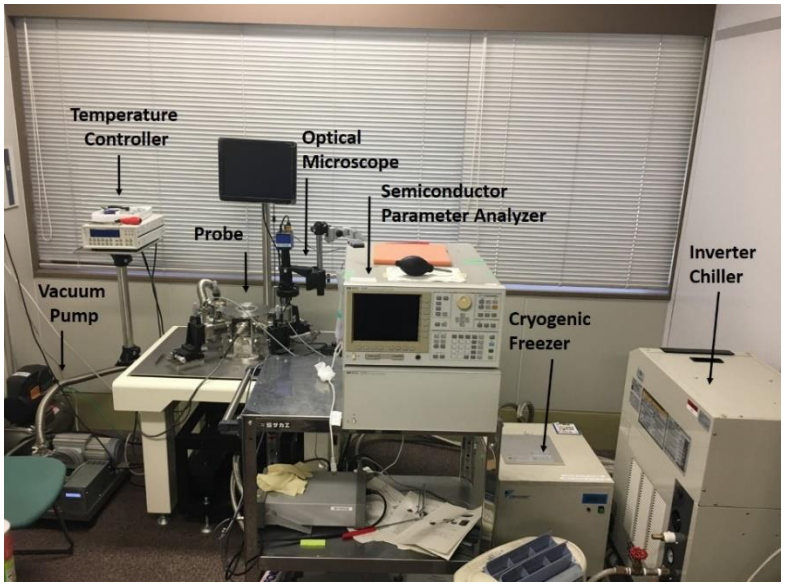

Figure 2. 10 Photograph of probing system equipped with cryogenic freezer

2.8.4. Magnetic property measurement

2.8.4.1. SQUID magnetometer

The magnetic property were measured only to LCO samples by Superconducting Quantum Interference Device (SQUID) magnetometer Quantum Design MPMS XL Model M 107-3 TKIR. SQUID is known as the most sensitive instrument to sense the magnetic property which has demonstrated field resolution at the 10^{-17} T level.[2)] The working principle of a SQUID magnetometer is based on flux quantization within a superconducting loop due to Josephson junctions.[3)] SQUID magnetometer consists of two superconductor materials separated by thin insulating layers to experience two parallel Josephson junctions, as illustrated in Figure 2.11.

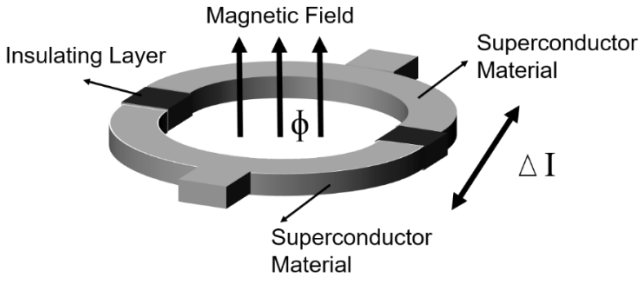

Figure 2. 11 Josephson junction principle

In the DC Josephson effect, the electrical current density through a weak electric contact between the two superconductors depends on the phase difference ($\Delta\varphi$) of the two superconducting wave functions, which influenced upon the change in magnetic flux. Therefore such structure results on a current proportional to the phase difference of the wave function can flow in the junction, in the absence of the voltage. Therefore, such a structure can be used to convert magnetic flux into an electrical voltage. If a constant biasing current is maintained in the SQUID magnetometer, the measured voltage oscillates with the changes in phase at the two junction. Counting the oscillations allows the magnetic flux change to be evaluated.

In sample preparation, all used tools must be non-metal based, because SQUID is very sensitive machine, even small amount of metal will influence the magnetic measurement. There are two main items used for preparing the sample, there are a capsule and clear plastic straw. Firstly, the weight of sample was recorded because the magnetization result need to be normalized [i.e. mass magnetization (emu/g)]. Secondly, place the sample in a capsule (approximately half of capsule at the bottom part) and a wad of cotton can be placed at the top part of capsule to hold the sample orientation. Thirdly, poke a small hole in the top of the capsule to allow air to be pumped out. Next, the capsule was put in the middle of a plastic straw. The capsule then placed properly at the center of a plastic straw, otherwise it will move during the measurement.

There are two types of magnetic measurements: (1) *M-H* and (2) *M-T* sequences. *M-H* is a measurement of magnetization (M) as a function of applied magnetic field (H). In this measurement, the temperature is fixed at certain temperature and M is recorded as a series of applied magnetic field (H) values. *M-T* is a measurement of magnetization as a function of temperature (T). In this measurement, two measurement were done: 1) the applied magnetic field is fixed at certain value and M is recorded as a series of temperature, from 6 K to 300 K, 2) the temperature is fixed and H is applied ranging from -50,000 Oe to 50,000 Oe.

2.8.4.2. Muon spin rotation

Muon spin rotation (μSR) is an advance technique to investigate magnetic properties in microscopic view. In μSR technique, polarized muons are embedded into a sample, therefore the polarization promotes in the local magnetic field, until they decay. Since muon has positive charge, it located at an interstitial site and parity violation interaction decay occurs. Muon decays to positron and two neutrinos. The decay positrons are collected by detector and time dependence of the muon spin depolarization function can be recorded, which reflect the distribution of magnetic fields at the muon site.

In this research work, zero field (ZF-μSR) were perfomed in Japan Proton Accelerator Research Complex (J-PARC) installed at the RIKEN-RAL Muon Facility. The μSR time spectra are interpreted by asymmetry parameter [A(t)], which obtained from the ratio of numbers of positron detected by the forward [F(t)] and backward [B(t)] counters at t time: $[A(t) = (F(t) - \alpha B(t)]/[F(t) + \alpha B(t)]$, and all time spectra are corrected by calibration factor α during analysis. The μSR time spectra was fitted by Eq. 1:

$$A(t) = A_1 \cos\left(\gamma_\mu H_{int} t + \phi\right) e^{-\lambda_1 t} + A_2 e^{-\lambda_2 t} \quad \text{..... (2.3)}$$

First and second terms correspond the muon-spin precession component and fast depolarizing component, respectively, with A_1 and A_2 are the initial asymmetries of each component.

2.8.5. Thermal analysis

Thermogravimetry Analysis (TGA) is a thermal analysis technique that measure the mass change of a sample with temperature.[1)] The application of this TGA technique is to analyze decomposition of material and thermal stability through mass change as a function of temperature or time in a controlled atmosphere. Here, TG-DTA Rigaku Model TG8120 (see Figure 2.12) was used to estimate the oxygen content based on the change of weight of the sample. The oxygen content was estimated for LCO_{4-y} sample, since the sample was subjected

for electron doping by post-annealing at 450 ℃ for 24 h under non-oxygen atmosphere. The change of oxygen content were calculated by equation 2.2.[4)]

$$\Delta\delta = \frac{M_S}{M_O}\frac{\Delta w_S}{ws} \quad \text{..... (2.4)}$$

where Δδ, Ms, Mo, ws are the change of oxygen content, molecular weight of the sample and oxygen and the weight of sample, respectively.

Figure 2. 12 Photograph of TG-DTA machine

2.9. References

1) Y. Leng, Materials characterization: introduction to microscopic and spectroscopic methods (John Wiley & Sons, Singapore, 2009).

2) R. Fagaly, Rev. Sci. Instrum. 77, 101101 (2006).

3) B.D. Josephson, Phys. Lett. 1, 251 (1962).

4) T. Nakamura, Y. Ling, & K. Amezawa, J Mater. Chem. 3, 10471-10479 (2015).

CHAPTER 3

Size Controlled Synthesis of La_2CuO_4 and $SrTiO_3$ Nanoparticles by Sol-Gel Technique

3.1. Abstract

The formation of lanthanum cuprate (La_2CuO_4/LCO) and strontium titanate ($SrTiO_3$/STO) nanoparticles (NPs) was systematically studied via sol-gel method. Parameter studied in the fabrication process including acid catalyst, pH and annealing condition was assessed. The results obtained by field emission scanning electron microscopy and X-ray diffraction method show that the required minimum annealing condition to fabricate pure LCO NPs and STO NPs was at 600 ℃ for 45 min and 500 ℃ for 5 h, respectively. The size of the product could be successfully controlled from nanoscale to bulk one by varying the annealing condition during synthesis, also affected by the pH of the solution.

3.2. Introduction

Investigation of nanoscale materials has been a subject of interest of researchers over the past years owing their unique properties compared with their encounter bulk.[1)] One of the most fascinating materials is perovskite oxide.[2)] In a typical perovskite material, its structural symmetricity can be reduced owing lattice distortion, providing great variability in the electrical and magnetic properties.[3)] Tuning the electric properties is also reliable depends on charge carriers and materials itself.[4)] The flexibility properties might increase the performance of a material both in magnetic and electronic devices and fulfil the technology demant.

Free-standing NPs of strontium titanate ($SrTiO_3$/STO) and lanthanum copper oxide (La_2CuO_4/LCO) are studied. STO has indirect and direct band gaps of 3.25 and 3.75 eV, respectively.[5)] High-dielectric-constant of STO makes the material good to be utilized in capacitors[6)] and transistors.[7)] Since STO is also widely used as an excellent substrate for epitaxial growth of various oxides,[8-10)] physics of

complex oxide heterostructures based on STO also expected.[11-13] Moreover, LCO is basically a frontier of strong correlated antiferromagnetic (AF) Mott insulator[14] with Néel temperature (T_N) at about ~ 300 K[15]. Apart from starting system of superconductivity, as an AF material, LCO is also potentially to be utilized in magnetic devices. Earlier, Néel stated that AF material might have limited practical applications.[16] For the time being, enormous application of AF material as spin-transfer torque[17] and magnetoresistance[18] recently revealed and strongly turns the perspective of AF material these days,[19] and may another potential applications of AF material will appear in near future. To date, there are no detail information about free-standing of LCO and STO NPs fabrication. Conversely, the fabrication of nano-sized LCO and STO material is essentially fundamental for future wide applications.

In the present work, fabrication of free-standing LCO and STO NPs by sol-gel method were investigated. Various process were implemented in perovskite synthesis such as sol-gel,[20] solid-state, hydrothermal,[21] spray pyrolysis,[22] co-precipitation,[23] Among them, here sol-gel method was selected considering the particles of the products are high in homogeneity, purity, and size is easy to be controlled.[24] Accordingly, sol-gel is preferable to make multi component compound with controlled stoichiometry. Some parameters such as acid catalyst, pH, annealing condition were assessed in the fabrication process. According to the results, the size of the product could be controlled from nanoscale to bulk size order.

3.3. Experimental procedure

Sol-gel was implemented to fabricate LCO and STO NPs and some parameters used is summarized in Table 3.1. A stoichiometric amount of starting materials were dissolved in an appropriate amount of acid catalyst separately, to attain its nitrate/citrate forms. The organic matters used were citric acid (CA) (Wako, 99.5%) and ethylene glycol (EG) (Wako, 99%) with mass ratio 3:2 and the pH of the solution was adjusted to 7 by NH_3 (aq) (Wako, 38%). The liquid phase in the gel was dried by heating at 150 ℃ for 1 h, and appearance of an

elastic solid gel formed. For LCO, heat treatment was done in two stages: 1) 300 ℃ for 3 h and 2) 500-800 ℃ for 0-3 h for LCO, where the STO only at 400-800 ℃. The final product was ground for about 1 h using agate mortar until obtaining well-homogeneous fine powder.

Table 3. 1 Parameter used for LCO and STO synthesis

Parameter	**La_2CuO_4**	**$SrTiO_3$**
Starting Material 1	La_2O_3 (Wako, 99.9%)	$SrCO_3$ (Aldrich, 99.9%)
Starting Material 2	CuO (Wako, 99.9%)	$C_{12}H_{28}O_4Ti$ (Tokyo Chemical Industry
Acid Catalyst	Nitric Acid (Wako, 70%)	Citric Acid (Wako, 99.5%)

The phase of LCO samples were examined by x-ray diffractometry (XRD, Rigaku RINT-2100) with Cu Kα radiation 40 kV (λ = 0.154 nm) and the scanning rate was 0.02 °/s. The morphology of samples were observed by field emission scanning electron microscopy (FESEM, Hitachi S-5200), with acceleration voltage at 5 kV. The average particle size were calculated by measuring the diameter of particles from SEM image, from one edge to the other opposite edge of particle, using Image J software. Additionally, crystallite size were also calculated by Scherrer formula (Equation 3.1)

$$D = \frac{k\lambda}{\beta cos\theta} \quad (3.1)$$

where D is the crystallite size, k is the Scherrer constant (0.9), λ is the wavelength of Cu Kα, and β is the full-width at half maximum (FWHM) of the main XRD peak.

3.4. Results and discussion

3.4.1. Results of LCO synthesis

Figure 3.1 shows the XRD profiles of the fabricated LCO samples at different annealing condition, at pH 7. The LCO phase in XRD profiles was matched with reference of JCPDS no. 38-0704. Annealing temperature study was firstly conducted by annealing the samples at 800 ℃ [Figure 3.1 (a)], 700 ℃ [Figure 3.1 (b)], 600 ℃ and 500 ℃ [Figure 3.1 (c)] for 180 min. As seen LCO phase with orthorhombic structure began to form if the sample was annealed at 600 ℃ and above. Sharp peaks in XRD profiles indicate that the samples is highly crystalline. Annealing the sample at 500 ℃ resulted on mixture phases of starting materials and insufficient to produce LCO phase [Figure 3.1 (g)]. Next step, several samples were prepared by annealing the sample at 600 ℃, but the annealing time was varied from 180 min [Figure 3.1 (c)], 90 min [Figure 3.1 (d)], 45 min [Figure 1 (e)] and 0 min [Figure 1 (f)]. According to the XRD results, the required annealing condition for the formation of LCO was at 600 ℃ for 45 min at least. Additionally, the lattice parameters of LCO with the orthorhombic structure were calculated from Equation 3.2:

$$\frac{1}{d^2} = \frac{h^2}{a^2} + \frac{k^2}{b^2} + \frac{l^2}{c^2} \quad \text{.....(3.2)}$$

Where a, b, c are the lattice constant and d is the inter-atomic spacing. The lattice parameters and unit cell volume are summarized in Table 3.2.

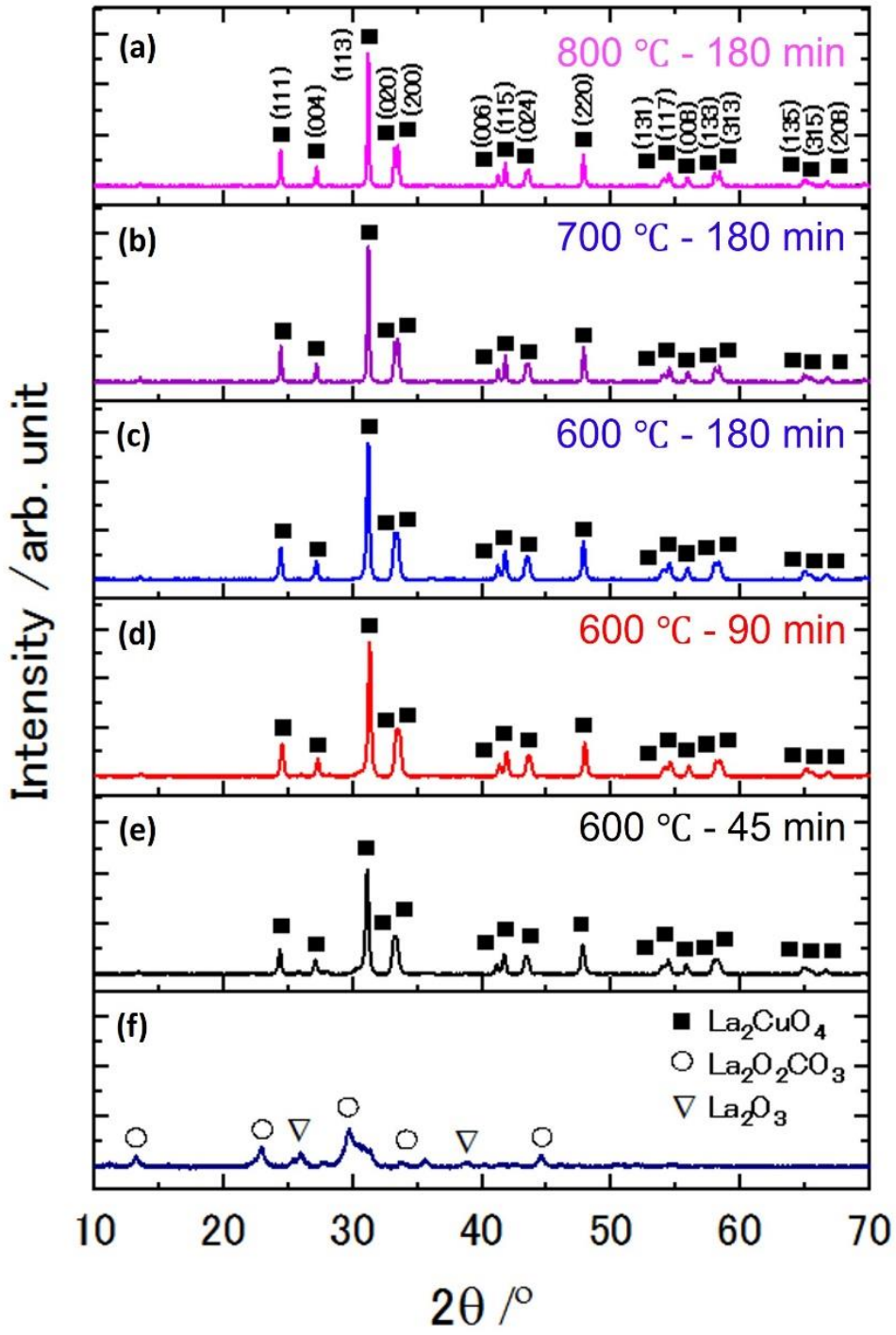

Figure 3. 1 XRD profiles of the synthesized LCO at: (a) 800 ℃ – 180 min, (b) 700 ℃ – 180 min, (c) 600 ℃ – 180 min, (d) 600 ℃ – 90 min, (e) 600 ℃ – 45 min, (f) 600 ℃ – 0 min

Figure 3.2 displays FESEM image of the synthesized LCO annealed at various temperature and time. The morphology for all samples is sphere-like structure and the particle size is varied depending on the annealing condition.

The morphology of LCO samples annealed at 600 ℃ for 45 min, 90 min and 180 min is shown in Figure 3.2 (a), (b) and (c), respectively, representing the effect of annealing time during synthesis. The obtained average particle size of those samples were noted to be 69 nm, 73 nm, and 96 nm, respectively. Annealing temperature effect is represented by LCO samples annealed at 600 ℃, 700 ℃ and 800 ℃ for 180 min, as shown in Figure 3.2 (c), (d) and (e), respectively. The measured particles size were noted to be about 96, 153 and 286 nm. The tendency of particle size was found increases with rising annealing temperature of synthesis. The summary of obtained particle size (based on FESEM images) and crystallite size (based on XRD results) against annealing condition is summarized in Figure 3.3. The tendency of crystallite size increases with annealing synthesis condition and ranging from ~ 35-52 nm, and the result is in agreement with FESEM results. Lower temperature and short time of annealing produces smaller particle and crystallite size. In our work, LCO NPs (size < 100 nm) could be fabricated when the annealing temperature was 600 ℃. Additionally, lattice parameter of the synthesized LCO is shown in Figure 3.2. The increase of a/c lattice and expansion in unit cell volume appear when the size of LCO is reduced and remarkably says the LCO exhibiting lattice distortion.

Table 3. 2 Lattice parameter of the synthesized LCO

Particle size (nm)	**a (Å)**	**b (Å)**	**c (Å)**	**a/c**	**V (Å^3)**
69	5.36274	5.40764	13.16964	0.40720	381.91649
96	5.3489	5.39902	13.12588	0.40750	379.05990
153	5.3507	5.3977	13.10634	0.40825	378.53041
286	5.35224	5.4	13.10756	0.40833	378.83595

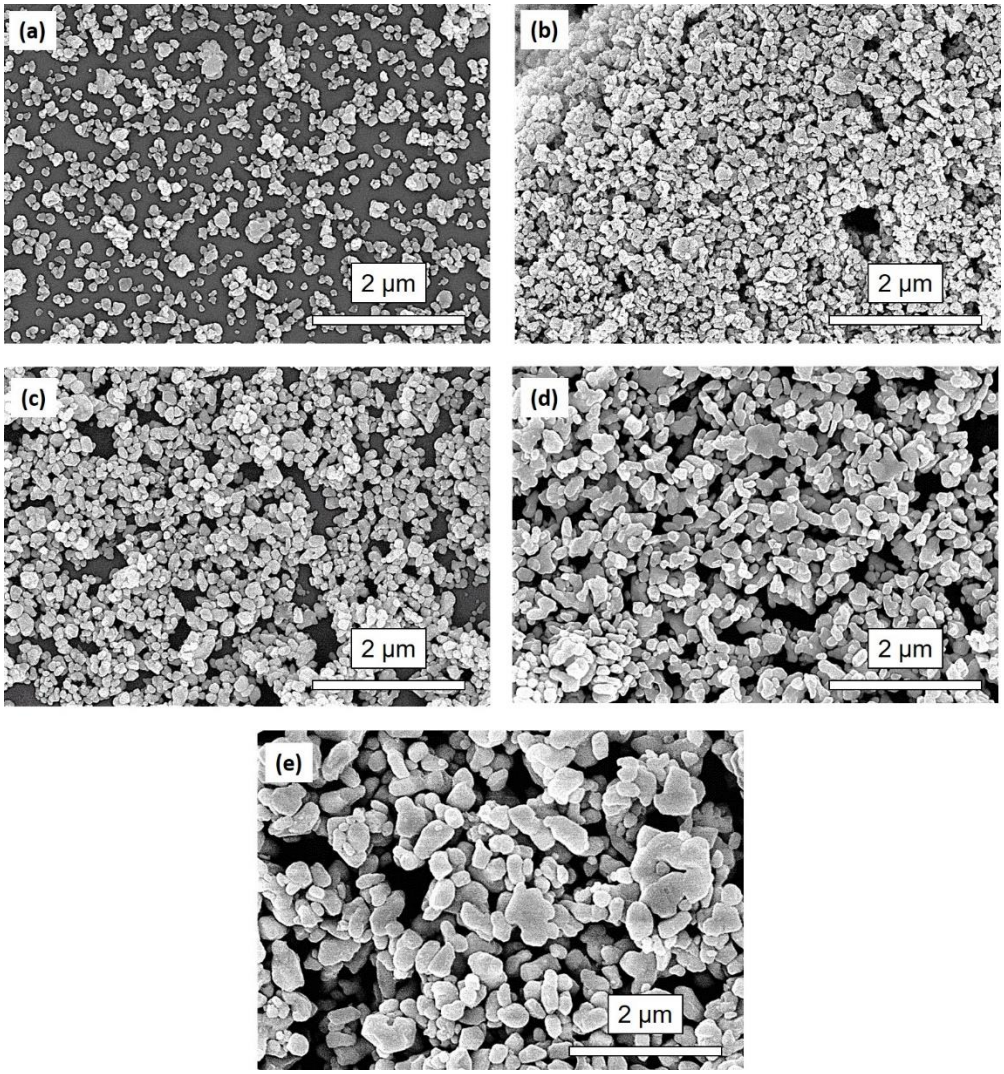

Figure 3. 2 FESEM images of the synthesized LCO annealed at (a) 600 ℃ - 45 min, (b) 600 ℃ - 90 min, (c) 600 ℃ - 180 min, (d) 700 ℃ - 180 min and (e) 800 ℃ - 180 min

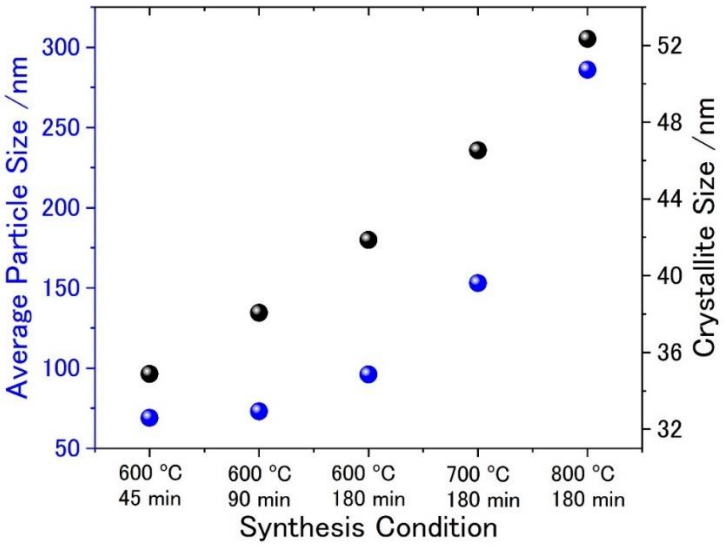

Figure 3. 3 Summary of average particle size (based on FESEM images) and crystallite size (based on XRD peaks) obtained of the synthesized LCO.

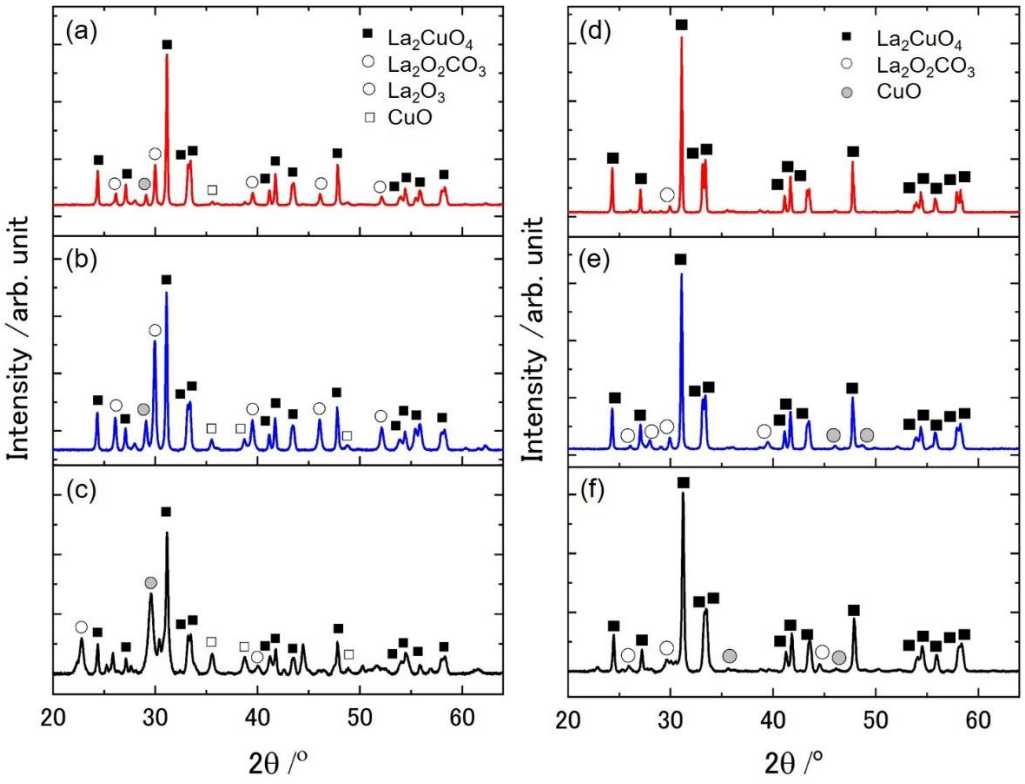

Figure 3. 4 XRD profiles of LCO samples synthesized at: (a) 600 ℃ pH 2, (b) (a) 700 ℃ pH 2, (c) 800 ℃ pH 2, (d) 600 ℃ pH 10, (e) 700 ℃ pH 10 and (f) 800 ℃ pH 10.

Additionally, the effect of pH on LCO synthesis was also assessed and the XRD profiles of LCO synthesized at pH 2 and 10 is shown in Figure 3.4. By using pH 2, mixture phases of LCO and others $La_2O_2CO_3$, La_2O_3 and CuO are exist if the sample was annealed at 600 [Figure 3.4 (c)], 700 [Figure 3.4 (b)] and 800 ℃ [Figure 3.4 (a)], and the intensity of mixture phases decreases with increasing of annealing synthesis temperature and might need higher temperature to obtain pure LCO phase. However, lower annealing temperature is preferable to get small size of LCO. Also, by using pH 10, LCO phase present for samples annealed 600, 700 and 800 ℃, but still not show single phase of LCO. In this research work, pH 7 is still considered as the optimum condition to synthesize LCO NPs.

XPS analysis was also performed for LCO NPs with 69 nm size, in order to know the element exist in the sample, as well as its oxidation state. Figure 3.5 displays the XPS analysis of the synthesized LCO. As seen La, Cu and O element are observed in the sample. Figure 3.5 (a) shows La 3d spectrum, consisted of multiplet split of La $3d_{3/2}$ (850 eV and 853.3 eV) and La $3d_{5/2}$ (833.4 eV and 836.8 eV) that matched with oxidation state of La^{3+}. The Cu 2p spectrum in Fig. 3.5 (b) indicates Cu $2p_{1/2}$ and Cu $2p_{3/2}$ exist in the sample, with strong Cu^{2+} satellite are observed at 960.9 eV and 942.6 eV, which referred to oxidation state of Cu^{2+}. Moreover, the O 1s peak [Figure 3.5 (c)] with binding energy at 530 eV is referred to oxidation state of O^{2-}. Therefore, the oxidation state of La, Cu and O is 3+, 2+ and O2-, respectively and agreed with chemical formula La_2CuO_4.

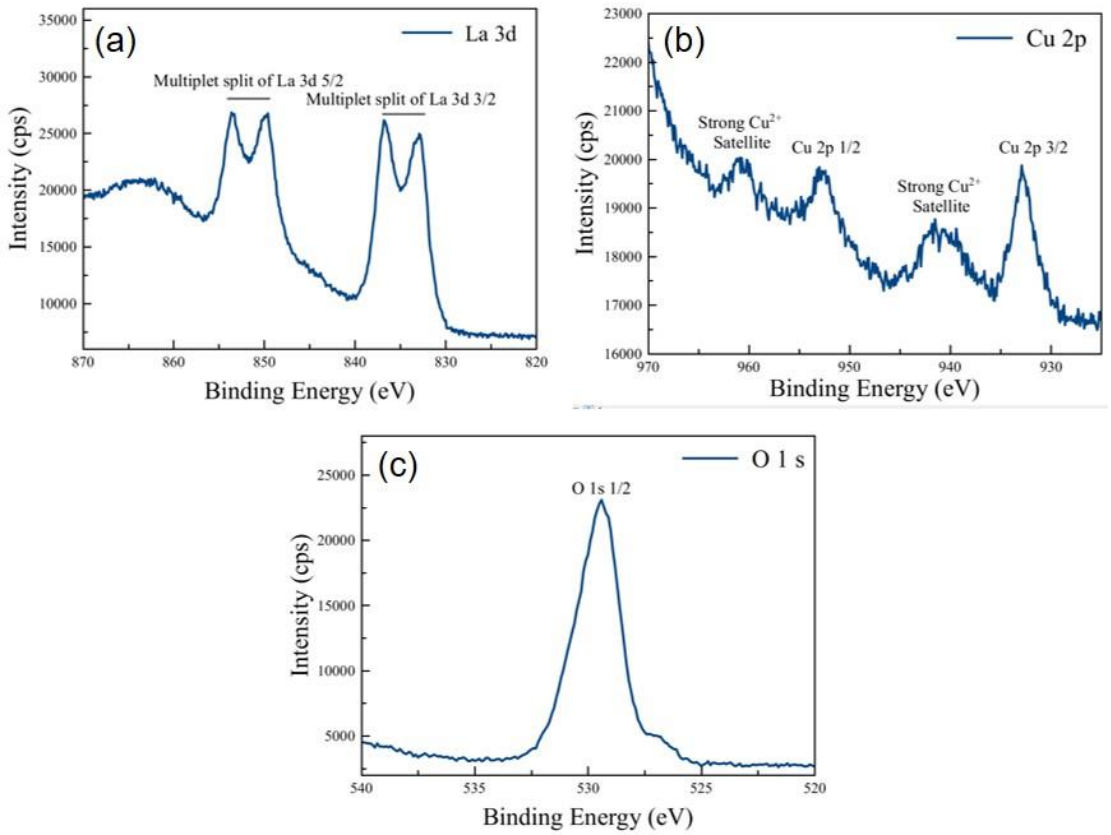

Figure 3. 5 XPS spectra of LCO NPs with 69 nm size: (a) La 3d, (b) Cu 2p and (c) O 1 s spectrum.

3.4.2. Results of STO synthesis

XRD profiles of the synthesized STO NPs are displayed in Figure 3.6. The XRD profile for sample annealed at 400 ℃ shows the temperature was insufficient to yield STO phase, instead resulted on amorphous (see broadening peak in the XRD profile) and $SrCO_3$ phase, marked by white triangles symbol. By increasing the annealing temperature to 500 ℃, high crystalline STO phase with cubic structure start forming. The STO phase also present in the sample annealed at 600, 700 and 800 ℃, in agreement with JCPDS No. 86-0178. The average crystallite size and lattice parameter analysis is shown in Table 3.3. As seen, the CS tends to increase by raising the temperature of synthesis. The lattice parameters of LCO with the orthorhombic structure were calculated from Equation 3.3:

$$\frac{1}{d^2} = \frac{h^2+k^2+l^2}{a^2} \quad \text{(3.3)}$$

Table 3. 3 Lattice parameter of the synthesized STO

Synthesis temperature	a (Å)	V (Å^3)	Average Crystallite Size (nm)
500 ℃	3.9253	60.4809	24.6
600 ℃	3.9158	60.0428	17.0
700 ℃	3.9159	60.0474	30.4
800 ℃	3.9182	60.1533	34.8

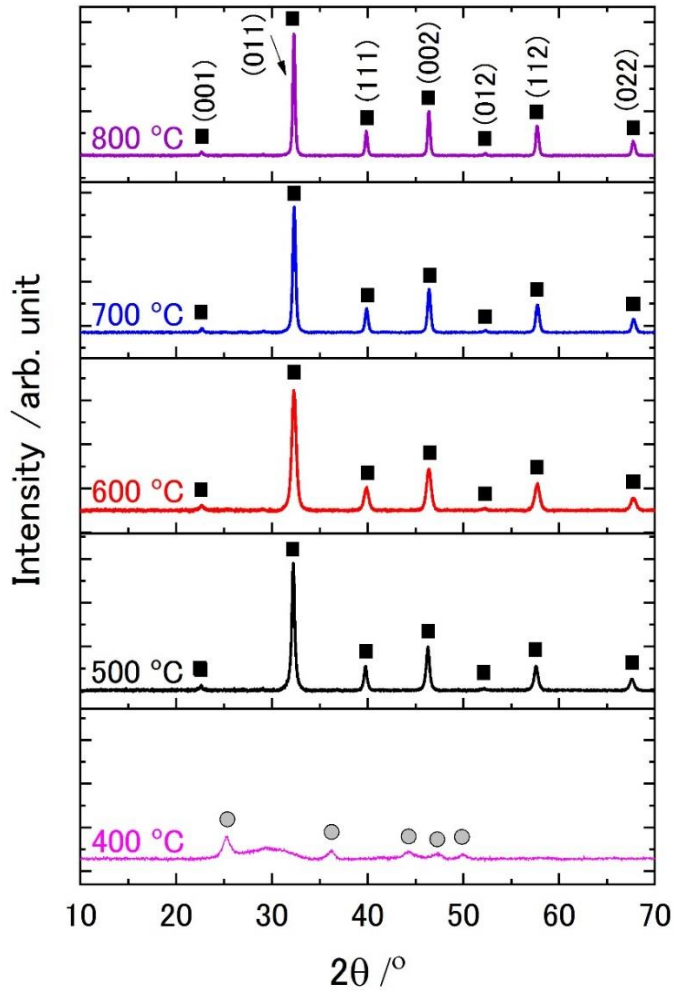

Figure 3. 6 XRD profiles of pure STO synthesized at 400–800 °C for 5 h

Figure 3.7 shows the FESEM images of the synthesized of STO at 500-800 ℃. The STO NPs has a sphere-like structure and aggregated with average particle size 21.4 nm, 17.2, 30.1 nm and 42.3 for samples annealed at 500 ℃ [Figure 3.7. (a)], 600 ℃ [Figure 3.7 (b)], 700 ℃ [Figure 3.7 (c)], and 800 ℃ [Figure 3.7 (d)], respectively. The particle size of the product is in proportional with synthesis temperature.

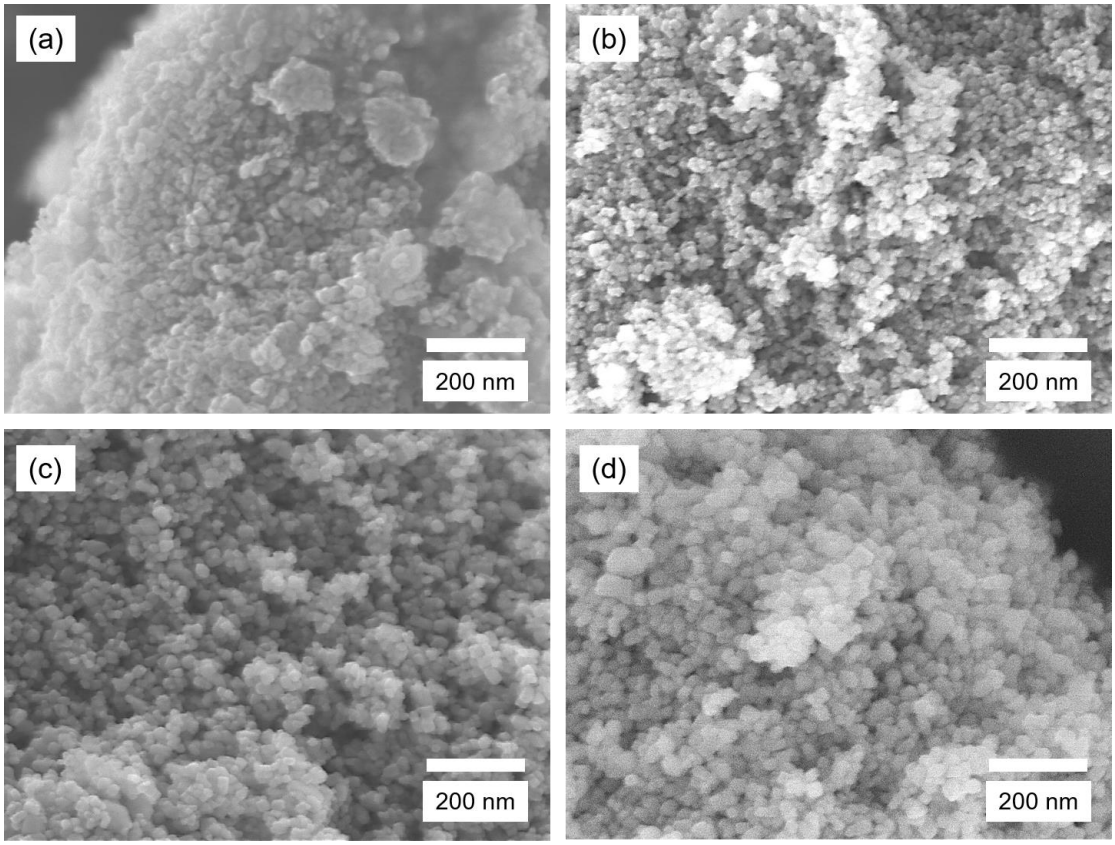

Figure 3. 7 FESEM images of STO NPs annealed at: (a) 500, (b) 600, (c) 700 and (d) 800 °C for 5 h.

3.4.3. Discussion

The mechanism of LCO and STO formation in this work started from the reaction of the raw materials with the acid catalyst, either nitric or citric acid, to induce more hydrolysis process and yield its metal nitrate or citrate form. As the metal nitrate/citrate precursors were mixing together, the ethylene glycol (EG) and citric acid (CA) were added. The metal nitrate/citrate acts as the oxidant,

where the EG and CA as organic fuel. By adding the organic fuel, the precursors undergo further hydrolysis and polycondensations, thus forming metal chelate complex, to tighten the bonding between one metal to another metal ions. The presence of organic matters in here is also important for suppression of the crystal growth to obtain small crystallite size and preventing precipitation of individual oxide.[24] In the case of LCO synthesis, pH 7 is the optimum pH to synthesize LCO. NH_3 (aq) was used as pH adjustment and acting as organic fuel as well, remembering nitrate based material was used. The NH_3 (aq) will supply N and H to the system and enhancing the combustion process,[25] helping on the releasing gas product such NO_x, CO_x and H_2O. As for STO synthesis, since it is metal citrate based synthesis, so the precursors contains metal ions and organic matter (C, H and O). Heat treatment is sufficient enough to release the organic matters (residue) from the precursors, as CO_2 and H_2O. Heating process was performed several times in the synthesis. Firstly, the precursor was heated at 150 °C prior to water evaporation, to remove all the liquid phase and solid gel formed. Secondly, further annealing at 300 °C for 3 h was applied to decompose all the organic matters. During this stage, volume expansion of sample was physically observed (Notes that second annealing only done for LCO synthesis). Finally, annealing at high temperature (i.e. 500-800 °C) was performed prior to crystallization process. As heat energy is induced to the system, the nucleation of particle start to occur and the particle growth and forming extended particle network. The agglomeration of particle was reduced by grinding the sample agate mortar.

The particle size obtained was found to be proportional with the synthesis temperature. The growth of particle is driven by thermal energy,[26] which serves diffusion of atom. Increasing the annealing temperature provides more thermal energy and serve faster migration of boundaries, thus migration of atom through diffusion process develops from one size of the boundary to the neighborhood atom, leading to the reduction of boundary area. As a result, growth of the particle sizes take places and the total boundary area will decrease. With rising annealing temperature and time of synthesis, the growth of particles more

intensively occur, boundary area will be reduced and bigger particle size will be obtained. In the case of STO, annealing time study was not studied since the increment of annealing temperature of 100 ℃ resulted only changed the size about 10 nm. As why the STO sample annealed at 600 ℃ is smaller compared to the 500 ℃ sample, one possibly reason is due to to non-uniform heating, therefore affecting the gas products and the growth of the material.[27)]

3.5. Conclusions

The synthesis of LCO and STO NPs were investigated by sol-gel method. Metal nitrate and citrate based were assessed on the formation of LCO and STO NPs, respectively. For nitrate based synthesis, the addition of ammonia as pH adjustment is required to induce LCO phase at lower temperature, since it supply N and H to the system an d assist the formation during heating. Additionally, for metal citrate based synthesis, no pH adjustment was required since only C, H and O and metal ion in the precursors, and the organics could be removed by only heating. The requirement minimum annealing condition to obtain LCO and STO phase was at 600 ℃ for 45 min (69 nm size) and 500 ℃ for 5 h (21 nm size), respectively. The particle size of LCO could be controlled by varying the annealing condition during synthesis. Higher annealing temperature and longer time result on bigger particle. Heat energy provides the particle growth more intensively.

3.6. References

1) D. L. Schodek, P. Ferreira, and M. F. Ashby, Nanomaterials, Nanotechnologies and Design: An Introduction for Engineers and Architects (Butterworth-Heinemann, Oxford, U.K., 2009).
2) L.G. Tejuca and J. Fierro, Properties and Applications of Perovskite-Type Oxides (CRC Press, Boca Raton, FL, 2000).
3) H. Wu and X. Zhu, Perovskite Materials-Synthesis, Characterisation, Properties, and Applications (InTech, Rijeka, 2016).
4) K. Szot, W. Speier, G. Bihlmayer, and R. Waser, Nat. Mater. 5, 312 (2006).

5) K. Van Benthem, C. Elsässer, and R. French, J. Appl. Phys. 90, 6156 (2001).
6) W. Gao, M. Yao, and X. Yao, Ceram. Int. 43, 13069 (2017).
7) Y. Sato, K. Doi, Y. Katayama, and K. Ueno, Jpn. J. Appl. Phys. 56, 051101 (2017).
8) S. Nakashima, S. Seto, Y. Kurokawa, H. Fujisawa, and M. Shimizu, Jpn. J. Appl. Phys. 56, 10PF17 (2017).
9) S. Okamoto, S. Okamoto, S. Yokoyama, K. Akiyama, and H. Funakubo, Jpn. J. Appl. Phys. 55, 10TA08 (2016).
10) C. Zhao, C. Zhou, and C. Chen, Physica B 521, 376 (2017).
11) A. Monteiro, D. Groenendijk, N. Manca, E. Mulazimoglu, S. Goswami, Y. Blanter, L. Vandersypen, and A. Caviglia, Nano Lett. 17, 715 (2017).
12) Z. Liu, L. Sun, Z. Huang, C. Li, S. Zeng, K. Han, W. Lü, T. Venkatesan, and Ariando, J. Appl. Phys. 115, 054303 (2014).
13) S. Gariglio, M. Gabay, and J. -M. Triscone, APL Mater. 4, 060701 (2016).
14) F. Zhou, Growth and Characterization of Bulk Superconductor Material (Springer, Switzerland, 2016)
15) V.G. Storchak, J.H. Brewer, D.G. Eshchenko, P.W. Mengyan, O.E. Parfenov, A.M. Tokmachev and P. Dosanjh, Phys. Rev. B 94, 134407 (2016).
16) L. Néel, Sci. 174, 985 (1971).
17) S. Fukami, C. Zhang, S. DuttaGupta, A. Kurenkov and H. Ohno, Nat. Mater. 15, 535 (2016).
18) Z. Qiu, D. Hou, J. Barker, K. Yamamoto, O. Gomonay and E. Saitoh, Nat. Mater. 1 (2018).
19) M.B. Jungfleisch, W. Zhang and A. Hoffmann, Phys. Lett. A. 382, 865 (2018).
20) A. Youssef, H. Farag, A. El-Kheshen, and F. Hammad, Silicon 1, 1 (2017).
21) V. Kalyani, B. S. Vasile, A. Ianculescu, A. Testino, A. Carino, M. T. Buscaglia, V. Buscaglia, and P. Nanni, Cryst. Growth Des. 15, 5712 (2015).
22) S. -J. Shih and W. -L. Tzeng, Powder Technol. 264, 291 (2014).
23) Y. -H. Chen and Y. -D. Chen, J. Hazardous Mater. 185, 168 (2011).

24) A. Danks, S. Hall, and Z. Schnepp, Mater. Horizons 3, 91 (2016).
25) M. Epifani, E. Melissano, G. Pace and M. Schioppa, J Eur. Ceram. Soc. 27, 115 (2007).
26) F. Humphreys and M. Hatherly: Humphreys FJ, Hatherly M, Recrystallization and Related Annealing Phenomena (Oxford, Pergamon, 1995).
27) X. Sun, Y. Shi, P. Zhang, C. Zheng, X. Zheng, F. Zhang, Y. Zhang, N. Guan, D. Zhao, and G. D. Stucky, J. Am. Chem. Soc. 133, 14542 (2011).

CHAPTER 4

Size Dependent Magnetic Properties of La_2CuO_4 Nanoparticles Synthesized by Sol-Gel Method

4.1. Abstract

The effect of particle size on the magnetic properties lanthanum cuprate (La_2CuO_4/LCO) nanoparticles (NPs) was systematically studied. The particle size of LCO used to be investigated are: 69 nm, 96 nm, 153 nm and 286 nm. Magnetic property measurement by SQUID magnetometer reveals that the enhancement of magnetization occurs as the particle size is reduced. Additionally, advance magnetism of LCO was also investigated by muon spin rotation (μSR) and the results showed Néel temperature reduction was observed with reducing size.

4.2. Introduction

Investigation of magnetism in nano-sized particles has been a subject of interest over the past years owing their properties are deviated comparing to their bulk.[1)] A perovskite oxide material is one of the best material to be investigated since the material potentially to appear extraordinary variety of properties.[2)] La_2CuO_4 (LCO) is the selected material studied here. LCO is basically a frontier of strong correlated antiferromagnetic (AF) Mott insulator[3)] with Néel temperature (T_N) of about ~ 300 K[4)]. The strong electron-electron interaction in the sample making the sample to exhibit superconductivity, by introducing some charge carriers to the sample. Therefore, here also remain understanding on how the magnetism changed in nano-sized of such strong correlated system. To date, there are still no detail information about magnetism in nano-sized LCO.

Our experiments were designed to investigate on how nano-sized affect the magnetic properties of LCO utilizing high sensitive muon-spin rotation (μSR) and SQUID magnetometer. Magnetism in LCO was found to be strongly affected

by size: a reduction of T_N enhancement of magnetic moment with reducing size. A detailed magnetic phenomena study on the Mott insulating system nano-sized LCO became significantly importance, since the properties will also be related to others strong correlated materials.

4.3. Experimental procedure

The magnetic property of LCO was measured using Quantum Design MPMS SQUID magnetometer. The samples were placed to a capsule and inserted into the magnetometer. The samples were cooled to a desired temperature followed by measuring the magnetic response of sample in a fixed temperature *M-H* and magnetic field *M-T*. The *M-T* measurement was done from 5 to 300 K under magnetic field 0.5 T. The *M-H* measurement was also performed with applied field ranging from -5 to 5 T (double sweep) at 5 K with increment 0.5 T.

Zero field (ZF-μSR) were perfomed in Japan Proton Accelerator Research Complex (J-PARC) installed at the RIKEN-RAL Muon Facility. Muon is generated by high proton beam and implanted to the sample. Muon has spin S = ½ and lifetime 2.2 μs before it decays, thus by implanting muon to the sample, it will act as local probe and the magnetism of sample in microscopic view can be observed. The emitted positron from muon decays then counted by forward and backward detector, located along the muon beam for further processing information. Muon spin polarization is interpreted by asymmetry parameter [A(t)], which obtained from the ratio of numbers of muon detected by the forward [F(t)] and backward [B(t)] counters at t time: $[A(t) = (F(t) – \alpha B(t)]/[F(t) + \alpha B(t)]$, and all time spectra are corrected by calibration factor α during analysis.

4.4. Results and discussion

The morphology of the synthesized LCO with various particle size is displayed in Figure 4.1. The synthesis process were explained in Chapter 3 in this thesis. The sample used were noted having average particle size of about 69 nm [Figure 4.1 (a)], 96 nm [Figure 4.1 (b)], 153 nm [Figure 1 (c)] and 286 nm [Figure 1 (d)].

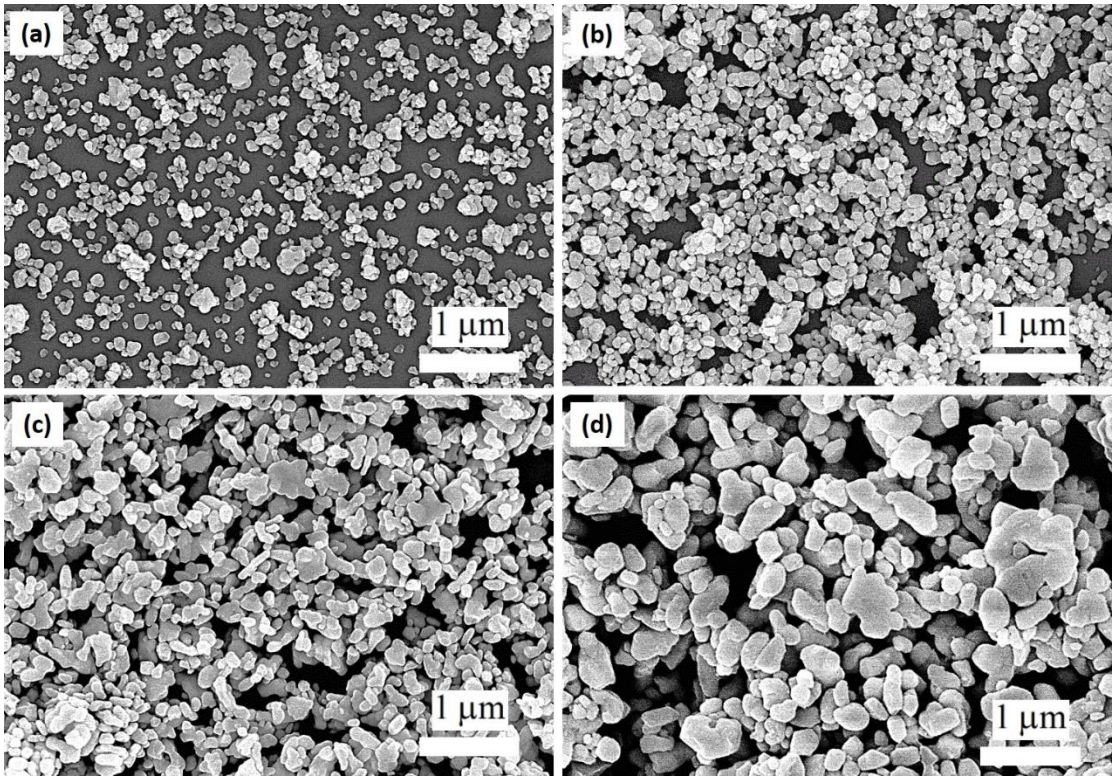

Figure 4. 1 FESEM images of synthesized LCO samples with particle size: (a) 69 nm, (b) 96 nm, (c) 153 nm and (d) 286 nm

We systematically studied the magnetism of LCO from bulk to nanoscale through varying the particle size. The LCO magnetization response as a function of magnetic field have been recorded by SQUID magnetometer at 6 K from -5 T to 5 T, as shown in Figure 4.2 (a). The tendency of magnetization for all samples rises linearly as the magnetic field is stronger and enhanced with reducing size. The magnetization of samples at 5 T was recorded reaching 1.07 emu/g, 0.97 emu/g, 0.25 emu/g and 0.17 emu/g for sample with 69 nm, 96 nm, 153 nm and 286 nm size, respectively, thus the obtained magnetization is inversely proportional with size. From *M-H* curve, the magnetization of sample is strongly size dependence.

To double confirm the finding, temperature dependent magnetic susceptibility of LCO was also assessed under field 5000 Oe from 6-300 K, as shown in Figure 4.2 (b). The magnetization response for all samples increases with lowering measurement temperature, and rise of magnetization occurs with

decreasing size, in agreement with *M-H* result. The temperature dependence of magnetic susceptibility follows the Curie-Weiss law and the estimated Weiss temperature (with fitting range temperature from 0 to 300 K) are about -1.96 K, -2.17 K, -3.7 K, -1.94 K for sample with 69 nm, 96 nm, 153 nm and 286 nm size, respectively. The effective magnetic moment (μ_{eff}) of the samples were calculated from $\mu_{eff} = 2.84\sqrt{\chi.(T-\theta)}$. The tendency of μ_{eff} increases with reducing size with the values 0.701 μB, 0.73 μB, 0.443 μB and 0.353 μB for sample with 69 nm, 96 nm, 153 nm and 286 nm size, respectively.

The magnetic moment of LCO was found increases with decreasing size. One possible reason is, from FESEM image observation, the aggregated particles shows variety of particle dispersion with different size and shape, thus for every particle, either aggregated or not, will also have different distribution of magnetic moment that oriented differently for each aggregated particle, and the magnetism will interact each other.[5)] Additionally, lattice parameters from XRD result shows deviation as a function of size, indicating the orthorhombicity of samples is also changed and the sample experiencing atomic distortion. The distortion induces the spins to align disorder, therefore the increase of magnetic moment is expected. Moreover, the volume of unit cell of samples also becomes bigger with reducing size, indicating there are incorporation of oxygen excess, particularly at surface. Oxygen is non-magnetic, but it is paramagnetic.[6)] because it has unpaired electron, therefore the paramagnetic behavior of oxygen will involve and contributing to the magnetic measurement. Moreover, since there is a lattice deviation was observed, therefore influencing the orthorhombicity in the sample and atomic distortion occurs, furthermore influencing the magnetic properties. Accordingly, the total magnetic moment in the LCO NPs now is expected coming from the contribution of two components: surface property and core property, which responsible for the enlargement of magnetic moment. However, in our work, no clear indication of magnetic transition signal T_N were observed in all samples, probably it concealed by surface property that dominating during magnetic susceptibility measurement and leads to slightly modifications in LCO

properties.[7] However, the sign of negative Weiss temperature here proving the intrinsic property is still AF.

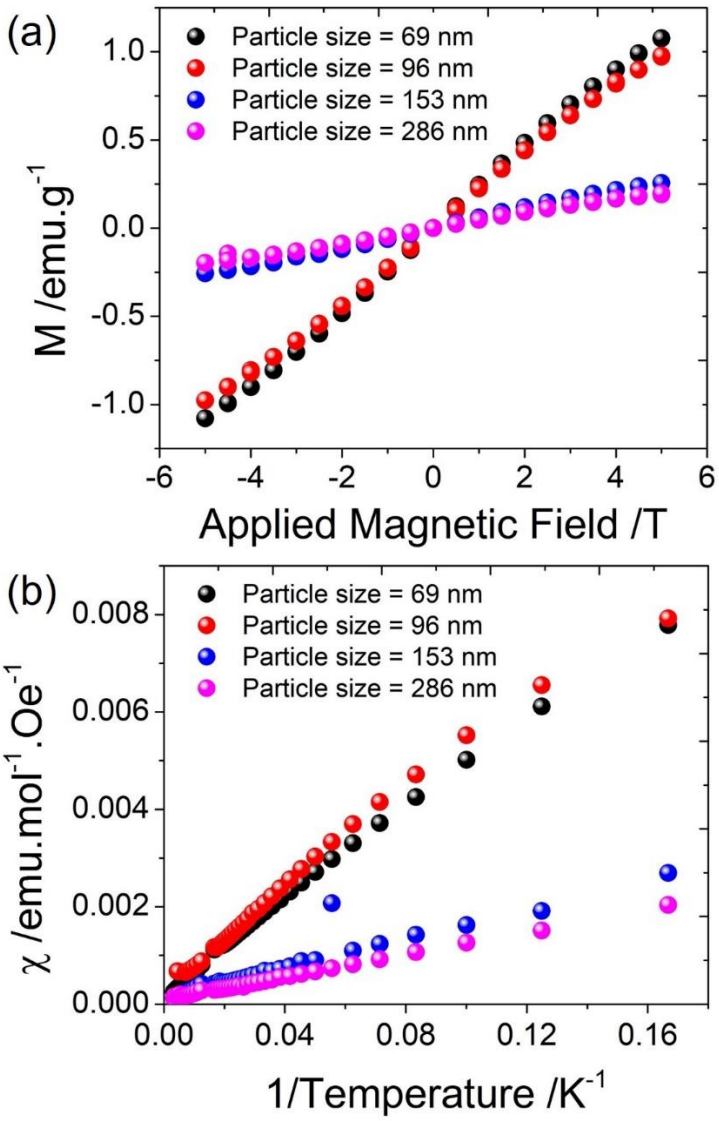

Figure 4. 2 *M-H* curve of the fabricated LCO with different. Inset is the temperature dependent magnetic susceptibility.

To overcome the sign of T_N, here the ordered magnetic property of the synthesized LCO was also evaluated by Zero Field (ZF)-μSR measurement, therefore the magnetism in microscopic view could be observed, and the μSR time spectra of LCO with various size are shown in Figure 4.3. The μSR time spectra is interpreted by asymmetry parameter A(t), calculated from the ratio of numbers of positron detected by the forward [F(t)] and backward [B(t)] counters

at t time: [A(t) = (F(t) – αB(t)]/[F(t) + αB(t)], and all time spectra are corrected by calibration factor α during analysis. The μSR time spectra was fitted to Equation 4.2:

$$A(t) = A_1 \cos\left(\gamma_\mu H_{int} t + \phi\right) e^{-\lambda_1 t} + A_2 e^{-\lambda_2 t} \quad \text{(4.2)}$$

First and second terms correspond the muon-spin precession component and fast depolarizing component, respectively, with A_1 and A_2 are the initial asymmetries of each component. The muon-spin precession reveals the AF order state, particularly the ordered state of Cu spins that aligned in the AF order state. For the 69 nm sample [Figure 4.3 (a)], clear muon spin precession spectra was observed at 10 K and 35 K and the amplitude gradually decreases with raising temperature. The precession disappeared at 60 K and 110 K, indicating the system has just changed to paramagnetic state, and, near this point we could identified the T_N. Similar spectrum was observed in the 96 nm sample, precession occurred at 10 K and 60 K [Figure 4.3 (b)] and vanish at 100 K. For the sample with 153 nm [Figure 4.3 (c)] and 286 nm [Figure 4.3 (d)] size, precession was observed at low temperature and there are no sign of the appearance of any magnetically ordered states at 150 K and 285 K, respectively.

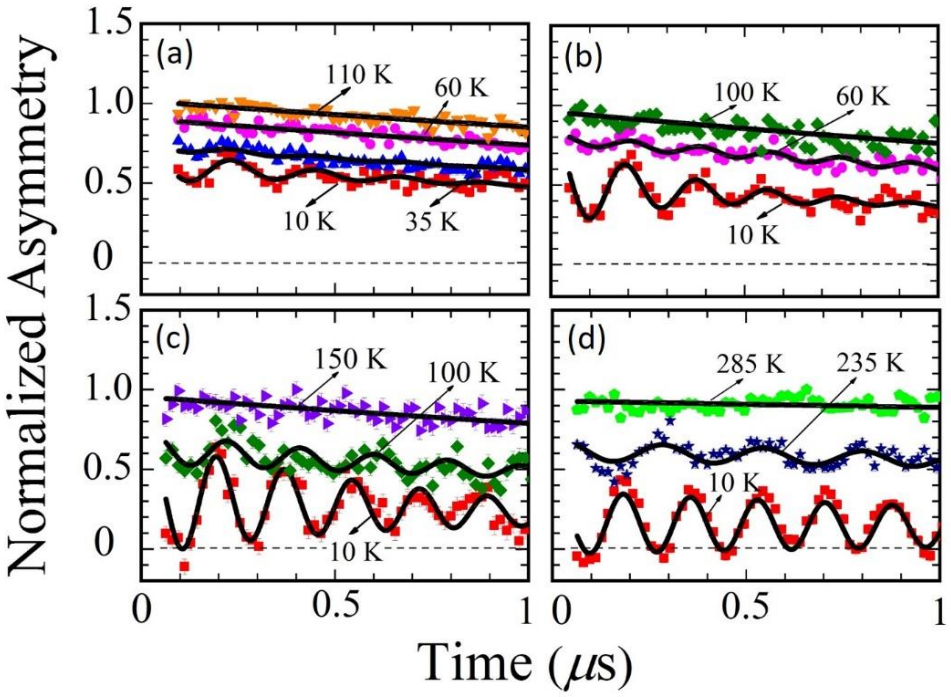

Figure 4. 3 ZF-μSR time spectra of the fabricated LCO with particle size: (a) 69 nm, (b) 96 nm, (c) 153 nm and (d) 286 nm at various temperature

The internal field (H_{int}) of LCO samples are shown in Figure 4.4 (a), and were calculated from $H_{int} = \omega/\gamma_{\mu}$, where γ_{μ} is the gyromagnetic ratio of the muon (13.55 MHz/kOe). The H_{int} of all samples at 10 K are about ~ 420 G, which closely equivalent with the sample value observed in the bulk LCO.[8)] The precession internal field undergoes abrupt change to zero at 60 K, 65 K, 150 K and 265 K for the sample with size 69 nm, 96 nm, 153 nm and 286 nm, respectively and this temperature denotes as the magnetic transition of LCO, as summarized in Figure 4.4 (a). The magnetic transition temperature of the Mott insulator of LCO was found to be dependent with the size, where the AF ordering state gradually decreases as decreasing size. Magnetic transition temperature of a material relates to the strength of exchange interaction and number of neighboring atoms.[9)] With smaller particle, the fraction of atom will be larger compared to their bulk and the atoms at surface will have less number of neighboring atom, therefore smaller particles tend to have lower coordination.

Thus, their exchange interaction will be weaker in a smaller particles because of lower coordination, and, in here, causing drastic reduction of magnetic transition temperature.

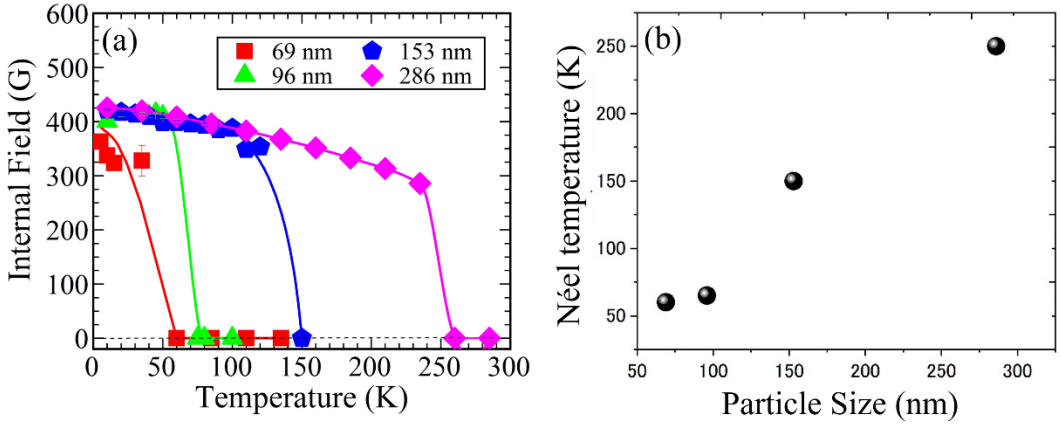

Figure 4. 4 (a) Temperature dependent internal field at muon site and (b) Néel temperature of LCO sample with various size

4.5. Conclusions

To conclude, here we have presented on how to fabricate the controlled size of nanometer-sized LCO by sol-gel technique and investigate its magnetic properties. The key to control the size of the product could be done by varying the annealing condition during synthesis. Reduction of size induces lattice deviation and expansion of unit cell volume, indicating the orthorhombicity of sample is changed. The magnetic properties of the nano-sized LCO were investigated and reduction of size causes magnetization enhancement and reduction of T_N. The enhanced magnetization is expected because the magnetic signal coming from distribution of magnetic moment because of random particles dispersion of aggregated particles, seen from SEM images, also lattice deviation from XRD results. Also, by having smaller particles, there will be less neighboring atom (reduced coordination number) therefore the interaction will be weaker and causes reduction of T_N.

4.6. References

1) A. Fernández-Pacheco, R. Streubel, O. Fruchart, R. Hertel, P. Fischer and R.P. Cowburn, Nat. Commun. 8, 15756 (2017).
2) E. Grabowska, Appl. Catal. B: Environ. 186, 97 (2016).
3) F. Zhou, Growth and Characterization of Bulk Superconductor Material (Springer, Switzerland, 2016)
4) V.G. Storchak, J.H. Brewer, D.G. Eshchenko, P.W. Mengyan, O.E. Parfenov, A.M. Tokmachev and P. Dosanjh, Phys. Rev. B 94, 134407 (2016).
5) S. D. Tiwari, K. P. Rajeev, Phys. Rev. B 72, 104433 (2005).
6) M. Ivanovskaya, E. Ovodok and V. Golovanov, Chem. Phys. 457, 98-105 (2015).
7) M. Molina-Ruiz, A. Lopeandía, F. Pi, D. Givord, O. Bourgeois and J. Rodríguez-Viejo, Phys. Rev. B. 83, 140407 (2011).
8) J.I. Budnick, A. Golnik, C. Niedermayer, E. Recknagel, M. Rossmanith, A. Weidinger, B. Chamberland, M. Filipkowski, and D.P. Yang, D.P., Phys. Lett. A, 124, pp.103-106 (1987).
9) X. Zheng, C. Xu, K. Nishikubo, K. Nishiyama, W. Higemoto, W. Moon, E. Tanaka and E.S. Otabe, Phys. Rev. B. 72, 014464 (2005).

CHAPTER 5

Assembly and Electrical Properties of La_2CuO_4 and $SrTiO_3$ Nanoparticles Based on Dielectrophoresis for Future Electronic Device Applications

5.1. Abstract

La_2CuO_4 (LCO) and $SrTiO_3$ nanoparticles (NPs) and were aligned at electrodes by dielectrophoresis (DEP) to measure the electric properties. Electrodes separated with nanoscale gap were firstly fabricated via electron beam lithography (EBL). After that, the NPs were trapped by applying gradient electric field. From electrical characteristics, the conductance increases as the temperature is raised. Arrhenius plot analysis indicating that two conductions mechanism occur (hopping and tunneling).

5.2. Introduction

Advancement of technologies driven the demand of electronic devices on a nanometer scale for high density electronic devices and effectively transporting the electric current. One interesting material to be investigated is a perovskite.[1)] Variation of electric properties from insulator, semiconductor and metallic insulator is feasible in a perovskite, relying on the charge carriers and materials itself.[2)] Among perovskite materials, here La_2CuO_4 (LCO) nanoparticles (NPs) and $SrTiO_3$ (NPs) are selected. Bulk LCO is an antiferromagnetic (AF) Mott insulator with Néel temperature (T_N) of about 300 K[3)]. Therefore, LCO is potentially utilized as a sensor,[4,5)] spin-valve[6)] or numerous prospect in electronic devices. Moreover, the wide band gap of STO 3.75 eV[7)] makes the material good to be used as capacitors[8)] Since STO is also an excellent substrate for the epitaxial growth of various oxides,[9-11)] physics of complex oxide heterostructures based on STO material is also of interest to be investigated[12-14)] Utilization of LCO and STO NPs become important since they hold important and great properties, and here its electrical investigation in its nanoscale order is investigated. To the best

of our knowledge, there was no detail information about the electric properties of free-standing STO and LCO NPs. Become fundamental and essential for further research in LCO and STO based compound.

In the present work, assembly and electrical properties investigation of LCO and STO NPs based on dielectrophoresis (DEP) technique were reported. DEP is a phenomenon where a dielectric matter move due to force created by non-uniform electric field.[15] It offers a low-cost method to assembly nanostructure in an electrode device.[16] Here, electrodes separated with nanoscale gap were firstly fabricated via electron beam lithography (EBL), and then the fabricated NPs were assembled at the electrodes by DEP technique. Furthermore, the set up was utilized prior to electrical properties measurement. From the results, the LCO NPs act as semiconducting material and the behavior was also confirmed by optical band gap energy measurement by UV-Visible spectrophotometry. Therefore, NPs assembly is potentially to be utilized for various purposes electronic device applications.

5.3. Experimental procedure

Electrodes separated with nanoscale gap were fabricated via electron beam (EB) lithography method, with SiO_2 as the substrate. Firstly, EB resist solution (gL 2000:anisole = 1:1) was spin coated to the substrate with speed 5000 rpm for 40 s and pre-baked at 180 °C for 3 min. The electrode patterning was performed by EB machine model Elionix ELS-7500. The as obtained patterns were developed by ZED-50 N solution for 5 min continued by isopropanol for 15 sec, then rinsed by DI water and dried. The electrodes Pt/Ti with thickness 24/6 nm (Ti next to the substrate) were deposited by sputtering machine model CFS-4EP for LCO NPs sample, whereas Al electrodes was deposited for the STO NPs sample. The residue of EB resist then was removed by dipping it in dimethyl sulfoxide solution at 80 °C for 40 min, followed by isopropanol cleaning under sonication process.

The LCO NPs were aligned at the edge of electrodes by DEP method. Firstly, small amount of LCO NPs was suspended into ethanol. Centrifugation was

performed to the suspension, prior to avoiding the agglomeration of particles. Secondly, the suspension then was casted to the electrode device and naturally dried. During casting, AC voltage was applied at both electrodes to induce the electric field, with phase difference 180°. The voltage and frequency used were V_{pp} = 5 V and f = 1 MHz respectively. After that, the device was heated at 450 ℃ for 30 min in Ar environment, to make a good electrical contact. For electric property measurement, a tailor-made cryogenic temperature probing system was used and the *I-V* responses were recorded as a function of temperature and voltage by semiconductor parameter analyzer model Keysight Agilent 4156A. All measurement were carried out in vacuum condition.

5.4. Results and discussion

4.4.1. Sample used

The morphology of the synthesized LCO and STO NPs are displayed in Figure 5.1 and the synthesis process was using sol-gel method and were explained in Chapter 3 in this thesis. The LCO and STO NPs used for electrical characteristic investigation has 69 nm and 21 nm size (based on FESEM images), with crystallite size 34.88 nm and 21.4 nm, respectively (based on XRD result).

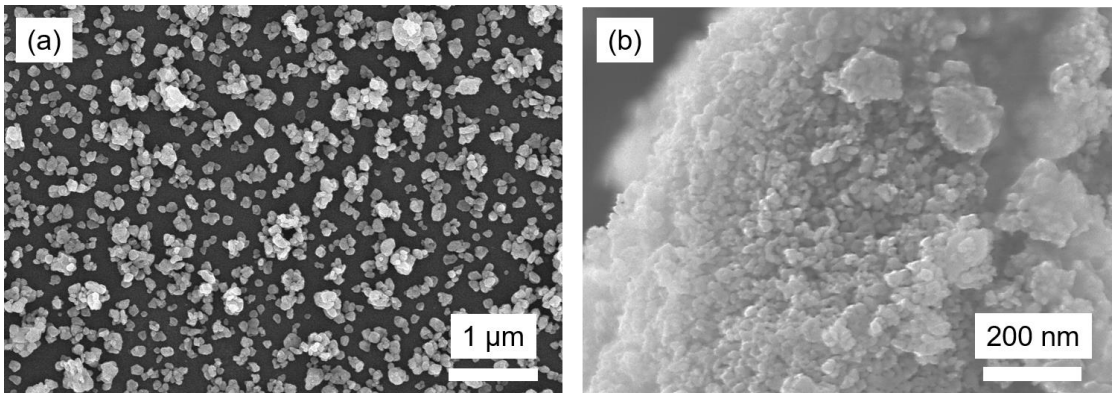

Figure 5. 1 (a) FESEM images of the synthesized (a) LCO and (b) STO NPs.

4.4.2. Electrical characteristics of LCO NPs

Figure 5.2 (a) displays the FESEM image of electrode device fabricated by EBL. As seen that the design of device consists of two electrodes and separated with nanometer size gap, and the gap size is about ~ 100 nm. The gap is expected place for LCO NPs to be located. Pt was used as the material electrode due to its high work function and to make good electric contact with p-type semiconductor (i.e. LCO). The fabricated electrode device then were casted by an ethanol suspension containing LCO particles, and, at the same time, AC voltage was applied between the electrodes prior to trapping process. The results of particles trapping were monitored by FESEM, as displayed in Figure 5.2 (b), inset is the FESEM images after tilted 80°. As seen the particles were well gathered and mounted, particularly at the gap of electrodes and bridging the electrodes. Figure 5.2 (c) shows the typical *I-V* of the device before and after subjected to annealing, purposing to obtain good electrical contact. As seen that if the device was un-annealed, the electrical contact is poor compared to the annealed one. As the heat treatment was done at lower temperature of the LCO synthesis temperature, therefore no significant change in the size of LCO.

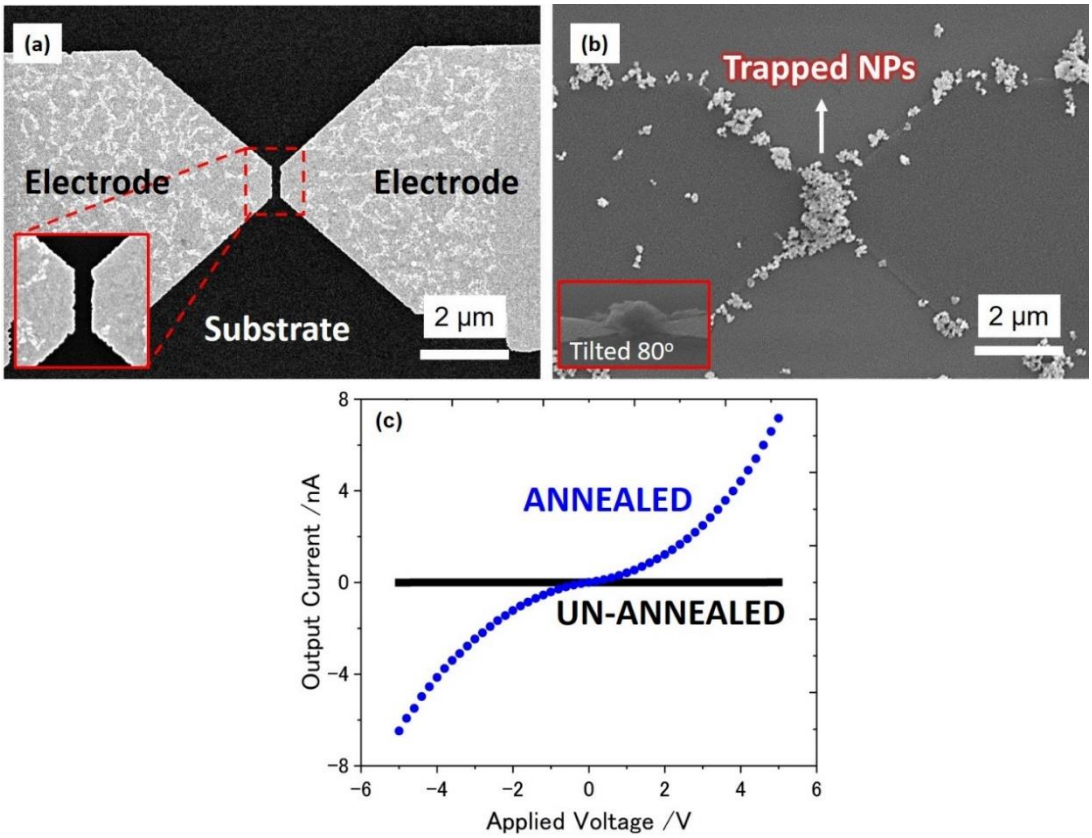

Figure 5. 2 FESEM image of the electrodes: (a) before and (b) after DEP and (c) connection of electrodes.

The electric properties of LCO NPs is displayed in Figure 5.3. The measured output current at variance of temperature in the inset of Figure 5.3 (a) and applied dc voltage. *I-V* curve of sample shows non-linear curve and the behavior of sample for all temperature are similar. The tendency of conductance of the sample gradually increases with raising temperature of measurement, indicating the sample are non-metallic. Moreover, Arrhenius plot analysis in the Figure 5.3 (b) shows the change in conductivity slope in two different temperature region and reveals two conduction mechanism: variable range hopping and tunneling, respectively with activation energy at 20.94 meV and 0.0071 meV at high and low temperature, respectively.

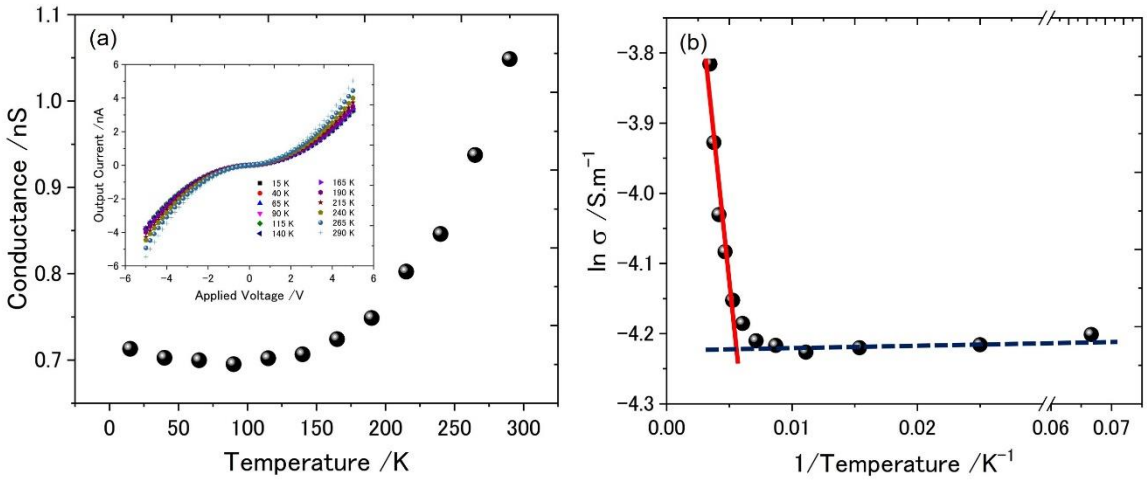

Figure 5. 3 (a) Temperature dependent conductance (inset is the *I-V* curve at various temperature) and (b) Arrhenius plot of LCO NPs

4.4.3. Electrical characteristics of STO NPs

FESEM images of the electrodes before and after STO NPs trapping are shown in Figures 5.4 (a) and 5.4 (b), respectively, and the obtained gap of the electrodes is about ~ 100 nm [Figure 5.4 (a)]. Al was used as the material electrode owing its low work function and preferable making good electrical contact with n-type semiconductor (i.e. STO). The trapping process and conditions were same like LCO case in previous section.

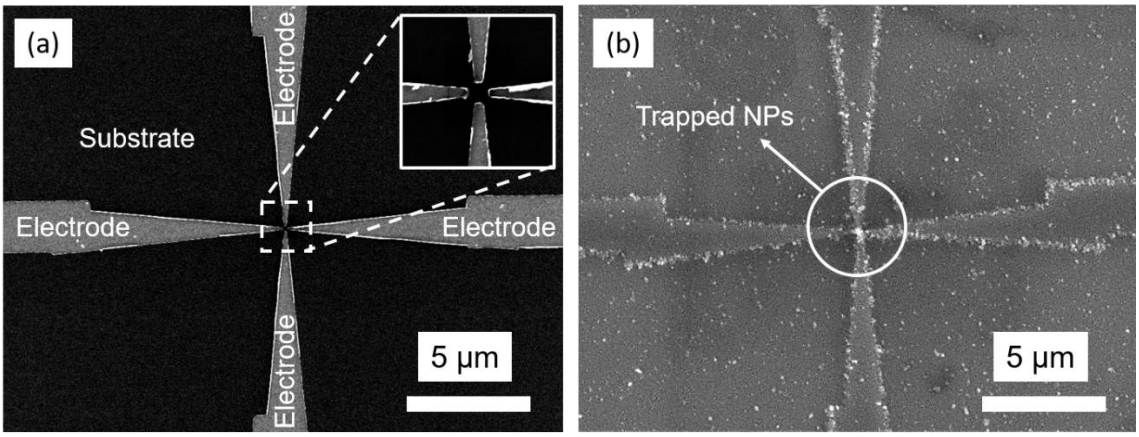

Figure 5. 4 FESEM images of electrodes: (a) before and (b) after DEP (Free permission to reuse as the authors. Copyright IOP Publishing)[17)]

The electric properties of the STO NPs at various temperature is displayed in Figure 5.4 (a). The conductance of sample raises with the increasing of

measurement temperature [inset in Figure 5.5 (a)], indicating the STO NPs are non-metallic. The conduction mechanism of STO NPs was also investigated by using Arrhenius plot, as displayed in Figure 5.5 (b). Arrhenius plot analysis shows two activation processes take place, marked by the change in conductivity slope in two temperature regions. The conduction mechanism occurs: hopping and dominant tunneling for high and low temperature region, with calculated activation energies at 0.0223 eV and 0.000537 eV, respectively.

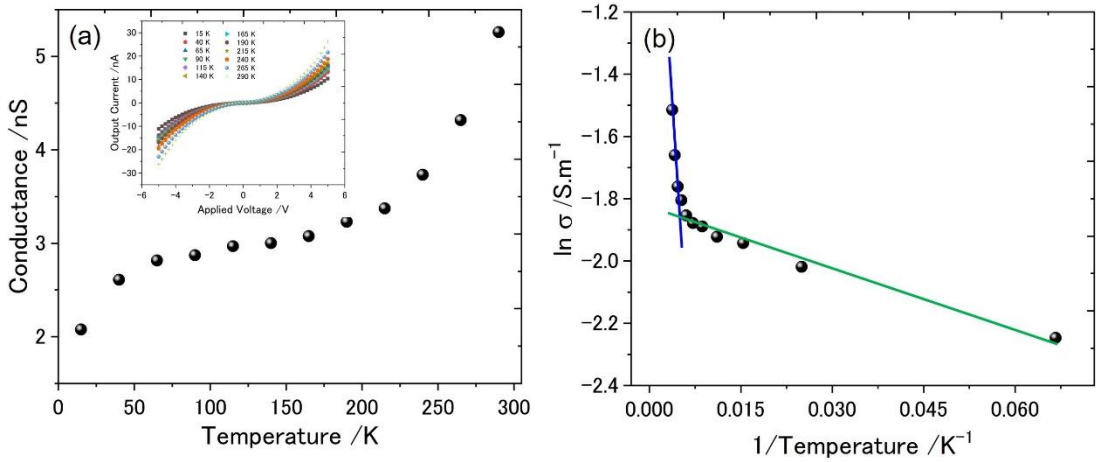

Figure 5. 5 Temperature dependent *I-V* characteristic of STO sample and (b) Arrhenius plot analysis

4.4.4. Discussions

The behind mechanism of trapping process started when a gradient electric field (AC field) is applied to the electrodes and induces dielectric force. At f = 1 MHz, the NPs were attracted to this field through the medium (i.e. ethanol) and gathered at the corner of electrodes. Upon ethanol is evaporating, the trapping were inactive. After trapping, the NPs well gathered at the edge of electrodes and some particles are trapped at the gap between electrodes, which bridging one electrode to another one and beneficiary for electric property measurement. Heat treatment was employed to the device to improve the electrical contact and reduce the interface trap density between metal electrode and the NPs sample.[18)] The heating process was done in Ar atmosphere to prevent any further oxidations.

As the heating temperature of the device was still below the NPs synthesis temperature, therefore there will be no change in the size of particles.

By observing the Arrhenius plot, there are two conduction mechanism occurs: hopping and tunneling at high and low temperature region, respectively for both LCO and STO NPs. Hopping conduction is recognized to be mechanism at high temperature, owing to thermal activation is involved, indicated by the temperature-dependence of *I-V* curve.[19] Here, hopping take places owing to the phonons are transferred to compensate the change energy of electron, and the electrons might be transported from one localized state to other state assisted by the energy transfer from the system. Moreover, tunneling behavior is also expected occur at low temperature (marked by the almost flat region in Arrhenius plot) owing to it does not show any temperature dependent *I-V* curve[19] and only shows field induced conduction. The current generated due to the electrons are penetrated to the sample (tunneling of electrons) from the barrier between low and high energy band, particularly by carriers of applied voltage field.

5.5. Conclusions

Electric properties of LCO and STO NPs were investigated based on NPs assembly using DEP technique. Electrodes separated with nanoscale gap were fabricated by EBL and the NPs were aligned to bridge the electrodes. Electrical investigation was done by low temperature probing system. The obtained current-voltage shows non-linear curve and temperature dependent electrical properties shows the conductance of STO and LCO NPs increases with raising temperature. Moreover, two conductions mechanism were observed in Arrhenius plot: hopping and tunneling. According to the results, the synthesized LCOand STO NPs is non-metallic.

5.6. References

1) J. Zhu, H. Li, L. Zhong, P. Xiao, X. Xu, X. Yang, Z. Zhao and J. Li, ACS Catal. 4, 2917 (2014).

2) K. Szot, W. Speier, G. Bihlmayer and R. Waser, Nat. Materi. 5, (2006).

3) V.G. Storchak, J.H. Brewer, D.G. Eshchenko, P.W. Mengyan, O.E. Parfenov, A.M. Tokmachev and P. Dosanjh, Phys. Rev. B. 94, 134407 (2016).
4) X. Zhou, Q. Cao, Y. Hu, J. Gao and Y. Xu, Sens. Actuators B: Chem. 77, 443 (2001).
5) H. Aono, M. Sakamoto and Y. Sadaoka: J Ceram. Soc. Jpn. 108, 1052 (2000).
6) B.G. Park, J. Wunderlich, X. Martí, V. Holý, Y. Kurosaki, M. Yamada, H. Yamamoto, A. Nishide, J. Hayakawa and H. Takahashi, Nat. Mater. 10, 347 (2011).
7) K. Van Benthem, C. Elsässer, and R. French, J. Appl. Phys. 90, 6156 (2001).
8) W. Gao, M. Yao, and X. Yao, Ceram. Int. 43, 13069 (2017).
9) S. Nakashima, S. Seto, Y. Kurokawa, H. Fujisawa, and M. Shimizu, Jpn. J. Appl. Phys. 56, 10PF17 (2017).
10) S. Okamoto, S. Okamoto, S. Yokoyama, K. Akiyama, and H. Funakubo, Jpn. J. Appl. Phys. 55, 10TA08 (2016).
11) C. Zhao, C. Zhou, and C. Chen, Physica B 521, 376 (2017).
12) A. Monteiro, D. Groenendijk, N. Manca, E. Mulazimoglu, S. Goswami, Y. Blanter, L. Vandersypen, and A. Caviglia, Nano Lett. 17, 715 (2017).
13) Z. Liu, L. Sun, Z. Huang, C. Li, S. Zeng, K. Han, W. Lü, T. Venkatesan, and Ariando, J. Appl. Phys. 115, 054303 (2014).
14) S. Gariglio, M. Gabay, and J. -M. Triscone, APL Mater. 4, 060701 (2016).
15) R. Pethig, A. Menachery, S. Pells and P. De Sousa, BioMed Res. Int. 2010, (2010).
16) B.C. Gierhart, D.G. Howitt, S.J. Chen, R.L. Smith and S.D. Collins, Langmuir. 23, 12450 (2007).
17) F. Budiman, T. Kotooka, Y. Horibe, M. Eguchi and H. Tanaka 57, 06HE07 (2018).

18) G. Greco, F. Iucolano and F. Roccaforte, Appl. Surf. Sci. 383, 324 (2016).
19) W. Wang, T. Lee and M. A. Reed, Phys. Rev. B. 68, 035416 (2003).

CHAPTER 6

The Effect of Particle Size on Magnetic Properties of $La_{1.80}Sr_{0.2}CuO_4$ Nanoparticles Fabricated by Sol-Gel Method

6.1. Abstract

$La_{1.80}Sr_{0.20}CuO_4$ (LSCO) nanoparticles (NPs) with different size were synthesized by sol-gel method. X-ray diffractometry and field emission scanning electron microscopy method showed the phase of all samples is LSCO with tetragonal structure and the morphology of samples are spherical. Size could be controlled by varying the annealing condition during synthesis. The magnetic properties of LSCO measured by SQUID magnetometer showed superconducting property with critical temperature at 24 K and cancellation of superconductivity is observed with LSCO sample near nano-sized region, owing to London penetration depth.

6.2. Introduction

Superconducting state is a phenomena where a superconductor material exhibit zero electrical resistance and expulsed magnetic field (typically occur at cryogenic temperature). To date, superconductivity in nanosystems are attracted the interest of researchers.[1)] Studies on superconductor $YBa_2Cu_3O_{7-x}$ (YBCO) showed that particle smaller than 110 nm did not possessed superconducting properties.[2)] Limitation of superconducting state owing to size was also observed in Al nanowires.[3)] Pinning of critical current density on YBCO superconductor was reported by doping with nano-sized Al_2O_3.[4)] That aside, the behavior of superconductor material in nanoscale systems could be dissimilar from its counter bulk.

Nano-sized $La_{2-x}M_xCuO_4$ (M = metal) is the superconducting system that investigated here. LMCO is well known the first high temperature cuprate superconductor (HTSC), as discovered by Bednorz and Muller in La-Ba-Cu-O

system.[5] The based compound itself, bulk La_2CuO_4 (LCO), is an antiferromagnetic (AF) Mott insulator with Néel temperature (T_N) of about 300 K.[6] LCO based compound is considered one of best studied on superconducting phenomena due to its simple structure.[7] The transition from AF to SC state could be derived upon introducing metal (M = Sr, Ba, Ca) to the system with doping level $0.05 < x < 0.3$.[8] At such doping level, the T_N decreases to zero and superconducting property appears with critical temperature (T_c) as high as 40 K.[7]

In the present work, the effect of particle size on the magnetic properties of LSCO (x = 0.2) samples synthesized through sol-gel technique is reported. Sol-gel was chosen considering the product yield by this method is high in purity and homogeneity, and size is controllable.[9] Then, the magnetic properties of sample were investigated by SQUID magnetometer. According to the results, superconducting state is cancelled in LSCO with size near ~ 100 nm.

6.3. Experimental procedure

LSCO (x = 0.2) were prepared from La_2O_3 (Sigma Aldrich, 99.9%), $SrCO_3$ (Sigma Aldrich, 99.9%) and CuO (Wako, 99.9%) powders as starting materials with appropriate stoichiometric amount. The La_2O_3 was first heated at 700 ℃ for 2 h, then the La_2O_3 and CuO powders were dissolved in HNO_3 to form its nitrate. The precursors were mixed under continuous magnetic stirring, before $SrCO_3$ was added. Citric acid and ethylene glycol were used as organic fuel to enhance the binding between cation. The precursors was heated at 150 ℃ to remove water and continued at 300 ℃ for decomposing the organic matters. Crystallization process was performed by annealing the samples at 600, 700 and 800 ℃ for 3 h with heating up rate 10 ℃/min in air atmosphere. The final product then was ground by agate mortar until fine powder was obtained.

The phase of samples were identified by x-ray diffractometry (XRD, Rigaku RINT-2100) with Cu Kα radiation 40 kV (λ = 0.154 nm) and scanning rate 0.02 ^{o}/s. Morphology of samples were observed by field emission scanning electron microscopy (FESEM, Hitachi S-5200) with voltage at 5 kV. The average particle

size were measured through the diameter particles from SEM image, from one edge to the other opposite edge of particle using Image J software.

The magnetic property of LCO was measured using Quantum Design MPMS SQUID magnetometer. The samples were placed to a capsule and inserted into the magnetometer. For M (T) measurement, the temperature was ranged from 5 to 300 K, with applied field 100 Oe. M (H) measurement also performed for several samples at 5 K.

6.4. Results and discussion

Our previous work in LCO synthesis showed that the minimum annealing temperature for LCO phase formation was at 600 ℃ (Plase refer to Chapter 3). Therefore, here the annealing temperature of synthesis was varied from 600 ℃ to 800 ℃ at fixed time 3 h, to obtain LSCO particles with different size. Figure 6.1 (a) shows the XRD profiles of the synthesized LSCO samples annealed at 600 ℃ to 800 ℃ for 3 h. The peaks in XRD profiles reveals that the LSCO phase present in all samples. The samples have tetragonal structure and sharp peaks indicate the samples are highly crystalline. FESEM images in Figure 6.1 (b), (c), (d) displays the morphology of LSCO samples in FESEM images is sphere-like structure and the size is annealing temperature dependence. The average particle size were measured based on FESEM images and noted to be 103 nm, 114 nm and 164 nm for samples annealed at 600 ℃ [Figure 6.1 (b)], 700 ℃ [Figure 6.1 (c)], and 800 ℃ [Figure 6.1 (d)], respectively. Evidently, size of samples could be controlled by synthesis annealing temperature. The particle growth is strongly influenced by thermal energy for diffusion to occur.[10)] As energy is related to the boundary motion, the diffusion of atom occurs between atoms and higher energy causes reduction of grain boundaries and big particle is formed.

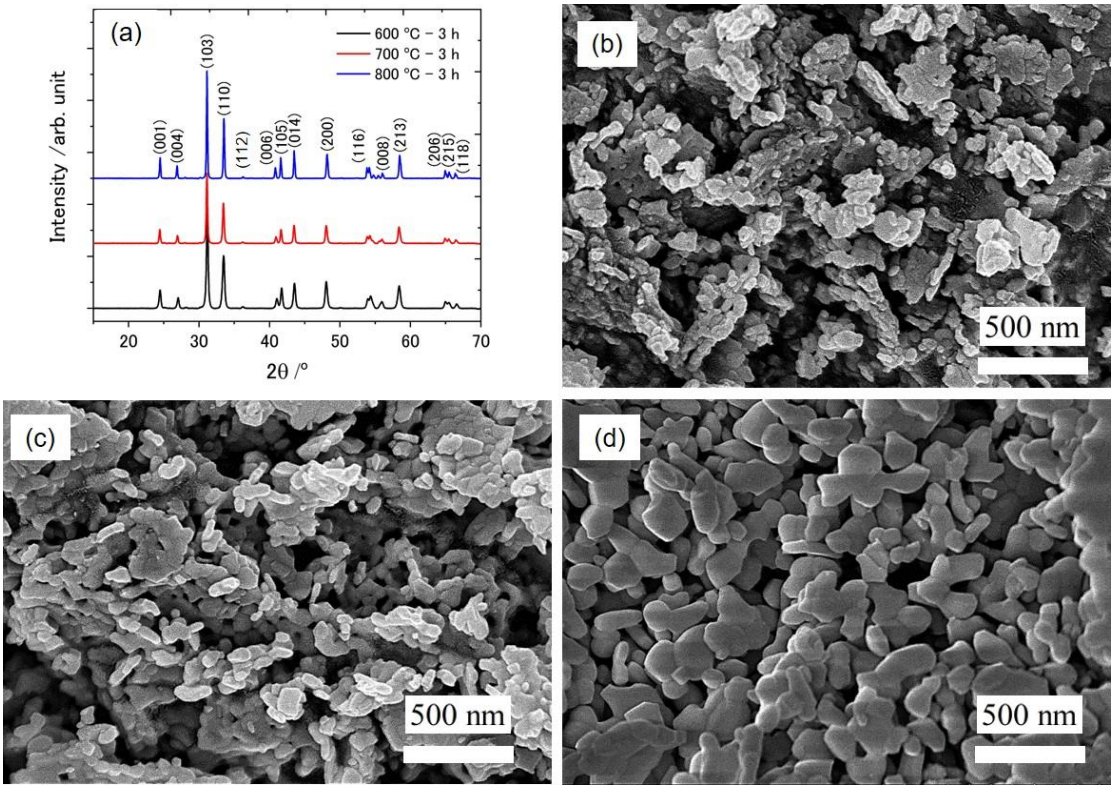

Figure 6. 1 (a) XRD and FESEM images of the synthesized LSCO samples annealed at: (b) 600 ℃, (c) 700 ℃ and (d) 800 ℃ for 3 h

The formation of LSCO in this work started by mixing the starting materials with nitric acid. As the metal oxide dissolved in the acid, metal nitrate is formed and hydrolysis start taking places. The binding between metals ion (La, Cu and Sr) is enhanced by the addition of organic fuel (ethylene glycol and citric acid), also to prevent precipitation of each oxide. The pH was controlled by NH_3 (aq), which also provides N and H to the system as the additional organic fuel during heating. Heating were performed at temperature 150 ℃, then 300 ℃ for 3 h to remove water and for decomposing all the organics matter, respectively. Final annealing at higher temperature 600-800 ℃ was performed for crystallization.

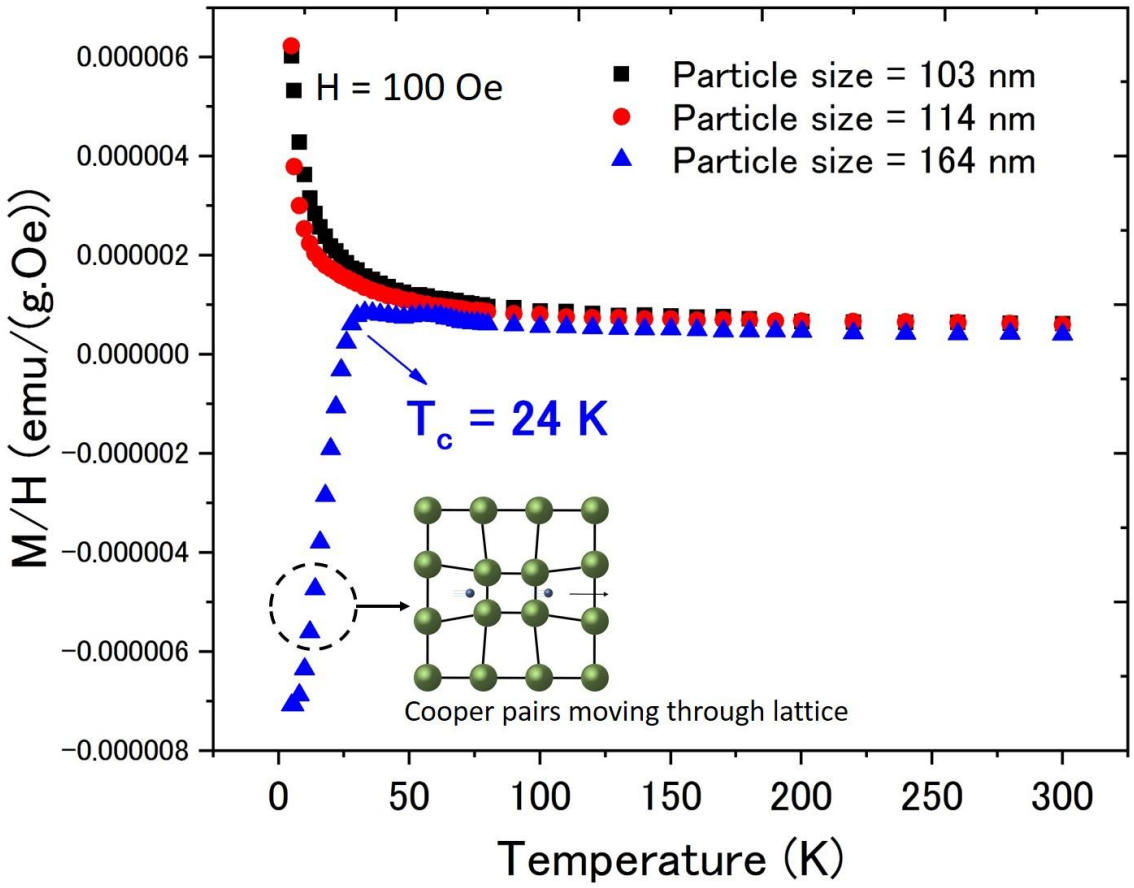

Figure 6. 2 Temperature dependent magnetic properties of LSCO with different particle size under magnetic field 100 Oe.

Figure 6.2 shows the magnetic properties of the synthesized LSCO with different particle size. According to phase diagram of $La_{2-x}Sr_xCuO_4$, sample with x = 0.2 should exhibit superconducting at low temperature.[11] By observing Figure 6.2, it can be seen LSCO sample with 164 nm size exhibit superconducting region with critical temperature (Tc) of about 24 K., good agreement with the phase diagram. Below the Tc, the magnetic flux is expulsed – called Meissner effect. At this condition, the resistance became zero because the scattering of electron are unable to the motion of current carriers due to the effect of Cooper pairs. Electrical resistance in metals arises because electrons propagating through solid are scattered in the metal. In superconductor material, the current is carried by pairs of electrons known as Cooper pairs.[12] Small attraction between electrons in a material causing two negatively charged

electrons are bound together (a paired state of electrons), as illustrated in the inset of Figure 6.2. The space occupied by one pair contains many other pairs, and there is thus a complex interdependence of the occupancy of the pair states. There is then insufficient thermal energy to scatter the pairs. The pairs thus carry current freely, then superconducting property occur. On the contrary, sample with 114 and 103 nm size exhibit paramagnetic instead superconducting. Upon metal doping to superconducting region, the T_N sharply decreases[13] to zero, therefore paramagnetic behavior appears. Another possible reason is, the reduced size making the material to become more defective at surface[14] and contributed in magnetic measurement. Additionally, it also can be observed that superconductivity is cancelled in 114 and 103 nm samples. If magnetic field enters a superconductive material, the magnetic field is not directly repelled by the sample, instead the intensity gradually decreases and become zero at certain point, due to effect of London penetration depth,[15] as illustrated in Figure 6.3. London penetration depth is defined as the allowed distance for magnetic field to penetrate to the surface of a superconductor material. As the particle size is small, thus the Meissner effect is cancelled because the London penetration depth is equal with the particle size. The London penetration depth of LCO based compound was reported ranging from ~ 1000 to 3000 Å,[16] which in here is almost equal to particle size. In the case of $YBa_2Cu_3O_{7-x}$ material, similar superconductivity cancellation also observed when the size of sample was made < 110 nm.[17]

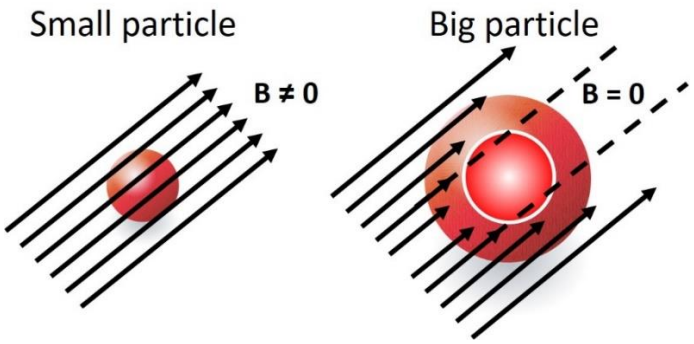

Figure 6. 3 Illustration of Meissner effect cancellation due to the effect of London penetration depth

6.5. Conclusions

The effect of particle size on the magnetic properties of $La_{1.80}Sr_{0.20}CuO_4$ (LSCO) nanoparticles (NPs) synthesized by sol-gel method are reported. The size could be controlled by annealing condition during synthesis. Bigger particle size could be yielded when the synthesis annealing temperature was high, owing to grain growth induced by thermal energy. The magnetic properties of sample were investigated by SQUID magnetometer. LSCO with big particle exhibit superconducting property with critical temperature 24 K. Additionally, superconductivity was cancelled if the sample is approximately in nano-sized region, one possible reason owing to London penetration depth that equal with the particle size.

6.6. References

1) S. Bose and P. Ayyub, Rep. Prog. Phys. **77**, 116503 (2014).
2) V. Blanco-Gutiérrez, M. Torralvo-Fernández and M. Alario-Franco, Dalton Trans. **46**, 11698 (2017).
3) M. Zgirski, K.-P. Riikonen, V. Touboltsev and K. Arutyunov, Nano Lett. **5**, 1029 (2005).
4) N. Moutalbi, J.G. Noudem and A. M'chirgui, Phys. C. **503**, 105 (2014).
5) K.A. Müller and J.G. Bednorz, Sci. **237**, 1133 (1987).
6) V.G. Storchak, J.H. Brewer, D.G. Eshchenko, P.W. Mengyan, O.E. Parfenov, A.M. Tokmachev and P. Dosanjh, Phys. Rev. B. **94**, 134407 (2016).
7) A. Mourachkine: Room-temperature superconductivity (Cambridge Int Science Publishing, U.K., 2004).
8) F. Zhou: Growth and Characterization of Bulk Superconductor Material (Springer, Switzerland, 2016)
9) A. Danks, S. Hall and Z. Schnepp, Mater. Horizons. **3**, 91 (2016).

10) F. Humphreys and M. Hatherly: Humphreys FJ, Hatherly M. Recrystallization and Related Annealing Phenomena. Oxford, Pergamon, 1995).

11) B.O. Wells, Y.S. Lee, M.A. Kastner, R.J. Christianson, R.J. Birgeneau, K. Yamada, Y. Endoh and G. Shirane, Sci. **277**, 1067 (1997).

12) L.N. Cooper, Phys. Rev. **104**, 1189 (1956).

13) J. Budnick, B. Chamberland, D. Yang, C. Niedermayer, A. Golnik, E. Recknagel, M. Rossmanith and A. Weidinger, Eur. Phys. Lett. **5**, 651 (1988).

14) S. Banerjee, A. Datta, A. Bhaumik and D. Chakravorty, J Appl. Phys. **110**, 064316 (2011).

15) R. Prozorov and R.W. Giannetta, Supercond. Sci. Technol. **19**, R41 (2006).

16) A. Savici, Y. Fudamoto, I. Gat, T. Ito, M. Larkin, Y. Uemura, G. Luke, K. Kojima, Y. Lee and M. Kastner, Phys. Rev. B. **66**, 014524 (2002).

17) V. Blanco-Gutiérres, M. J. Torralvo-Férnandez, and M. A. Alario-Franco, Dalton Trans., 11698-11703 (2017).

CHAPTER 7

Weak Ferromagnetism in La_2CuO_{4-y} Nanoparticles

7.1. Abstract

La_2CuO_{4-y} (LCO_{4-y}) were prepared by annealing the original LCO NPs under Ar atmosphere at 450 ℃ for 24 h. Morphology observation utilizing scanning electron microscopy showed there are no significant change in term of particle size, since the heating condition is lowered than the synthesis temperature. Diffraction studies shows some of the sample exhibit structural changed after heat treatment. Temperature dependent magnetic properties measurement indicated weak ferromagnetism appeared in the sample and varied with size. It is expected that heating introduced defect and give rise to weak ferromagnetism and size affecting its magnitude, owing to surface effect.

7.2. Introduction

Magnetism in nanoscale materials has attracted attention of researchers in past years since the properties may diverged from their bulk.[1)] Magnetization enhancement[2,3)] and reduction of magnetic transitions[4,5)] were observed as the material is made in nanoscale. Here, magnetism in a nanoscale perovskite oxide is investigated considering the properties of a perovskite can be tuned. Non-stoichiometry is also allowed in a perovskite,[6)] therefore the oxygen concentration in the sample could be varied and may shifting the properties.

La_2CuO_4 (LCO) is a perovskite oxide, and, in its stoichiometric form, it is an antiferromagnetic (AF) insulator.[7)] Upon doping, the properties of LCO gradually changed, and, at certain level will exhibit superconductivity (SC) .[8)] In the case of metal doping ($La_{2-x}M_xCuO_4$, M = metal), SC could be attained at doping level $0.05 < x < 0.3$.[9)] By introducing oxygen, there are two possible regions: oxygen rich and oxygen poor, with oxygen rich region will give rise to SC.[9)] However, there are still a lot miscibility gaps in term LCO as a function of oxygen content. That aside, the magnetic properties in nanoscale LCO may also differs from its counter bulk.

Here, oxygen deficient (La_2CuO_{4-y}/LCO_{4-y}) of LCO nanoparticles (NPs) were prepared and its magnetic properties is investigated. The fabrication process of LCO was done by sol-gel technique and has discussed in Chapter 3. The LCO NPs were subjected for heating under Ar, in order to modify the oxygen content in the sample. According to the results, SC was not observed, indicating the oxygen content is insufficient to attain SC property, instead both paramagnetic and weak ferromagnetism were observed in the sample for both condition. Additionally, surface effect also plays role in the magnetic properties.

7.3. Experimental procedure

The samples used in this work was LCO NPs that synthesized by sol-gel method, and the fabrication process was explained in Chapter 3. There are four main samples used: synthesized at 600 ℃ - 45 min, 600 ℃ - 180 min, 700 ℃ - 180 min and 800 ℃ - 180 min, with average particle size of about 69 nm, 96 nm, 153 nm and 286 nm, respectively. The four samples were subjected to post-annealing at 450 ℃ for 24 h under two conditions: Ar and oxygen atmosphere. Morphology of samples were observed by field emission scanning electron microscopy (FESEM, Hitachi S-5200) with voltage at 5 kV and the diffraction data were collected using XRD, Rigaku RINT-2100 with Cu Kα radiation 40 kV (λ = 0.154 nm) and scanning rate 0.02 °/s was also used. Additionally, TG-DTA Rigaku Model TG8120 (see Figure 2.12) was used to estimate the oxygen content based on the change of weight of the sample during the heat treatment. The oxygen content was estimated by measuring the change of oxygen content according to equation 7.1.[4)]

$$\Delta\delta = \frac{M_s}{M_o}\frac{\Delta w_s}{ws} \quad \text{..... (7.1)}$$

where Δδ, Ms, Mo, ws are the change of oxygen content, molecular weight of the sample and oxygen and the weight of sample, respectively. After that, the magnetic properties of the annealed LCO were measured by Quantum Design MPMS SQUID magnetometer. The samples were placed to a capsule and

inserted into the magnetometer. *M-T* measurement were performed from 5 to 300 K, with applied field 100 Oe. Several *M-H* necessary measurement were also conducted at 100 K, to support the *M-T* data.

7.4. Results and discussion

Figure 7.1 displays the XRD profiles of the LCO_{4-y}, supported by FESEM image at the right side. Compared to the original LCO starting material, the LCO_{4-y} samples experienced structural changed to tetragonal structure, and the XRD profiles for all samples are same, as seen in the Figure 7.1 (a), (b), (c) and (d). By observing the FESEM images in Figure 7. 1 (right side), we expect there are no significant change in term of particle size after the heat treatment, due to the annealing temperature used was still lower compared to the synthesis temperature. Therefore, the average particle size are still assumed to be approximately 69 [Figure 7.1 (d')], 96 [Figure 7.1 (c')], 153 [Figure7.1 (b')] and 286 nm [Figure 7.1 (a')]. The change of orthorhombicity is expected because annealing under Ar also introduce defects -oxygen vacancy to the system.

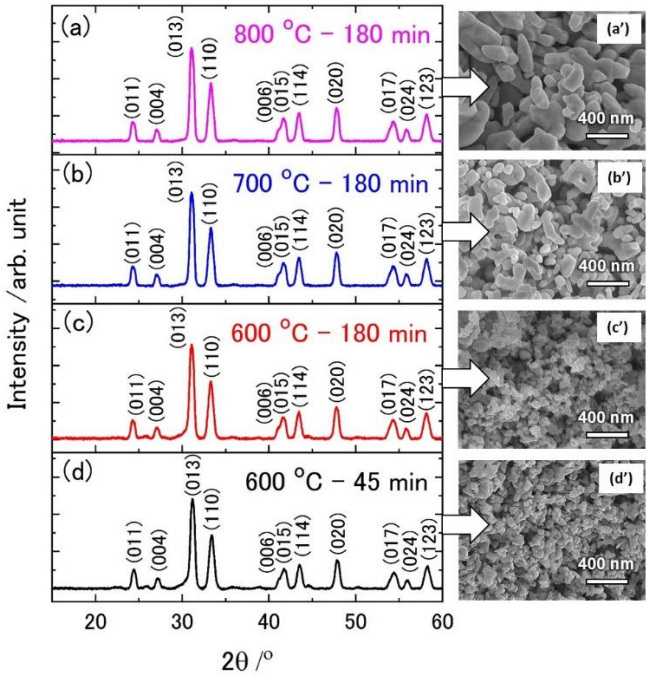

Figure 7. 1 XRD profiles of LCO after annealed under Ar at 450 °C for 24 h

The TG result of the sample is shown in Figure 7.2. The weight of sample decreases with raising time, indicating there are formation of defect-oxygen vacancy in the sample. The weight of sample after the heat treatment at 450 ℃ were measured decreasing about 3.27 %, after deducted with the influence of sample holder. Therefore, the estimated change of oxygen content in the sample was decreased about 0.1817.

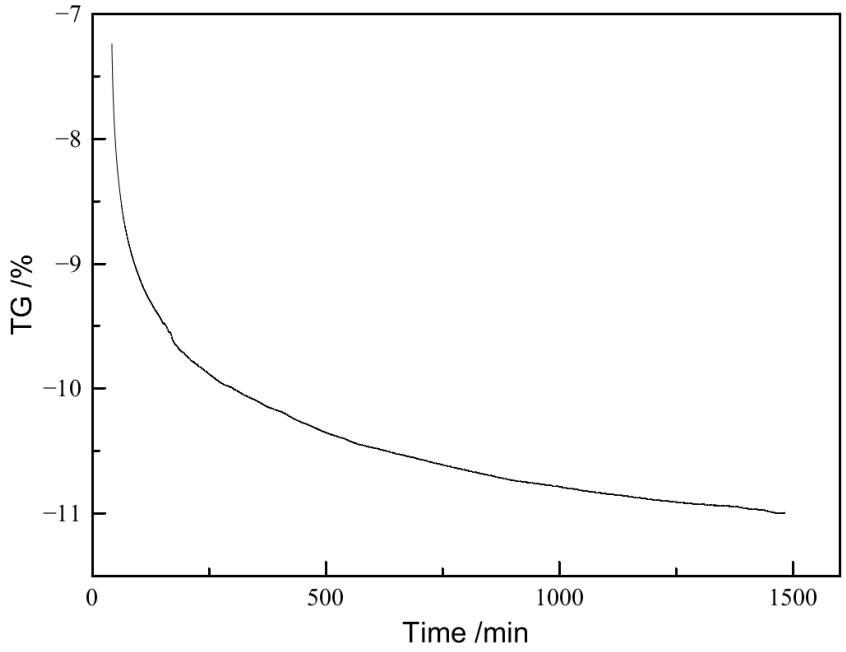

Figure 7. 2 TG result of sample

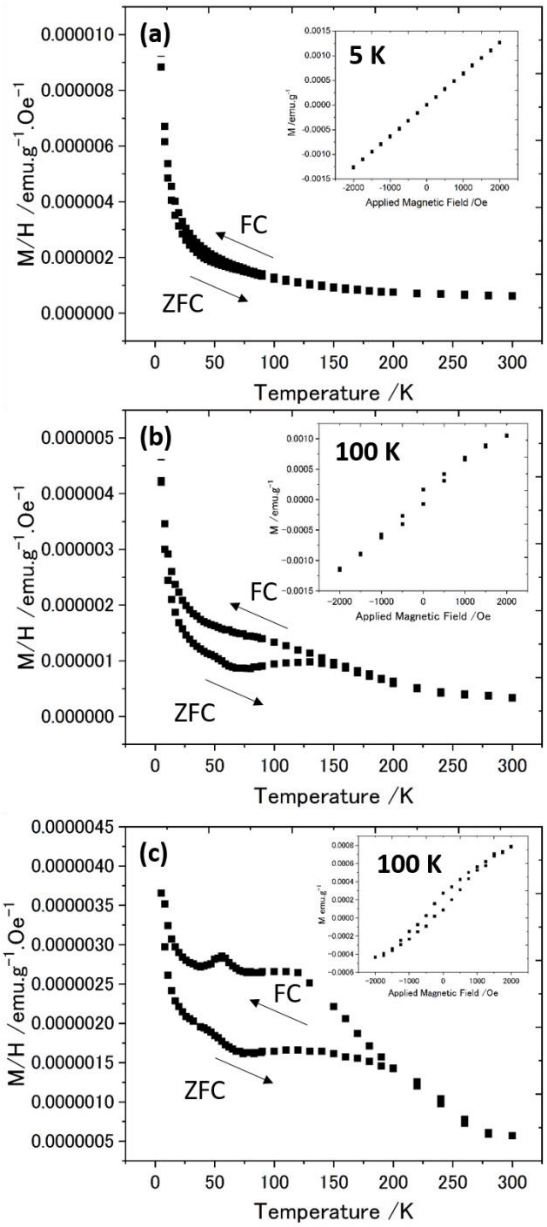

Figure 7. 3 *M-T* curve of the LCO_{4-y} with size: (a) 69 nm, (b) 153 nm and (c) 286 nm

Figure 7.3 shows the temperature dependent magnetic properties of samples with various size under low applied field 100 Oe. As shown, the magnetic properties of LCO_{4-y} shows the magnetization tends to stronger with reducing size. There are no superconducting property is observed, indicating the amount of oxygen vacancy is not sufficient to exhibit superconductivity. For the 69 nm sample [Figure 7.3 (a) and (d)], the sample exhibit paramagnetic behavior without any transition temperature is observed. In the 153 nm sample, similar

paramagnetic behavior also monitored [Figure 7.3 (e)], but, ferromagnetism also gradually appear in the sample anneal in Ar [Figure 7.3 (b)]. The ferromagnetism were proved by *M-H* measurement at 100 K, as seen there is a hysteresis magnetization in the inset of Figure 7.3 (b), but the intensity is very weak, up to 1000 Oe. The appearance of weak ferromagnetism more clearly observed in the 286 nm sample for both condition [Figure 7.3 (c) and (f)]. In this sample, both paramagnetic and weak ferromagnetic appear with transition occur at 56 K. *M-H* curve in the inset of Figure 7.3 (c) clearly indicates that weak ferromagnetism arises. By annealing, there are defects introduced to the structure, either by oxygen or oxygen vacancy, therefore it can give rise to paramagnetism.[11] Another possibility is, size reduction also induced surface effect, therefore there are uncompensated spins generated at the surface and contributing in magnetic measurement.[12] Additionally, the possible reason on the weak ferromagnetism aroused owing to point defects generated during the heating,[13] or there are spin canted induced by Dyzaloshinkii-Moriya interaction, related to the tilt of Cu-O octahedra.[14,15] Zakharov et al. also reported the hidden ferromagnetism in LCO_{4+y} due to canting moment.[16] Nikonov et al. also found similar LCO_{4+y} and occurred due to defect introduced causing the lattice distortion.[17] Spin canting is illustrated in Figure 7.4. As shown, the incorporation of oxygen defect, even small can cause lattice distortion. Here, since there are changed in the structure from the diffraction data, thus the orthorhombicity of sample is also changed. Additionally, the defectiveness of each sample is also different depending on the size, therefore the weak ferromagnetism appear in the sample also depending on the size.

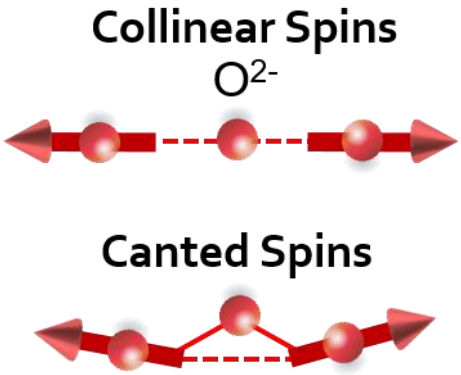

Figure 7. 4 Illustration of collinear spins and canted spins.

7.5. Conclusions

La_2CuO_{4-y} nanoparticles (NPs) were synthesized by annealing the original LCO under argon. There are no notable changes in size after annealing and diffraction data showed that the sample exhibit structural changed from orthorhombic to tetragonal. The magnetic properties of the samples were investigated by SQUID magnetometer and showing paramagnetic accompanied by weak ferromagnetism, and the similar behavior were observed for LCO_{4-y} samples. By reducing size, surface effect also give more defective surface to the sample. Also by heating, defects are introduced to the system and induce the spins to be canted and give rise to weak ferromagnetism.

7.6. References

1) A. Fernández-Pacheco, R. Streubel, O. Fruchart, R. Hertel, P. Fischer and R.P. Cowburn, Nat. Commun. 8, 15756 (2017).

2) R. Bhowmik, R. Nagarajan and R. Ranganathan, Phys. Rev. B. 69, 054430 (2004).

3) T.-J. Park, G.C. Papaefthymiou, A.J. Viescas, A.R. Moodenbaugh and S.S. Wong, Nano Lett. 7, 766 (2007).

4) N. Rinaldi-Montes, P. Gorria, D. Martínez-Blanco, A.B. Fuertes, I. Puente-Orench, L. Olivi and J.A. Blanco, AIP Adv. 6, 056104 (2016).

5) X. Zheng, C. Xu, K. Nishikubo, K. Nishiyama, W. Higemoto, W. Moon, E. Tanaka and E.S. Otabe, Phys. Rev. B. 72, 014464 (2005).
6) H. Kamimura, H. Ushio, S. Matsuno and T. Hamada, Theory of copper oxide superconductors (Springer Science & Business Media, Oxford, 2005).
7) A. Mourachkine, Room-temperature superconductivity (Cambridge Int Science Publishing, U.K., 2004).
8) F. Zhou, Growth and Characterization of Bulk Superconductor Material (Springer, Switzerland, 2016)
9) B.O. Wells, Y.S. Lee, M.A. Kastner, R.J. Christianson, R.J. Birgeneau, K. Yamada, Y. Endoh and G. Shirane, Sci. 277, 1067 (1997).
10) F. Chou, J. Cho, L. Miller and D. Johnston, Phys. Rev. B. 42, 6172 (1990).
11) M. Ivanovskaya, E. Ovodok and V. Golovanov, Chem. Phys. 457, 98 (2015).
12) Y. Tang, D.J. Smith, B. Zink, F. Hellman and A. Berkowitz, Phys. Rev. B. 67, 054408 (2003).
13) J. Wu, S. Mao, Z.-G. Ye, Z. Xie and L. Zheng, ACS Appl. Mater. Interfaces 2, 1561 (2010).
14) V. Mazurenko and V. Anisimov, Phys. Rev. B. 71, 184434 (2005).
15) D. Coffey, T. Rice and F. Zhang, Phys. Rev. B. 44, 10112 (1991).
16) A. Zakharov, A. Nikonov and O. Parfionov, Phys. Rev. B 57, R3233 (1998).
17) A. Nikonov, O. Parfenov and A. Zakharov, J Exp. Theoretical Phys. Lett. 66, 165 (1997).

CHAPTER 8
Conclusions and Suggestions

La_2CuO_4 and $SrTiO_3$ nanoparticles were successfully synthesized via sol-gel method. The roles to control the size was found to be dependent on annealing condition: temperature is in proportion with the size. The optimum parameter to synthesize LCO and STO NPs based on this research work is summarized in Table 8.1.

Table 8. 1 The optimum parameter to synthesize LCO and STO NPs

Parameter	LCO	STO
Starting material	Nitrate based compound	Citrate based compound
Annealing condition	600 ℃ for 45 min with pre-annealing at 300 ℃ for 3 h	500 ℃ for 5 h
pH	7	2
Organic material	Citric acid, ethylene glycol and ammonia	Citric acid and ethylene glycol

Electrical properties of the fabricated LCO and STO NPs were investigated based on aligning the NPs via dielectrophoresis technique at electrodes. The results showed that LCO and STO NPs acted as semiconductor material. Additionally, magnetic properties of LCO based compound were also investigated. Enhancement of magnetization were observed with reducing size, and, in the case of Sr doped to LCO, superconductivity is cancelled in NPs.

Based on present study, there are indeed much more can be done and the following ideas were suggested for future study.

1. To apply the synthesis parameter to synthesize other perovskite oxide nanoparticles.

Nanoparticles formation was successfully synthesized in this research work. Therefore, it is strongly suggested to apply the parameter to fabricate other nanomaterials with different properties (such as ferromagnetic, paramagnetic, antiferromagnetic, etc.). Thus, there are more prospect to use the material in wide applications.

2. To apply the material as gas sensor/electric nose.

Since this research work has introduced how to do nanoparticles alignment on an electrodes and conduct the electric property measurement based. Thus, it is suggested to apply the material as an electric nose (e-nose), to recognize some gases from air. Most metal oxide has semiconducting properties and tends to absorb moisture (surface functional group is –OH), therefore it can be utilized to sense the presence gas through the change of oxygen.

3. To study the dielectric property of sample.

In this research work, only dc electric properties is investigated. Since nanoparticles is expected to have large dielectric constant compared to their bulk, thus investigating the dielectric properties is worthy and may advantageous to be used as capacitor.

LIST OF PUBLICATIONS

1. **Faisal Budiman**, Kotooka Takumi, Yoichi Horibe, Masanori Eguchi and Hirofumi Tanaka (2018). Electric property measurement of free-standing $SrTiO_3$ nanoparticles assembled by dielectrophoresis. *Japanese Journal of Applied Physics*, *57*(6S1), 06HE07.
2. Hadiyawarman, **Faisal Budiman**, Detiza Goldianto Octensi Hernowo, Reetu Raj Pandey and Hirofumi Tanaka (2018). Recent progress on fabrication of memristor and transistor-based neuromorphic devices for high signal processing speed with low power consumption. *Japanese Journal of Applied Physics*, *57*(3S2), 03EA06.
3. **Faisal Budiman**, Suci Winarsih, Kotooka Takumi, Kouichi Takase, Yoichi Horibe, Isao Watanabe and Hirofumi Tanaka (2018). Origin of low Néel temperature in nanoscale of strong correlated La_2CuO_4. In preparation for publication.

LIST OF CONFERENCES

ORAL PRESENTATION

1. Suci Winarsih, **Faisal Budiman**, Hirofumi Tanaka, Takayuki Goto, Tadashi Adachi, Budhy Kurniawan, Isao Watanabe, *Finite Size Effects in La_2CuO_4 Nanoparticles Probed by μSR and NMR*, The 4th Emallia Conference, Hokkaido, Japan.
2. **Faisal Budiman**, Kotooka Takumi, Masanori Eguchi, Yoichi Horibe, Koichi Takase and Hirofumi Tanaka, *Size Dependent Magnetic and Electric Properties of Free-Standing La_2CuO_4 and $SrTiO_3$ Nanoparticles Synthesized by Sol-Gel Method*, International Conference on Nanoscience and Technology (ICN+T) 2018, Czech Republic.
3. **Faisal Budiman**, Kotooka Takumi, Yoichi Horibe and Hirofumi Tanaka, (2017), *Size Dependent Paramagnetic-Weak Ferromagnetic Transition in La_2CuO_{4-y}*, The 65th Spring Meeting of Japan Society Applied Physics, Fukuoka, Japan.
4. Takumi Kotooka, **Faisal Budiman**, Kouichi Takase, Yoichi Horibe and Hirofumi Tanaka, Electric and Magnetic Properties of $SrTiO_3$ Nanoparticles Synthesized by Sol-Gel Method, The 65th Spring Meeting of Japan Society Applied Physics, Fukuoka, Japan.
5. **Faisal Budiman**, Kotooka Takumi, Masanori Eguchi, Yoichi Horibe and Hirofumi Tanaka, (2017), The Effect of Particle Size on The Magnetic and Electric Properties of La_2CuO_4 and $La_{2-x}SrCuO_4$ Nanoparticles, The 30th International Microprocesses and Nanotechnology, Jeju, Korea.
6. **Faisal Budiman**, Yoichi Horibe and Hirofumi Tanaka, (2017), *Size Dependent Electric and Magnetic Properties of Oxygenated La_2CuO_4 Nanoparticles*, The 65th Autumn Meeting of Japan Society Applied Physics, Fukuoka, Japan.
7. **Faisal Budiman**, Yoichi Horibe and Hirofumi Tanaka, (2017), *Size Dependent Electric and Magnetic Properties of La_2CuO_4 and $La_{2-x}Sr_xCuO_4$*

Nanoparticles Fabricated by Sol-Gel Method, The 9th International Conference on Molecular Electronics and Bioelectronics, Kanazawa, Japan.

8. **Faisal Budiman**, Yoichi Horibe and Hirofumi Tanaka, (2017), *Cryogenic Temperature Magnetic and Electric Properties of La_2CuO_4 and $La_{2-x}Sr_xCuO_4$ Nanoparticles Synthesized by Sol-Gel Method*, The 64th Spring Meeting of Japan Society Applied Physics, Yokohama, Japan.
9. **Faisal Budiman**, Yoichi Horibe and Hirofumi Tanaka, (2016), *Low Temperature Synthesis and Magnetic Property of La_2CuO_4 Nanoparticles Synthesized by Sol-Gel Method*, The 4th Universiti Putra Malaysia-Kyushu Institute of Technology International Symposium on Applied Engineering and Sciences, Kitakyushu, Japan.
10. **Faisal Budiman**, Yoichi Horibe and Hirofumi Tanaka, (2016), *Superlattice Study of Lanthanum Cuprate Nanoparticles Synthesized via Sol-Gel Method under Air Pressure*, The 29th International Microprocesses and Nanotechnology Conference, Kyoto, Japan.
11. **Faisal Budiman**, Yoichi Horibe and Hirofumi Tanaka, (2016), *Crystal Structure Analysis of High Pressure Phase of La_2CuO_4 Nanoparticles under Air Pressure*, The 2nd Materials Research Society of Indonesia, Bandung, Indonesia.
12. **Faisal Budiman**, Yoichi Horibe and Hirofumi Tanaka, (2016), *Analysis Structural and Magnetic Properties of La_2CuO_4 Nanoparticles Synthesized by Sol-Gel Method*, The 77th Autumn Meeting of Japan Society Applied Physics, Niigata, Japan.

POSTER PRESENTATION

1. Suci Winarsih, **Faisal Budiman**, Hirofumi Tanaka, Takayuki Goto, Tadashi Adachi and Isao Watanabe, *Investigation of Nano-Sized Effects on the Magnetic Properties of La_2CuO_4 by using μSR and NMR*, The Physical Society of Japan Autumn Meeting 2018, Kyoto, Japan.
2. Suci Winarsih, **Faisal** Budiman, Hirofumi Tanaka, Takayuki Goto, Tadashi Adachi, Budhy Kurniawan, Isao Watanabe, *Reduction in Néel Temperature*

of Nanocrystalline La_2CuO_4 Probed by μSR and NMR, The 12th International Conference on Materials and Mechanism of Superconductivity, Beijing, China.

3. Takumi Kotooka, **Faisal Budiman**, Yoichi Horibe and Hirofumi Tanaka, (2017), Electrical and Optical Properties of $SrTiO_3$ Nanoparticles Synthesized by Sol-Gel Method, The 5th Universiti Putra Malaysia-Kyushu Institute of Technology International Symposium on Applied Engineering and Sciences, Selangor, Malaysia.
4. **Faisal Budiman**, Yoichi Horibe and Hirofumi Tanaka (2017), Size Dependent Electric and Magnetic Properties of La_2CuO_4 and $La_{2-x}Sr_xCuO_4$ Nanoparticles Synthesized by Sol-Gel Method, The 9th International Conference on Molecular Electronics and Bioelectronics, Kanazawa, Japan.
5. **Faisal Budiman**, Yoshinobu Fusao, Yoichi Horibe, Hirofumi Tanaka, (2016), *Fabrication of Dielectric Nanoparticles Toward Electric Devices Showing* Brain-*Like Signal Behaviour*, The 14th Annual Meeting of Nanoscience and Technology, Kitakyushu, Japan.